

Transmission electron microscopy on live catalysts

Bremmer, G.M.

Citation

Bremmer, G. M. (2017, December 21). *Transmission electron microscopy on live catalysts*. Retrieved from https://hdl.handle.net/1887/59505

Version: Not Applicable (or Unknown)

License: License agreement concerning inclusion of doctoral thesis in the

Institutional Repository of the University of Leiden

Downloaded from: https://hdl.handle.net/1887/59505

Note: To cite this publication please use the final published version (if applicable).

Cover Page



Universiteit Leiden



The following handle holds various files of this Leiden University dissertation: http://hdl.handle.net/1887/59505

Author: Bremmer, G.M.

Title: Transmission electron microscopy on live catalysts

Issue Date: 2017-12-21

Transmission Electron Microscopy on live catalysts

Transmission Electron Microscopy on live catalysts

Proefschrift

ter verkrijging van de graad van Doctor aan de Universiteit Leiden op gezag van Rector Magnificus prof. mr. C.J.J.M. Stolker volgens besluit van het College voor Promoties te verdedigen op donderdag 21 december 2017 klokke 10:00 uur

door

Gerrit Marinus Bremmer geboren te Katwijk aan Zee in 1990

Promotor:

Prof. dr. J.W.M. Frenken

Co-promotor:

Prof. dr. P.J. Kooyman *University of Cape Town, Kaapstad, Zuid-Afrika*

Promotiecommissie:

Prof. dr. E.J.M. Hensen Technische Universiteit Eindhoven Prof. dr. P.E. de Jongh Universiteit Utrecht Prof. dr. J. Aarts Prof. dr. E.R. Eliel

Dr. I.M.N. Groot

ISBN: 978-90-8593-323-6 Casimir PhD series, Delft-Leiden 2017-39

The work in this thesis has been performed at the Huygens-Kamerlingh Onnes Laboratory, Leiden Institute of Physics, Leiden University, Leiden, The Netherlands, and at the Zandbergen Lab, Department of Quantum Nanoscience, Kavli Institute of Nanoscience, Delft University of Technology, Delft, The Netherlands. The work has been financially supported by the Netherlands Organisation for Scientific Research (NWO/OCW), as part of the Frontiers of Nanoscience (NanoFront) program. For a description of the cover illustration and all other illustrations in this PhD thesis, see Chapter 'About the illustrations in this thesis' on page 91.



Table of Contents

1.	Introd	uction 1
	1.1 V	Why is catalysis important?
	1.2 R	esearch in catalysis, then and now
	1.3 T	EM investigation on MoS_2 catalysts
	1.4 In	a situ and operando TEM
	1.5 C	Operando TEM experiments of Co nanoparticles
	1.6 D	Developments of other <i>in situ</i> techniques
2.	conditate and X-	ility of NiMoS ₂ and CoMoS ₂ hydrodesulfurization catalysts at ambient ions: A quasi <i>in situ</i> High-Resolution Transmission Electron Microscopy Ray Photoelectron Spectroscopy study
	2.1 In	ntroduction
	2.2 E	xperimental
	2.2.1	Preparation of catalysts
	2.2.2	Exposure to ambient air
	2.2.3	Characterization of catalysts
	2.3 R	esults and discussion
	2.3.1	Imaging and slab length analysis
	2.3.2	X-ray Photoelectron Spectroscopy
	2.3.3	Proposed oxidation mechanism
	2.4 C	Conclusion
3.	The ef	fect of oxidation and resulfidation on (Ni/Co)MoS ₂ hydrodesulfurization sts
	3.1 In	ntroduction
	3.2 E	xperimental
	3.2.1	Preparation of catalysts
	3.2.2	TEM and XPS characterization of catalysts
	3.2.3	Catalytic activity
	3.3 R	esults and discussion
	3.3.1	Imaging and slab length analysis
	3.3.2	Chemical state of the catalysts
	3.3.3	Catalytic activity
	3.3.4	
	3.4 C	Conclusion 44

4.	Cobalt- chemist	rhenium β -Mn-type bimetallic nanoparticles prepared via try	colloidal 49
	4.1 In	troduction	50
	4.2 Ex	operimental	50
		Synthesis of Co-Re nanoparticles	
	4.2.2	Nanoparticle characterization	
	4.3 Re	esults and discussion	
	4.3.1	Characterization of Co-Re nanoparticles	52
	4.3.2	Varying the Co-Re composition	55
	4.3.3	High Re content	57
	4.3.4	Thermal stability	58
	4.4 Co	onclusion	58
5.	formati	TEM observation of the Boudouard reaction: multi-layered good from CO on cobalt nanoparticles at atmospheric pressure	65
		troduction	
		perimental	
		Cobalt nanoparticles	
	5.2.2	Nanoreactors	
		<i>In situ</i> TEM holder	
	5.2.4	Gas supply system and residual gas analysis	
	5.2.5	Transmission Electron Microscopy	69
	5.3 Re	esults and discussion	
	5.3.1	Nanoparticle preparation	69
	5.3.2	Carbon deposition	71
	5.3.3	Effect on the nanoparticles	75
	5.3.4	Carbon morphologies	76
	5.4 Co	onclusion	77
Su	ımmary		83
Sa	menvatt	ing	87
Αŀ	oout the	illustrations in this thesis	91
Αc	cknowle	dgements	93
	ırriculur		95
		dications	97
1.39	St Of 12111	III CALIOUS	9/





CHAPTER 1

Introduction

1.1 Why is catalysis important?

Catalysis pervades our daily lives in countless ways. Some applications of catalysts are well-known, for example the three-way catalytic converters that are mounted on the exhausts of our cars. By using these, we try to make the impact of our cars on the environment less severe. Harmful and toxic gases are removed, as the catalyst converts these into less dangerous products.[1] Also, the fuel that we put into our cars is processed and cleaned thoroughly by a series of catalytic treatments, as it originates mostly from crude oil, which is contaminated (e.g. with sulfur, as we will see below). Not only the automotive industry exploits catalysts: the pharmaceutical industry, chemical plants, food processing industries, the production of polymers, they all rely on catalysts to make their production process easier, more energy efficient, and overall cleaner.[2,3]

Why are catalysts so special, why are they popular in all these processes and why are so many industries dependent on them? The reason for this is rooted in the working principle behind catalysis in general. A catalyst can enable or improve a chemical reaction between two (or more) reactants. Various aspects of a chemical reaction can be improved by adding a catalyst, for example the reaction rate, the selectivity, and the energy required to let the reaction take place.

In heterogeneous catalysis for example, when two reactants react with each other to form a product, a type of catalyst that is frequently used consists of metal nanoparticles, supported on a high surface-area metal oxide material. The surface of the metal nanoparticles facilitates the adsorption of the reactant molecules, allows them to react, and subsequently releases the newly formed molecules. The reactant molecules can be in gas or in liquid phase, while gaseous reactants could also form liquid phase products, for example in the Fischer-Tropsch process, which is the formation of liquid hydrocarbons from CO and H₂ gas. Different types of metals have different properties, so a chemical reaction that will take place on the surface of a nickel nanoparticle, might not necessarily give the same result on e.g. a platinum nanoparticle. Also, the catalytic properties of a metal nanoparticle can be altered by mixing multiple metallic elements into an alloy, by changing the support material carrying the nanoparticles, or by varying the size or shape of the nanoparticles.[4-9]

The performance of a catalytic system can therefore be tuned by actively changing the parameters mentioned above. These adjustments might result in a catalyst that is more active, has a longer lifetime before becoming inactive, or requires less energy to yield the same result (e.g. to require a lower operating temperature or pressure of the reactants). Also, the selectivity of the chemical reaction can be tuned, so that more of the desired end products are formed, while side product formation is suppressed.

As catalysts are used so abundantly, even the smallest improvements can lead to significant savings in energy, materials, or other costs. For this reason there is an ongoing effort in academia and industry to try and improve the catalysts used in their processes.

1.2 Research in catalysis, then and now

The search for better catalysts has evolved significantly since the early days of industrial catalysis. In the beginning of the 20th century, Fritz Haber, now famous

for the Haber-Bosch process that enables the production of ammonia from nitrogen and hydrogen, was looking for ways to improve his catalyst. [10] At that time, the best catalyst available for ammonia synthesis was manganese, while iron and nickel were slightly worse. As a catalyst, manganese did the job but there was still much room for improvement.

In a paper published by Haber and his colleague Le Rossignol in 1913, they describe their efforts and approach: "In our searching the elements for their capability to catalytically accelerate the formation of ammonia from its elements, we were led by the periodic table".[11] Their first plan was to go down in the column that contained manganese, but the periodic table was still empty there as technetium and rhenium were not yet identified at that time. So they needed a different approach. It was known that chromium, one place to the left of manganese, had similar catalytic properties. They started investigating tungsten, and even tried uranium, which turned out to be a "surprising success". After testing the elements located near manganese in the periodic table, their conclusion was that "both in the iron column as in the manganese column, the catalytic ability greatly increases with increasing atomic weight". In the end, Carl Bosch, working at BASF at that time and appointed to scale up the production of ammonia and design an industrial process, decided that the catalyst of choice would be iron, because it proved to be "particularly trustworthy and promising". Today, over a hundred years later, the Haber-Bosch process still uses iron catalysts, often mixed with small amounts of other metal-oxides such as potassium.[12]

This history shows that Haber and Le Rossignol first identified their starting point and from there on systematically tried different materials, which illustrates that they were led by certain trends in the materials they investigated. One trend they discovered was the increasing "catalytic ability" for ammonia synthesis as the atomic weight of the catalyst material increased. These trends in catalytic performance are nowadays thoroughly documented, and some of these trends are based on the so-called Sabatier principle. The Sabatier principle describes the binding strength of a reactant molecule to the surface of a catalyst, which depends on the adsorption energy of that specific reactant to that material. The best catalyst for a certain reaction binds molecules with an optimal strength. If the molecular adsorption energies are too low, the reactant molecules will not bind well enough to the catalyst and may not dissociate as a first step towards the reaction product. Also if the adsorption is too strong, reactions may be inhibited and, in addition, the catalyst surface will get poisoned rapidly with strongly bound reactant or product molecules. Different metals have different binding energies, and this effect is often displayed in graphs, showing the reaction rate versus the adsorption energy of different catalyst materials. Often, the shapes of these plots resemble a mountain, for example going from low via optimal to high binding energies, and they are referred to as 'volcano plots'. The material at the top of the volcano shows the best reaction rate and has the optimal balance between adsorption of reactants and desorption of products for that specific chemical reaction.

Research methods based on trial and error, similar to the approach followed by Haber and Le Rossignol, were common among scientists in the early 20th century. As technology developed further, more advanced techniques and methods to study catalysts became available, providing novel insights. The development of electron

microscopy in the 1930s allowed researchers to visualize their catalyst samples in unprecedented detail. In 1940, von Ardenne and Beischer published a paper in Angewandte Chemie, describing the power of transmission electron microscopy (TEM) and its use in catalysis research. They were able to show structural and morphological details of platinum, nickel, and iron catalysts, and investigate the support material.[13] To study the effect of real chemical reaction conditions on catalysts, scientists started to compare freshly prepared samples with samples that had been used for catalysis. For example, by using scanning electron microscopy (SEM), it became evident that platinum catalyst microparticles used for the gasphase CO oxidation reaction changed significantly. On the initially smooth surface of the particle, large uneven protrusions had been formed after exposure to reaction conditions (i.e. high temperature and high CO pressure).[14]

This type of research, comparing the catalyst before and after the chemical reaction has taken place, is referred to as post-mortem analysis. Even though this approach cannot reveal all aspects of how the catalysts change their structure during the chemical reaction, it has served as a very valuable first step, for example providing insight in catalyst deactivation. [15] This has been useful in the design of new, improved types of catalysts.

1.3 TEM investigation on MoS₂ catalysts

In the work described in the first two chapters of this thesis, we used this traditional approach and implemented an additional feature. Using special TEM mixed mesh sample finder grids to support our catalyst sample, we were able to find back and image exactly the same areas of the catalyst before and after the sample was exposed to ambient air. We were able to determine the effect of ambient air exposure was on individual catalyst particles. As a catalyst, we studied $(Ni/Co)MoS_2$ supported on high surface-area γ -Al₂O₂.

(Ni/Co)MoS₂ catalysts are widely used for the hydrodesulfurization (HDS) of fossil fuel. The HDS reaction is a process designed to clean crude oil when it is converted into fuel: it is used to remove sulfur from the oil feed so that these contaminants do not end up in our atmosphere when the fuel is burnt.[16]

However, this approach to catalyst evolution leaves one of the most important question unanswered: What happens with a catalyst *during* the reaction? To answer this question, the experimentalist would need to apply elevated gas pressures and high temperatures, in order to provide conditions similar to those inside a genuine chemical plant, while the catalyst is being investigated for changes in structure and composition. These types of experiments, in which data are collected on the behavior of the sample during the course of the process, are called *in situ* experiments. When also the catalytic performance of the sample is evaluated by monitoring the composition of the gas that has been in contact with the catalyst, e.g. by using mass spectrometry, they are referred to as *operando* experiments.[17]

Early studies, combining traditional post-mortem TEM experiments on platinum catalysts with e.g. *in situ* Auger electron spectroscopy, a technique already available in the 1970s,[18] provided new insight in catalyst regeneration and emphasized the need for and value of *in situ* electron microscopy techniques.[19]

It could be argued that catalysts can also be studied under low-pressure and low-

temperature conditions, since the species involved in a catalytic reaction can have identical chemical potentials both under regular reaction conditions, i.e. the combination of a high temperature and a high pressure,

and at the combination of a low, e.g. cryogenic temperature and a low pressure, e.g. ultra-high vacuum conditions (UHV, working pressure ~1.0 × 10⁻⁹ mbar). What is kept equal by changing temperature and pressure such that the chemical potentials remain the same, are all thermodynamic equilibria between the reactants, products and intermediate stages. This is very attractive, since the lower-temperature, lowerpressure conditions are usually much more accessible to high-resolution surfacescience techniques. However, what this approach ignores is the important role of the kinetics in the investigated catalytic processes. There are two general ways in which the kinetics can bring the system so far out of thermodynamic equilibrium that keeping the chemical potentials unchanged is no guarantee for keeping the surface in the same structure and composition. The first is that in the dynamic situation of genuine reaction conditions, the combination of the reaction itself, the supply of the reactants and the removal of the products continuously keeps the reactants, the intermediate products and the final product(s) away from thermodynamic equilibrium with each other. The catalyst in its working state should be regarded as one of these intermediate products. It is evident that slowing down the kinetics may bring the system closer to thermodynamic equilibrium, but this will then bring it away from the truly active state of the catalyst. The other kinetics problem arises when the lower pressures that may be necessary for certain measurement techniques thermodynamically correlates with a temperature that is so much lower, that one or more steps in the catalytic process effectively comes to a standstill, simply because the associated activation energy is too high to be overcome frequently enough to reach equilibrium on a reasonable time scale. A typical example is the case where reactant molecules adsorb on a surface at cryogenic temperatures, after which 'nothing' happens, i.e. no bond breaking, no diffusion, no compound formation and no desorption. Obviously, this is not the equilibrium situation, but the time to reach equilibrium would be unacceptably long. There is no alternative, in situ and operando experiments are really needed.

1.4 *In situ* and operando TEM

Switching from traditional TEM experiments to catalytically more relevant *in situ* TEM is not trivial. The reason for this lies in the working principle of a transmission electron microscope, as schematically shown in Figure 1.1.

A beam of electrons is generated at the top of the microscope by the electron gun. This e-beam travels down along the center of the column, meanwhile being manipulated by sets of electromagnetic lenses that are able to focus the electron beam at the sample. The sample is mounted on the tip of a holder which is introduced into the TEM column via a loadlock. The electrons transmitted through the sample continue downward, again being manipulated by electron lenses, and are finally detected by the CCD camera placed at the bottom of the column. Apertures are placed at several positions along the Y-axis to regulate the intensity of the e-beam and to block out electrons traveling too far away from the optic axis, reducing the noise.

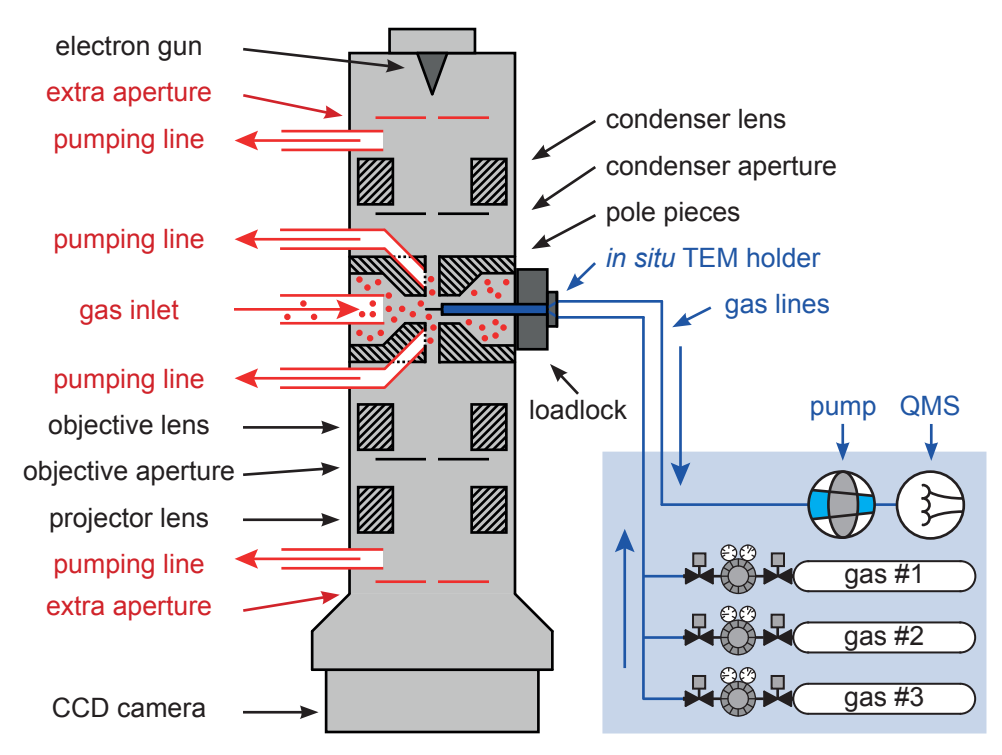


Figure 1.1. Schematic cross section of a transmission electron microscope, showing all the parts of a traditional TEM in black and gray, while the additional parts that make up an environmental TEM are shown in red. The gas flow equipment and gas lines that cover the *in situ* part are shown in blue, to the right of the TEM.

The electrons will be scattered by anything that is placed in between the gun and the camera. For that reason the column is constantly pumped down to a working pressure of $\sim 1.0 \times 10^{-7}$ mbar, thereby reducing unintentional scattering by collisions of electrons with gas molecules and enhancing the resolution of the image. This low pressure is also necessary for the electron gun, as this sensitive component is easily destroyed by any gas molecules that come into contact with it. Additional pumps placed next to the electron gun ensure a local pressure of below $\sim 1.0 \times 10^{-8}$ mbar. The sample that is loaded into the column via the airlock inherently also meets this low pressure environment. Imaging catalyst samples at higher pressures or even under reactant gas conditions therefore requires a different approach.

One way of realizing an elevated gas pressure at the sample while the rest of the TEM column remains at a reasonably low pressure is by using a differentially pumped environmental TEM (ETEM, Figure 1.1, parts outlined in red).[20-22] A gas feed is placed in the column of the ETEM, with the gas inlet placed directly next to the sample. The gas is inserted through the inlet and fills up the volume around the sample and sample holder, in between the pole pieces (Figure 1.1, red dots indicate gas molecules). To prevent the gas from diffusing too much to the rest of the TEM column, extra apertures are placed above and below the pole pieces. Main pumping lines are placed in the pole pieces to remove the majority of the gas, while extra

pumping lines above and below the pole pieces remove the diffused excess gas and thereby keep the pressure at the vulnerable electron gun low. This approach of additional apertures and differential pumping also increases the mean free path of the electrons in the column by reducing unintentional

increases the mean free path of the electrons in the column by reducing unintentional scattering.

The main drawback of this technique is the pressure range in which an ETEM can be operated. Despite the restricted volume that the gas is contained in, a too high gas pressure deteriorates the imaging resolution by scattering the electrons. This already occurs above a local pressure of 5 mbar, yielding blurred micrographs, while prolonged exposure to pressures above 50 mbar will destroy the electron gun.[20,23]

To overcome this restriction, a different approach was taken. Windowed cell systems were developed, which were able to contain both the catalyst sample and the reactant gases in a small volume, greatly reducing the electron path length through the gas layer. The cells, commonly referred to as nanoreactors, are currently available in a variety of versions. [24-30] The nanoreactors that were used in chapter 5 of this thesis consist of a single Si chip, prepared using MEMS technology (microelectromechanical systems), containing gas in- and outlets that are connected by a narrow channel. To use the nanoreactors in a TEM, a dedicated sample holder was developed simultaneously, containing a pair of capillaries running from the base of the holder to the tip. The nanoreactor is placed on two O-rings in the tip to ensure a leak-tight connection with the capillaries. Tube fittings at the base of the holder allow connections to a gas flow system of choice, and to a mass spectrometer to analyze the exhaust gas. A more detailed description of the components, including images of both the nanoreactors and the TEM holder, can be found in sections 5.2.2. - 5.2.4. The pressure regime in which this specific combination of tools can be operated ranges from vacuum up to 14 bar, making it a suitable approach to study a broad range of catalysts under their industrially relevant conditions.

1.5 Operando TEM experiments of Co nanoparticles

Chapter 5 of this thesis describes the experiments that we performed using the operando TEM tools described above, showing atomic scale images of cobalt nanoparticles at 1 bar pressure and elevated temperature. Cobalt nanoparticles are used as catalysts in the Fischer-Tropsch process. This process, currently running commercially at an industrial scale worldwide, transforms a mixture of CO and $\rm H_2$ gas into liquid hydrocarbons. These hydrocarbons can then be used as a renewable, synthetic fuel source, instead of traditional fossil fuel.

The cobalt nanoparticles were prepared via colloidal chemistry, allowing accurate control over the size distribution in which the resulting nanoparticles are synthesized.[31] This colloidal approach was also used to synthesize cobalt-rhenium bimetallic nanoparticles of varying composition. A thorough investigation of the cobalt-rhenium nanoparticles is described in chapter 4. A range of TEM techniques (scanning transmission electron microscopy - energy dispersive X-ray spectroscopy (STEM-EDX), high-angle annular dark field (HAADF) and regular HRTEM(-EDX)) was exploited to characterize the nanoparticles, revealing the atomic composition and distribution of the metals inside the particles.

1.6 Developments of other *in situ* techniques

The development of the traditional TEM into an instrument that is able to perform *in situ* and operando experiments is part of a broader progress. Inspired by early surprises in this field of research and supported by considerations such as those given in section 1.3, a growing number of instruments and measurement techniques is being made suitable for operation under catalytic reaction conditions.[32] As each individual technique and instrument only approaches the catalyst sample from a relatively narrow point of view, the results of single experiments show a rather limited part of the picture. Therefore, in order to fully investigate the catalytic process in all its aspects, it is essential to combine multiple approaches and apply different techniques on a catalyst sample.

Surface science laboratories, traditionally working with UHV setups containing surface sensitive equipment such as scanning tunneling microscopy (STM) and atomic force microscopy (AFM), have made vast progress by implementing small, high-pressure gas flow cells inside the UHV setup.[33,34] This approach allows flowing reactant gases over heated metal single crystal surfaces and observing the effect of these conditions on the metal surface. Recent publications reveal the power of these setups by yielding atomic-scale insight into catalytic reactions such as the Fischer-Tropsch reaction on a cobalt surface,[35] and CO oxidation and NO reduction on platinum.[36] X-ray techniques such as surface X-ray diffraction (SXRD) and X-ray absorption spectroscopy (XAS), traditionally limited to UHV conditions, are currently also being modified for *in situ* experiments, to acquire information about the geometrical structure, elemental composition and electronic structure of the surface.[37,38]. In some experiments, *in situ* X-ray techniques are used in direct combination with a second *in situ* technique to instantly benefit from both approaches.[39,40]

That also simpler and cheaper methods can be used to investigate surfaces under genuine catalytic conditions is illustrated by a recent investigation [41] in which we collaborated with Leiden Probe Microscopy [42] to design, build and apply a small, relatively simple tabletop flow reactor for catalytic experiments. The reactor uses the reflection of visible light over a metal single crystal to see the effect of different gas conditions and sample temperatures on the reflectivity of the sample surface. This optical experiment provides direct information on the interplay between different regions on a catalyst that are in different chemical states due to subtle differences in local conditions, e.g. local partial pressures. Such information complements the highly local information that is acquired through the TEM experiments that form the main subject of this PhD thesis. As was remarked above already, we can only gain a complete understanding of the complex mechanisms of catalysis by combining information of many different types, for example on many different length scales. In this thesis we concentrate on the atomic scale.

Next to all the scientific images and graphs, this PhD thesis contains additional illustrations, mostly dedicated to the instrumentation that was used for the conducted experiments. These include the cover page, the starting pages of all chapters and the upper corner of all right pages. A brief explanation of these illustrations is provided in a separate section near the end of the thesis.

References

- [1] Farrauto, R. J.; Heck, R. M. Catalytic Converters: State of the Art and Perspectives. *Catal. Today* **1999**, *51* (3-4), 351–360 DOI: 10.1016/S0920-5861(99)00024-3.
- [2] Rabó, J. A. Chapter 1 Catalysis Overview. *Catal. Today* **1994**, 22 (2), 201–233 DOI: 10.1016/0920-5861(94)80102-9.
- [3] Armor, J. N. A History of Industrial Catalysis. *Catal. Today* **2011**, *163* (1), 3–9 DOI: 10.1016/j.cattod.2009.11.019.
- [4] Ferrando, R.; Jellinek, J.; Johnston, R. L. Nanoalloys: From Theory to Applications of Alloy Clusters and Nanoparticles. *Chem. Rev.* **2008**, *108* (3), 845–910 DOI: 10.1021/cr040090g.
- [5] Cuenya, B.R. Synthesis and Catalytic Properties of Metal Nanoparticles: Size, Shape, Support, Composition, and Oxidation Effects. *Thin Solid Films* **2010**, *518* (12), 3127–3150 DOI: 10.1016/j.tsf.2010.01.018.
- [6] Den Breejen, J.P.; Radstake, P.B.; Bezemer, G.L.; Bitter, J.H.; Frøseth, V.; Holmen, A.; De Jong, K.P. On the Origin of the Cobalt Particle Size Effects in Fischer-Tropsch Catalysis. *J. Am. Chem. Soc.* **2009**, *131* (20), 7197–7203 DOI: 10.1021/ja901006x.
- [7] Bell, A.T. The Impact of Nanoscience on Heterogeneous Catalysis. *Science* **2003**, 229 (5613), 1688–1691 DOI: 10.1126/science.1083671.
- [8] Comotti, M.; Li, W.-C.; Spliethoff, B.; Schüth, F. Support Effect in High Activity Gold Catalysts for CO Oxidation. *J. Am. Chem. Soc.* **2006**, 128 (3), 917–924 DOI: 10.1021/ja0561441.
- [9] Vayssilov, G. N.; Lykhach, Y.; Migani, A.; Staudt, T.; Petrova, G. P.; Tsud, N.; Skála, T.; Bruix, A.; Illas, F.; Prince, K. C.; *et al.* Support Nanostructure Boosts Oxygen Transfer to Catalytically Active Platinum Nanoparticles. *Nat. Mater.* **2011**, *10* (4), 310–315 DOI: 10.1038/nmat2976.
- [10] van Veen, J. A. R. What's New? On the Development of Sulphidic HT Catalysts Before the Molecular Aspects. *Catal. Today* **2017**, 292, 2–25 DOI: 10.1016/j. cattod.2016.09.027.
- [11] Haber, F.; Le Rossignol, R. Über Die Technische Darstellung Von Ammoniak Aus Den Elementen. *Ber. Bunsenges. Phys. Chem.* **1913**, 19 (2), 53–72 DOI: 10.1002/bbpc.19130190201.
- [12] Rodriguez, M. M.; Bill, E.; Brennessel, W. W.; Holland, P. L. N₂ Reduction and Hydrogenation to Ammonia by a Molecular Iron-Potassium Complex. *Science* **2011**, 334 (6057), 780–783 DOI: 10.1126/science.1211906.
- [13] Ardenne, von, M.; Beischer, D. Untersuchungen Von Katalysatoren Mit Dem Universal-Elektronenmikroskop. *Angew. Chemie* **1940**, *53* (9-10), 103–107 DOI: 10.1002/ange.19400530905.
- [14] Flytzani-Stephanopoulos, M.; Wong, S.; Schmidt, L. D. Surface Morphology of Platinum Catalysts. *J. Catal.* **1977**, 49 (1), 51–82 DOI: 10.1016/0021-9517(77)90239-1.
- [15] Harris, P.; Boyes, E. D.; Cairns, J. A. The Sintering of an Alumina-Supported Platinum Catalyst Studied by Transmission Electron Microscopy. *J. Catal.* **1983**, *82* (1), 127–146 DOI: 10.1016/0021-9517(83)90124-0.

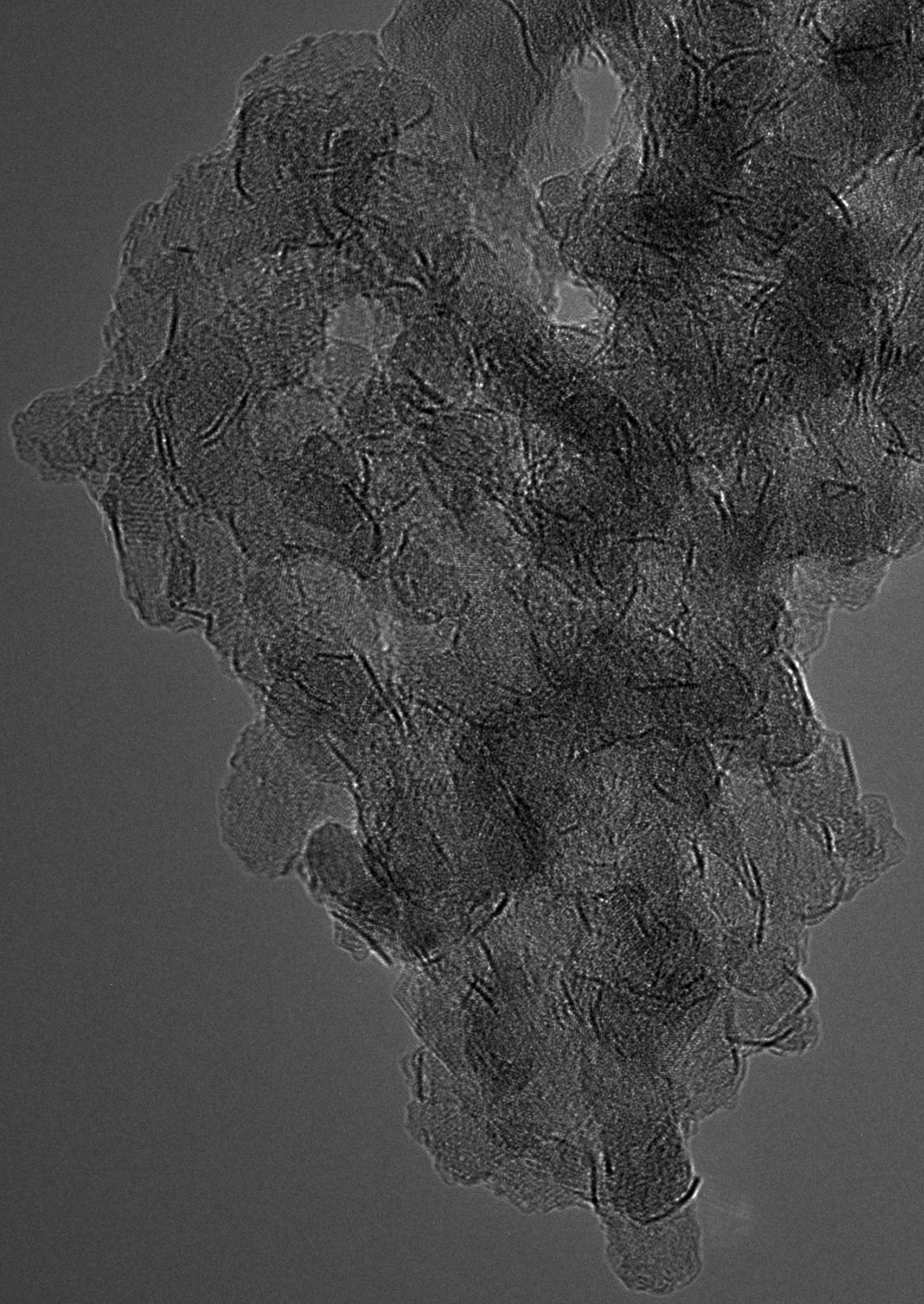
- [16] Eijsbouts, S.; Heinerman, J.; Elzerman, H. MoS₂ Structures in High Activity Hydrotreating Catalysts. II. Evolution of the Active Phase During the Catalyst Life Cycle. Deactivation Model. *Appl. Catal. A: Gen.* **1993**, *105* (1), 69–82 DOI: 10.1016/0926-860X(93)85134-B.
- [17] Topsøe, H. Developments in Operando Studies and *In Situ* Characterization of Heterogeneous Catalysts. *J. Catal.* **2003**, *216* (1-2), 155–164 DOI: 10.1016/S0021-9517(02)00133-1.
- [18] Tarng, M. L.; Wehner, G. K. Alloy Sputtering Studies with *In Situ* Auger Electron Spectroscopy. *J. Appl. Phys.* **1971**, 42 (6), 2449–2452 DOI: 10.1063/1.1660561.
- [19] Rickard, J. M.; Genovese, L.; Moata, A.; Nitsche, S. Redispersion of Platinum on Pt/Al₂O₃ Model Catalyst in Oxygen Studied by Transmission Electron Microscopy. *J. Catal.* 1990, 121 (1), 141–152 DOI: 10.1016/0021-9517(90)90224-8.
- [20] Hashimoto, H.; Naiki, T.; Eto, T.; Fujiwara, K. High Temperature Gas Reaction Specimen Chamber for an Electron Microscope. *Jpn. J. Appl. Phys.* **1968**, *7* (8), 946–952 DOI: 10.1143/JJAP.7.946.
- [21] Boyes, E. D.; Gai, P. L. Environmental High Resolution Electron Microscopy and Applications to Chemical Science. *Ultramicr.* **1997**, *67* (1-4), 219–232 DOI: 10.1016/S0304-3991(96)00099-X.
- [22] Sharma, R.; Weiss, K. Development of a TEM to Study *In Situ* Structural and Chemical Changes at an Atomic Level During Gas-Solid Interactions at Elevated Temperatures. *Microsc. Res. Tech.* **1998**, 42 (4), 270–280 DOI: 10.1002/(SICI)1097-0029(19980915)42:4<270::AID-JEMT6>3.0.CO;2-U.
- [23] Kooyman, P. J. Development of Operando Transmission Electron Microscopy. In Operando Studies in Heterogeneous Catalysis; Editors: Frenken, J. W. M., Groot, I. M. N.; **2017**; Springer Publishing, New York, pp 111–129. ISBN 978-3-319-44439-0.
- [24] Alsem, D.; Salmon, N. J.; Unocic, R. R. *In-Situ* Liquid and Gas Transmission Electron Microscopy of Nano-Scale Materials. *Microsc. Microanal.* **2012**, *18* (2), 1158-1159 DOI: 10.1017/S1431927612007647.
- [25] Xin, H. L.; Niu, K.; Alsem, D. H.; Zheng, H. *In Situ* TEM Study of Catalytic Nanoparticle Reactions in Atmospheric Pressure Gas Environment. *Microsc. Microanal.* **2013**, 19 (6), 1558–1568 DOI: 10.1017/S1431927613013433.
- [26] Allard, L. F.; Overbury, S. H.; Bigelow, W. C.; Katz, M. B.; Nackashi, D. P.; Damiano, J. Novel MEMS-Based Gas-Cell/Heating Specimen Holder Provides Advanced Imaging Capabilities for *In Situ* Reaction Studies. *Microsc. Microanal.* **2012**, *18* (4), 656–666 DOI: 10.1017/S1431927612001249.
- [27] Allard, L. F.; Bigelow, W. C.; Zhang, S.; Pan, X. Controlled *In Situ* Gas Reaction Studies of Catalysts at High Temperature and Pressure with Atomic Resolution. *Microsc. Microanal.* **2014**, 20 (3), 1572–1573 DOI: 10.1017/S1431927614009593.
- [28] Website DENSsolutions: http://www.denssolutions.com/products/climate/ Last consulted: 05-July-2017
- [29] Creemer, F.; Santagata, F.; Morana, B.; Mele, L.; Alan, T.; Iervolino, E.; Pandraud, G.; Sarro, P. M. An All-in-One Nanoreactor for High-Resolution Microscopy on Nanomaterials at High Pressures. *MEMS* **2011**, 1103–1106 DOI: 10.1109/MEMSYS.2011.5734622.

- [30] Vendelbo, S. B.; Elkjær, C. F.; Falsig, H.; Puspitasari, I.; Dona, P.; Mele, L.; Morana, B.; Nelissen, B. J.; van Rijn, R.; Creemer, F.; et al. Visualization of Oscillatory Behaviour of Pt Nanoparticles Catalysing CO Oxidation. *Nat. Mater.* **2014**, *13* (9), 884–890 DOI: 10.1038/nmat4033.
- [31] Zacharaki, E.; Kalyva, M.; Fjellvåg, H.; Sjåstad, A. O. Burst Nucleation by Hot Injection for Size Controlled Synthesis of ε-Cobalt Nanoparticles. *Chem. Cent. J.* **2016**, *10* (1), 10 DOI: 10.1186/s13065-016-0156-1.
- [32] Operando Studies in Heterogeneous Catalysis; Editors: Frenken, J. W. M., Groot, I. M. N.; **2017**; Springer Publishing, New York. ISBN 978-3-319-44439-0.
- [33] Herbschleb, C. T.; van der Tuijn, P. C.; Roobol, S. B.; Navarro, V.; Bakker, J. W.; Liu, Q.; Stoltz, D.; Cañas-Ventura, M. E.; Verdoes, G.; van Spronsen, M. A.; *et al.* The ReactorSTM: Atomically Resolved Scanning Tunneling Microscopy Under High-Pressure, High-Temperature Catalytic Reaction Conditions. *Rev. Sci. Instrum.* **2014**, *85* (8), 083703 DOI: 10.1063/1.4891811.
- [34] Roobol, S. B.; Cañas-Ventura, M. E.; Bergman, M.; van Spronsen, M. A.; Onderwaater, W. G.; van der Tuijn, P. C.; Koehler, R.; Ofitserov, A.; van Baarle, G. J. C.; Frenken, J. W. M. The ReactorAFM: Non-Contact Atomic Force Microscope Operating Under High-Pressure and High-Temperature Catalytic Conditions. *Rev. Sci. Instrum.* **2015**, *86* (3), 033706 DOI: 10.1063/1.4916194.
- [35] Navarro, V.; van Spronsen, M. A.; Frenken, J. W. M. *In Situ* Observation of Self-Assembled Hydrocarbon Fischer-Tropsch Products on a Cobalt Catalyst. *Nat. Chem.* **2016**, *8* (10), 929–934 DOI: 10.1038/nchem.2613.
- [36] van Spronsen, M. A.; van Baarle, G. J. C.; Herbschleb, C. T.; Frenken, J. W. M.; Groot, I. M. N. High-Pressure Operando STM Studies Giving Insight in CO Oxidation and NO Reduction Over Pt(110). *Catal. Today* **2015**, 244, 85–95 DOI: 10.1016/j.cattod.2014.07.008.
- [37] van Haandel, L.; Hensen, E. J. M.; Weber, T. High Pressure Flow Reactor for *In Situ* X-Ray Absorption Spectroscopy of Catalysts in Gas-Liquid Mixtures a Case Study on Gas and Liquid Phase Activation of a Co-Mo/Al₂O₃ Hydrodesulfurization Catalyst. *Catal. Today* **2017**, 292, 51–57 DOI: 10.1016/j.cattod.2016.08.027.
- [38] Onderwaater, W. G.; Balmes, O.; Roobol, S. B.; Van Spronsen, M.; Drnec, J.; Carla, F.; Felici, R.; Frenken, J. W. M. Oxidation of CO on Pd(100): on the Structural Evolution of the PdO Layer During the Self Sustained Oscillation Regime. *Catal. Struct. React.* **2017**, *3* (1-2), 89–94.
- [39] Roobol, S. B.; Onderwaater, W. G.; van Spronsen, M. A.; Carla, F.; Balmes, O.; Navarro, V.; Vendelbo, S.; Kooyman, P. J.; Elkjær, C. F.; Helveg, S.; *et al. In Situ* Studies of NO Reduction by H₂ Over Pt Using Surface X-Ray Diffraction and Transmission Electron Microscopy. *Phys. Chem. Chem. Phys.* **2017**, *19* (12), 8485–8495 DOI: 10.1039/c6cp08041c.
- [40] Mom, R. V.; Onderwaater, W. G.; Rost, M. J.; Jankowski, M.; Wenzel, S.; Jacobse, L.; Alkemade, P. F. A.; Vandalon, V.; van Spronsen, M. A.; van Weeren, M.; et al. Simultaneous Scanning Tunneling Microscopy and Synchrotron X-Ray Measurements in a Gas Environment. *Ultramicroscopy* **2017**, *182*, 233–242 DOI: 10.1016/j.ultramic.2017.07.011.
- [41] Onderwaater, W. G.; Taranovskyy, A.; Bremmer, G. M.; van Baarle, G. C.;

Frenken, J. W. M.; Groot, I. M. N. From Dull to Shiny: a Novel Setup for Reflectance Difference Analysis Under Catalytic Conditions. *Rev. Sci. Instrum.* **2017**, *88* (2), 023704 DOI: 10.1063/1.4975930.

[42] Website Leiden Probe Microscopy: http://www.leidenprobemicroscopy.com/ Last consulted: 05-Sept-2017





CHAPTER 2

Instability of NiMoS₂ and CoMoS₂ hydrodesulfurization catalysts at ambient conditions: A quasi *in situ* High-Resolution Transmission Electron Microscopy and X-Ray Photoelectron Spectroscopy study

The effect of exposure to ambient air of MoS₂-based, γ-Al₂O₃-supported HDS catalysts has been studied using HRTEM. Analysis of unpromoted as well as Ni-and Co-promoted MoS₂ samples showed that the number of MoS₂ slabs and the average slab length decreased as a function of air exposure time. A parallel XPS study showed this effect to be due to oxidation. During the first 24 h of exposure to air, all 1 bar sulfided (Ni/Co)MoS₂ samples showed an initial slab length decrease of around 20%. After an additional month in air, the slabs had deteriorated significantly further. A sample of CoMoS₂, sulfided at 30 bar, showed a slightly enhanced effect of oxidation, particularly after the first 5 minutes in air. The data obtained in this study emphasize the general necessity of shielding vulnerable catalyst samples from air during preparation and characterization, a message relevant in all fields of research covering catalysis.

2.1 Introduction

Current environmental legislation pushes oil refiners toward producing transportation fuels with progressively lower sulfur levels in order to limit the emission of harmful sulfur-containing exhaust gases into the atmosphere.[1] The main reaction used to remove organosulfur compounds from oil feedstock is the catalytic hydrodesulfurization (HDS) reaction. The industrial HDS catalysts used most for this purpose are based on MoS,, present in the form of nanometer-sized slabs dispersed on a high-surface-area support, such as γ-Al,O₃.[2] MoS, catalyst slabs consist of one layer of molybdenum atoms sandwiched between two layers of sulfur atoms. [2-4] MoS₂ is also being studied as a material with interesting electrical properties (e.g., to be used as a semiconductor material in nanoelectonics [5-8]. It has applications in photocatalysis, [9,10] and MoS, is used as a solid lubricant. [11-13] Research on MoS, has been a long ongoing effort, in which a wide variety of characterization techniques have been used. In 2008, Kooyman and van Veen reported the importance of shielding γ-Al₂O₂-supported MoS₂ catalysts from ambient air between preparation and characterization.[14] Their transmission electron microscopy (TEM) study indicated that exposing MoS, samples to ambient air leads to deterioration of the catalyst slabs, but no mechanism for this phenomenon was proposed.

Promoting MoS₂-slabs with metal atoms such as nickel or cobalt has the effect of enhancing the catalytic activity of the catalyst, as well as influencing the specific selectivity.[15-17] The influence of the incorporated promoter atoms on the stability of the catalyst slabs has not yet been studied. The effect of the promoter atoms could be stabilizing, causing the slabs not to deteriorate because of mere exposure to ambient conditions, but the effect might also cause less stability in air, as the promoted catalyst slabs are more reactive in general because of the presence of more coordinatively unsaturated sites.

We have investigated this issue by using quasi *in situ* high-resolution transmission electron microscopy (HRTEM) to monitor the effect of ambient air on NiMoS₂, CoMoS₂, and MoS₂ samples sulfided at 1 bar. After preparation of the samples, special care was taken to prevent contact with air during transportation and prior to the TEM imaging. We determined the average length and stacking of the catalyst slabs for each sample after the first TEM measurements, without contact with ambient air, as well as after 24 h and after 1 month of air exposure. Because many industrial processes using these catalysts are operated at high pressures (30-100 bar), a Co-promoted MoS₂-catalyst was sulfided at 30 bar for comparison. A parallel quasi *in situ* X-ray photoelectron spectroscopy (XPS) study was performed to monitor the chemical changes of the catalyst, following the same approach of air exposure.

2.2 Experimental

2.2.1 Preparation of catalysts

The four catalyst samples were prepared by incipient-wetness coimpregnation of Ketjen CK-300 γ -Al₂O₃ extrudates (SBET = 250 m²/g, Vpore = 0.66 mL/g), which were crushed and sieved to a 125-250 μ m fraction prior to impregnation. Different aqueous solutions containing cobalt(II) nitrate (Co(NO₃)₂ 6H₂O, Merck), nickel-

(II) nitrate (Ni(NO₃)₂ 6H₂O, Merck), ammonium heptamolybdate ((NH₄)₆Mo₇O₂₄ 4H₂O, Merck), and nitrilotriacetic acid (NTA, (C₂H₃O₂)₃N, Merck) were prepared to obtain catalysts with 8 wt % Mo and 1.5 wt

% Co or Ni for the promoted catalysts. The molar ratio of NTA:Mo was 1.2:1. All catalyst precursors were dried at room temperature for 1 h, dried in static air at 100 °C overnight, and finally calcined at 450 °C (heating rate, 6 °C/min) in flowing air for 4 h. The catalyst precursors were sulfided at 350 °C (heating rate, 6 °C/min) for 2 h in $\rm H_2/\rm H_2S$ 9:1 (Scott), in a flow of 60 mL/min STP at a total pressure of 1 or 30 bar. The samples sulfided at 1 bar are termed NiMoS₂, CoMoS₂, and MoS₂, while the Copromoted sample sulfided at 30 bar is termed CoMoS₂-30. After preparation, each sample was collected in a glass vial, which was filled with N₂ and sealed airtight for transportation.

2.2.2 Exposure to ambient air

The vials containing the sulfidic catalysts were opened in an Ar-filled glovebox (concentrations of $\rm H_2O$ and $\rm O_2$ < 1 ppm), after which the samples were mounted on TEM grids as described below. After the first quasi *in situ* TEM study of the samples, without any exposure to air, the samples on the TEM grids were left on an office desk in a small nonairtight plastic box, to prevent accumulation of dust but to allow exposure to ambient air. This procedure is very similar to the storage of larger samples of catalyst in containers on a shelf and is different from passivation. For passivation, a material is first exposed to a low, controlled, concentration of oxygen *before* being exposed to ambient air. For many materials this creates a protective oxide layer that prevents further oxidation and can be removed by mild reduction.

2.2.3 Characterization of catalysts

Quasi *in situ* TEM was carried out using an FEI monochromated Tecnai F20ST/STEM electron microscope, operated at an accelerating voltage of 200 keV, in bright field TEM mode. Images were obtained using a Gatan Ultrascan CCD camera (4k × 4k).

The vials containing the prepared samples were opened in an Ar-filled glovebox (concentrations of $\rm H_2O$ and $\rm O_2 < 1$ ppm), after which the samples were crushed in n-hexane using a mortar and pestle, creating a suspension. A few drops of the suspension were placed on a Quantifoil microgrid carbon-film covered mixed mesh Au TEM grid and, after evaporation of the solvent at room temperature, the grid was placed in a protective atmosphere transfer TEM specimen holder.[18] This holder was inserted into the glovebox via an air-lock. The holder was then closed (the sample compartment is sealed by a Viton O-ring), removed from the glovebox air-lock, and transferred to the TEM for imaging. Once the holder was inserted in the TEM air-lock, one 3 min pumping cycle was started while the holder was still closed, and the sample compartment of the holder was opened at the beginning of a second 3 min pumping cycle.

Samples were imaged quasi *in situ* (t = 0, without exposure to air), after 24 h of exposure to air (t = 24 h), and after 1 month in air (t = 1 month). The CoMoS₂-30 sample was also imaged after 5 min in air (t = 5 min). The average slab length of each sample was determined for quantitative analysis. Qualitative analysis was made possible by imaging identical regions of the samples at the different points in time.

To investigate possible effects of the high-energy electron beam on the sample, also control images of sample regions that had not been exposed to the electron beam before were recorded and analyzed.

The resulting images were analyzed using Gatan Digital Micrograph and ImageJ software. After the slabs were identified, the length of each slab was measured by hand using standard drawing tools in the software. Per sample, around 800 individual slabs were measured at t = 0. Due to the detrimental effect of ambient air on the slabs, at t = 24 h about 450 slabs per sample were left for analysis, while after 1 month in air only around 300 slabs were left for analysis in the same regions of the samples that had been studied before.

The same samples were analyzed with XPS using a Kratos AXIS Ultra spectrometer, equipped with a monochromatic X-ray source and a delay-line detector (DLD). To prevent contact with air, samples were transferred from the glovebox to the XPS in a closed, homemade transfer holder under N_2 atmosphere. Spectra were recorded using an aluminum anode (Al K α = 1486.6 eV). Survey scans were measured at constant pass energy of 160 eV and region scans at 40 eV. The background pressure was 2 × 10-9 mbar.

XP spectra were fitted with CasaXPS (version 2.3.16) by a nonlinear least-squares fitting algorithm using mixed Gaussian-Lorentzian (35/65) curves. Shirley background subtraction was applied, and the energy was calibrated using the Al 2p peak at 74.6 eV as a reference. The Mo 3d spectrum was fitted with Mo⁴⁺ (MoS₂), Mo⁵⁺ (MoS₂O₃), and Mo⁶⁺ (MoO₃) contributions, as well as with the overlapping S 2s (~226.5 eV) component. The Ni 2p and Co 2p spectra were fitted with a sulfidic M²⁺ contribution and an oxidic M²⁺ contribution (NiO, CoO). The sulfidic contribution was assigned to Ni or Co sulfides, either dispersed on the edges of MoS₂ particles or present as bulk metal sulfides (Ni₃S₂, Co₉S₈). Lastly, the S²⁻ and bridged S₂²⁻ anions, as well as sulfate (SO₄²⁻), were taken into account for fitting the S 2p spectra. The XPS fitting procedure is explained in more detail in a recent paper.[19] The respective binding energies of these components are listed in Table 2.1 and agree well with previously reported studies.[20-22]

Table 2.1. XPS Binding energies of the various species present in (Co/Ni)MoS₂, as determined by the fitting procedure described in the text.

	Mo ⁴⁺ (MoS ₂)	Mo^{5+} (MoS_xO_y)	Mo ⁶⁺ (MoO ₃)	S^{2-} (MS_x)	S_{2}^{2-} (MS _x)
BE $(eV)^a$	229.0	231.2	232.7	161.7	163.2
$\Delta \mathrm{BE} \; (\mathrm{eV})^b$	3.15	3.15	3.15	1.15	1.15
	S ⁶⁺ (SO ₄ ²⁻)	Co^{2+} $(CoS_x)^c$	Co ²⁺ (CoO) ^c	Ni^{2+} $(NiS_x)^c$	Ni ²⁺ (NiO) ^c
BE (eV) ^a	168.8	778.7	791.8	853.8	856.5
$\Delta \mathrm{BE} \; (\mathrm{eV})^b$	1.15	-	-	-	-

^a Binding energy of the $3d_{5/2}$ or $2p_{3/2}$ peak. Uncertainty ± 0.2 eV.

 $^{^{}b}\Delta BE(3d) = BE(3d_{3/2}) - BE(3d_{5/2}); \Delta BE(2p) = BE(2p_{1/2}) - BE(2p_{3/2}).$

^c Only the 2p_{3/2} peak was fitted for Co and Ni.

2.3 Results and discussion

2.3.1 Imaging and slab length analysis

A set of representative TEM images of the NiMoS, sample is shown in Figure 2.1, where the same γ-Al₂O₂ particle covered with NiMoS₂ slabs was imaged before any exposure to air, after 24 h in air, and after 1 month of exposure to air. It is immediately apparent that exposure to air leads to a decrease in the total number of visible slabs. For example, the slab that is indicated in the encircled region labeled "1" is present at t = 0 but has disappeared at t = 24 h. There are several other slabs that are present in the first image but are no longer visible after the sample has been exposed to ambient air. The second indication that the sample was affected by air is that the observed average length of the slabs is decreasing. The stack of multiple slabs in the encircled region labeled "2" is an example of this phenomenon. At t = 0, the stack consists of three slabs of approximately equal length. The length of the slabs decreases significantly upon exposure to air. It can also be noted that the substrate that carries the slabs seems to be changing simultaneously. Although this is not clearly visible in TEM imaging, the substrate material that supports the visible slabs does not consist solely of γ-Al₂O₂. It is actually γ-Al₂O₂ covered with more NiMoS₂ slabs that are oriented nonparallel with respect to the TEM electron beam and thus not clearly visible as slabs. Due to the planar layered structure of MoS, the only slabs that will be visible in the TEM two-dimensional projection are those that are oriented parallel, or slightly tilted (± several degrees) with respect to the electron beam.[23] As all NiMoS, slabs are influenced by ambient air, also the slabs that are not directly visible are changing. The result of this process is observed as changes in general morphology of the material surrounding and supporting the visible slabs, which is for example visible when comparing the edge structure of the particle in Figure 2.1 at the different stages of oxidation.

For the CoMoS₂, CoMoS₂-30, and MoS₂ samples, similar trends are found, with less and apparently shorter slabs being observed. All samples show slabs decreasing both in length as well as in number after exposure to air.

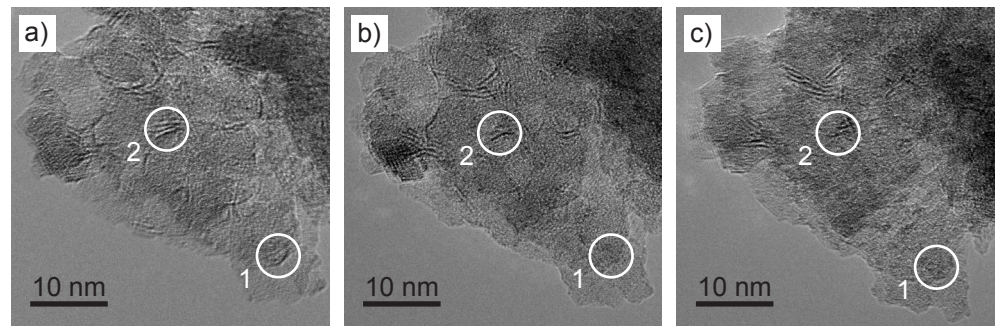


Figure 2.1. TEM images of a γ-Al $_2O_3$ particle covered with NiMoS $_2$ catalyst slabs: (a) prior to air exposure, (b) after 24 h of exposure to air, and (c) after 1 month in ambient air. Several catalyst slabs have disappeared after air exposure. The region labeled "1" shows a slab that has completely disappeared after 24 h of air exposure, while the region labeled "2" shows a stack of which the slabs have become shorter over time.

However, solely based on observations of a small number of slabs, no conclusions can be drawn. As the sample grid is taken out of the sample holder between the measurements, it might occur that a slab that was visible in the t=0 measurement is no longer visible during the t=24 h or t=1 month measurement because of a slight rotation of a part of the material. The opposite process might also occur, resulting in slabs appearing that were not visible before. Therefore, quantitative slab length analysis based on a large set of images is required. In this way, the random process of slabs appearing or disappearing due to changes in carrier material and observation angle will be averaged out.

For statistical analysis of the changes of the samples upon contact with air, all recorded images were analyzed and the lengths of all visible slabs were measured. For the $NiMoS_2$ sample, the t=0 measurement yielded 761 measured slabs, while the images of the same areas of the sample obtained after 24 h of air exposure showed 631 slabs for analysis. After 1 month in air, 585 slabs remained visible. The distribution of the recorded slab lengths is plotted as a histogram in Figure 2.2a.

The slab length distribution changes significantly after exposure to air. At t = 0, the slab length distribution is more evenly distributed over slab lengths between 1 and 3 nm, with a long tail stretching to 4.5 nm. At t = 24 h, the distribution of the histogram has mostly shifted to the regime between 1 and 2 nm, with a peak around 1.3 nm. This process continues during the 1 month of exposure to air, as is visible in the t = 1 month histogram. The number of slabs shorter than 1 nm has increased significantly, while the tail of the histogram decreases further. As the slabs get shorter, slabs that were initially relatively short (< 1 nm) disappear completely, explaining the decrease in the total number of observable slabs. The stacking degree of the slabs was also determined, resulting in an average stacking of 1.3 layers, which remained constant after exposure to air. Analysis of the other samples was performed in the same way, resulting in the histograms shown in Figure 2.2b-d. All samples show similar trends in slab length distribution, indicating that all samples are affected by exposure to air in a similar way, including the reference sample of unpromoted MoS₂ (Figure 2.2c).

When $CoMoS_2$ and $CoMoS_2$ -30 bar are compared, some differences are visible. The initial slab length distribution at t=0 shows a broader distribution for the 30 bar sulfided sample. At t=5 min, a shift is already visible in the distribution of the histogram, which indicates that only 5 min of exposure to air has an effect on the slabs. The distribution continues to shift after extended exposure to air. The calculated average slab lengths are shown in Table 2.2. Although $CoMoS_2$ -30 initially has a slightly higher average slab length value than the 1 bar sulfided $CoMoS_2$ sample, after exposure to air for 1 month the average slab lengths of both samples have decreased to similar values. The average slab length of $CoMoS_2$ -30 decreased faster than that of $CoMoS_2$. The average slab stacking degree was also determined for each sample, yielding similar values for all samples: around 1.3 ± 0.1 layers per cluster. These values remained constant during air exposure.

When the average slab length values per sample as a function of air exposure time is plotted, it is clear that all samples were affected (Figure 2.3). All samples showed a significant decrease in average slab length. Average slab length values were also determined from control images, obtained from areas that had not been exposed to the TEM electron beam before. The data are shown in Table 2.2. The t = 0 measurements did not require control data, because for these data the sample was

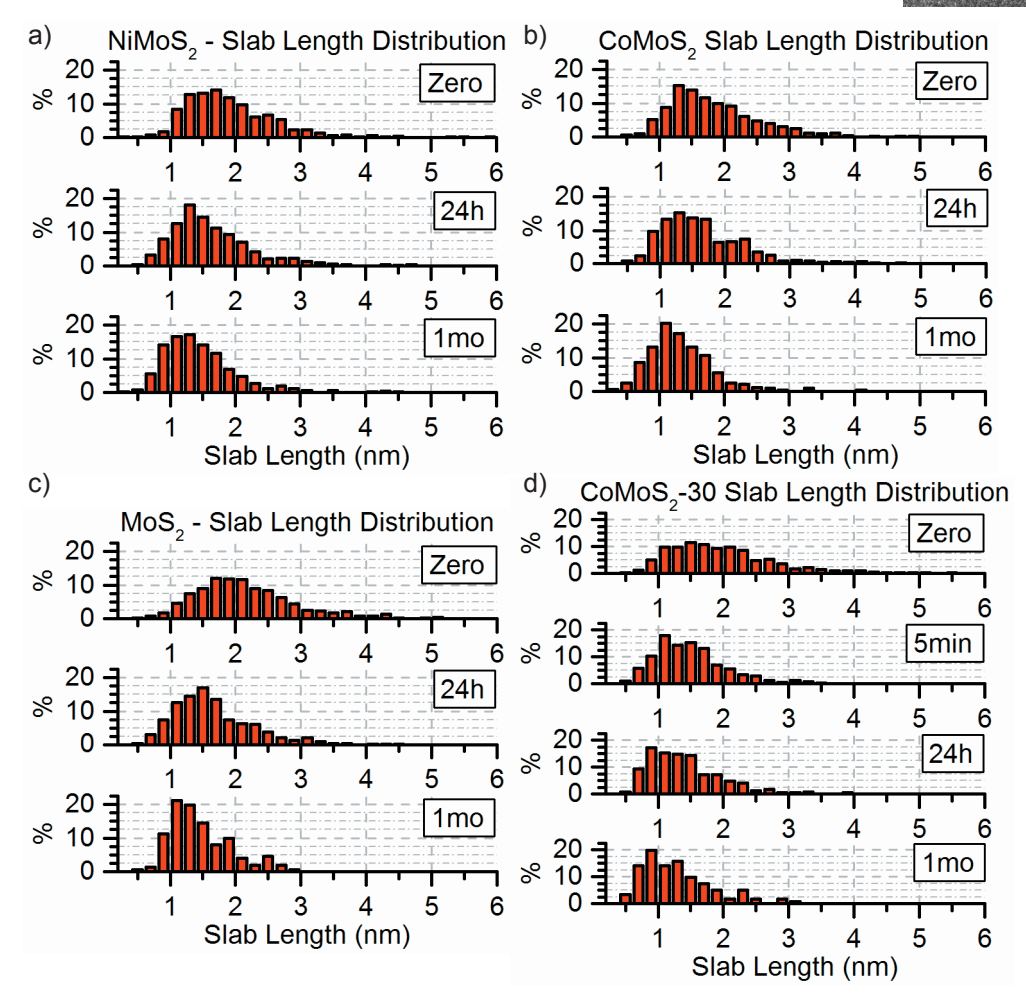


Figure 2.2. Sets of histograms showing the slab length distribution of: (a) NiMoS₂, (b) CoMoS₂, (c) MoS₂, and (d) CoMoS₂-30, as a function of air exposure time.

Table 2.2. Average Slab Length (l) in nm of each sample, including the control data of parts of the sample that had not previously been exposed to the electron beam.

	NiMoS ₂	CoMoS ₂	CoMoS ₂ -30	MoS ₂
Zero	1.91	1.83	1.98	2.16
5 min in air			1.48	
24 h in air	1.65	1.64	1.39	1.66
Control 24 h	1.80	1.76	1.55	1.78
1 month in air	1.45	1.33	1.29	1.46
Control 1 month	-	1.52	1.37	1.76

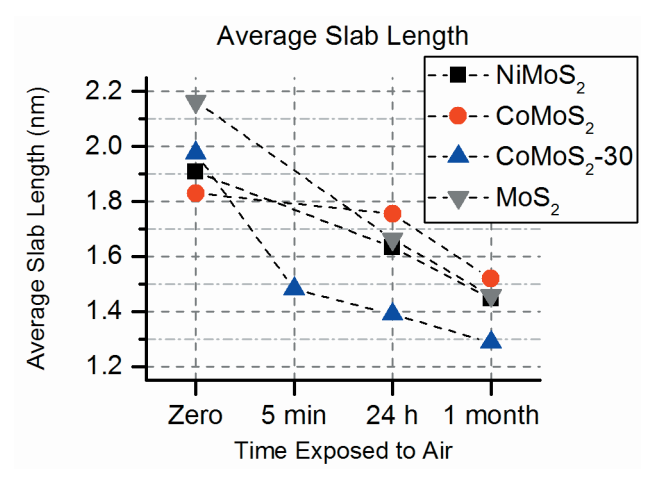


Figure 2.3. Average slab length of all (Ni/Co)MoS, samples as a function of air exposure time.

exposed to the electron beam for the first time. Although $\operatorname{NiMoS}_2 t = 24 \text{ h}$ control data were inadvertently not obtained, the data show a clear trend. Slabs in areas that had not yet been exposed to the electron beam also decreased in length, but at a somewhat lower rate. This indicates that exposure to the electron beam had a minor accelerating contribution to the process of slab deterioration.

2.3.2 X-ray Photoelectron Spectroscopy

To obtain detailed information concerning the composition of the catalyst at the different stages of air exposure during the experiments, we performed X-ray photo- electron spectroscopy. Figure 2.4 shows the acquired XP spectra of the catalyst samples, demonstrating the change in atomic composition as a function of air exposure time. At t = 0, approximately 80% of Mo and Ni and 90% of Co was present as the respective metal sulfides. All sulfur was present as sulfidic sulfur (S²-, S₂²). For CoMoS₂, sulfidation at 30 bar slightly increased the fractions of MoS₂ and Co sulfide compared with sulfidation at 1 bar. Upon brief exposure to air (5 min), no oxidation of Mo or S was apparent in the XP spectra, whereas slight oxidation (approximately 10%) of the Ni/Co promoter atoms could be observed after deconvolution of the XP spectra in the promoted catalysts. After an additional 24 h of exposure to air, approximately 15% of Mo, 6% of S, 39% of Ni, and 24% of Co was oxidized compared with the freshly sulfided catalysts at t = 0. Oxidation of the Mo and S species occurred at approximately the same rates in both the promoted and unpromoted samples. The promoted catalysts were most prone to oxidation as the Ni and Co atoms oxidized first. The oxidation of Co leveled off after 24 h of exposure to air, whereas Ni oxidation was an ongoing process.

After 1 month of exposure to air, all catalysts showed significant oxidation of all elements. Even sulfur, which oxidized more slowly than the other elements, was significantly oxidized after 1 month of exposure to air. The observed sequence of oxidation over time was Ni/Co > Mo > S. The data depicted in Figure 2.4 are listed in Table 2.2.

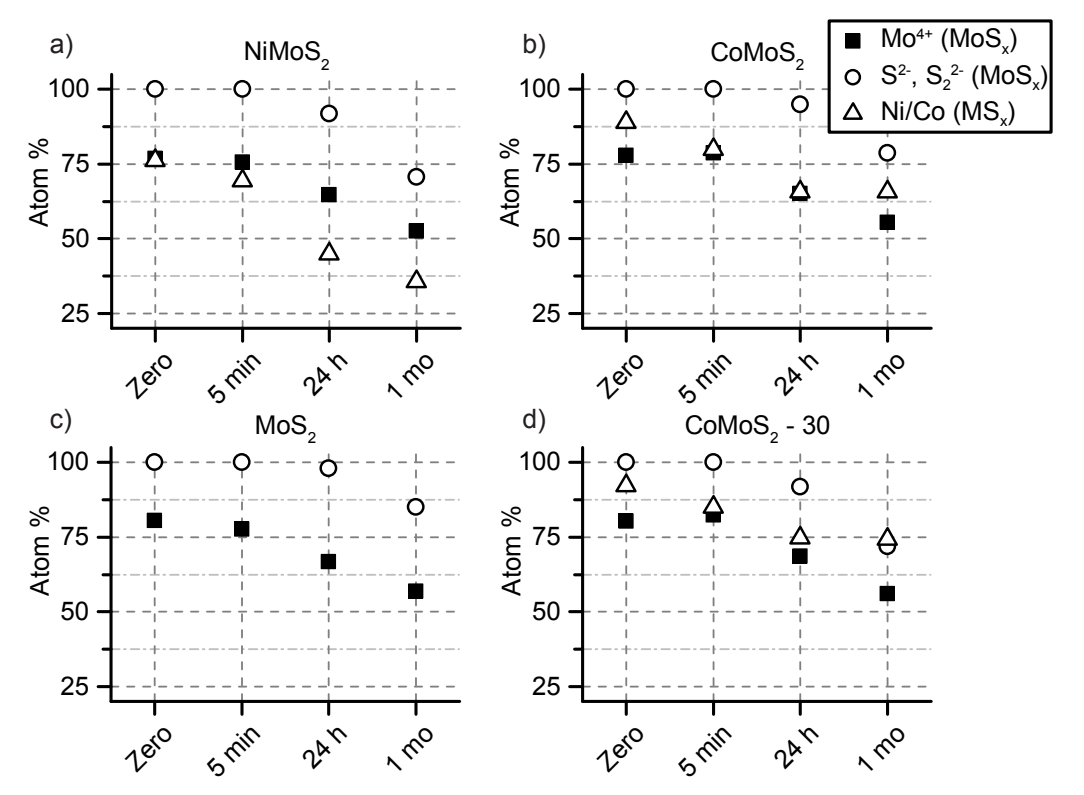


Figure 2.4. Composition (in atom %, as determined by deconvolution of XP spectra) of the samples (a) NiMoS₂,(b) CoMoS₂, (c) MoS₂, and (d) CoMoS₂-30, prior to exposure to air and after 5 min, after 24 h, and after 1 month of exposure to air. The fraction of sulfided species was calculated from the contributions of MoS₂ (Mo⁴⁺), sulfide anions (S²⁻ and S₂²⁻) and sulfided Ni/Co (either as M-MoS₂ or as MS_x).

The Ni 2p, Mo 3d, and S 2p XP spectra of NiMoS $_2$ are plotted in Figure 2.5 and are representative for all catalysts exposed to air. The XP spectra for the other samples are shown in Figures 2.6 - 2.8. Oxidation of the MoS $_2$ -phase was evident from the appearance of a peak at 235.9 eV in Figure 2.5b, which can be ascribed to Mo $^{6+}$, as in MoO $_3$ (3d $_{3/2}$). The formation of NiO was shown by the peak at 856.5 eV appearing in the Ni 2p spectrum (Figure 2.5a) as well as by the appearance of satellite features at ~862 eV (Ni 2p $_{3/2}$) and ~880 eV (Ni 2p $_{1/2}$). In agreement with these observations, a peak at 168.8 eV appeared in the S 2p spectrum (Figure 2.5c), indicative of the formation of sulfates. After 1 month of exposure to air, increased oxidation was observed in all spectra.

Table 2.2. Composition (atom %, as determined by deconvolution of XP spectra) of the samples NiMoS₂, CoMoS₂, MoS₂, and CoMoS₂–30, prior to exposure to air, after 5 minutes, after 24 hours, and after 1 month of exposure to air. The fraction of sulfided species was calculated from the contributions of MoS₂ (Mo⁴⁺), sulfide anions (S²⁻ and S₂²⁻) and sulfided Ni/Co (either as M-MoS₂ or as MS₂) to the respective XP spectra.

NUM-C						
	NiMoS ₂			CoMoS ₂		
	Mo^{4+}	S^{2-}, S_2^{2-}	Ni	Mo ⁴⁺	S^{2-}, S_{2}^{2-}	Co
Zero	76.8	100.0	76.2	77.8	100.0	89.0
5 min	75.6	100.0	69.5	78.6	100.0	79.9
24 h	64.7	91.8	44.9	65.1	95.0	65.6
1 month	52.5	70.6	35.7	55.4	78.7	65.7
	MoS_2			CoMoS ₂ - 30		
	Mo^{4+}	S^{2-} , S_2^{2-}		Mo ⁴⁺	S^{2-} , S_2^{2-}	Co
Zero	80.5	100.0		80.3	100.0	92.3
5 min	77.7	100.0		82.3	100.0	85.0
24 h	66.6	97.9		68.6	91.9	74.8
1 month	56.8	85.0		55.9	71.9	74.3

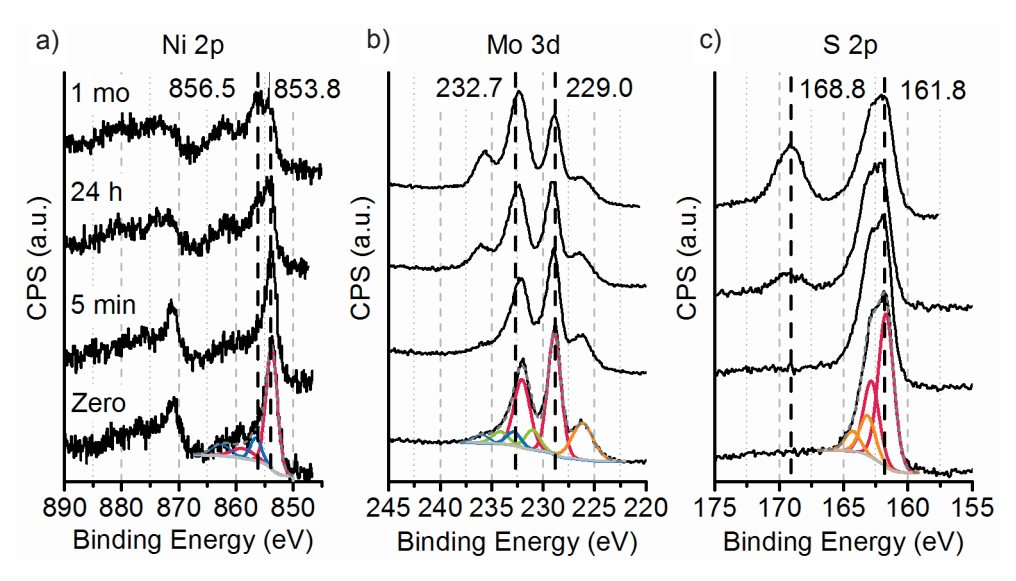


Figure 2.5. XP spectra of NiMoS₂, showing the (a) Ni 2p, (b) Mo 3d, and (c) S 2p signals, prior to exposure to air and after 5 min, 24 h, and 1 month of exposure to air. The binding energies (BE) of sulfided species (lower BE) and oxidized species (higher BE) are indicated by the dotted lines. The deconvolution is also shown. (a) Ni 2p: NiS₂, red; NiO₃, blue (both include satellites). (b) Mo 3d: Mo⁴⁺, red; Mo⁵⁺, green; Mo⁶⁺, blue; for S 2s, orange. (c) S 2p: S²⁻, red; S₂²⁻, orange. In all graphs: background, light gray; fit, gray dashed; data is black.

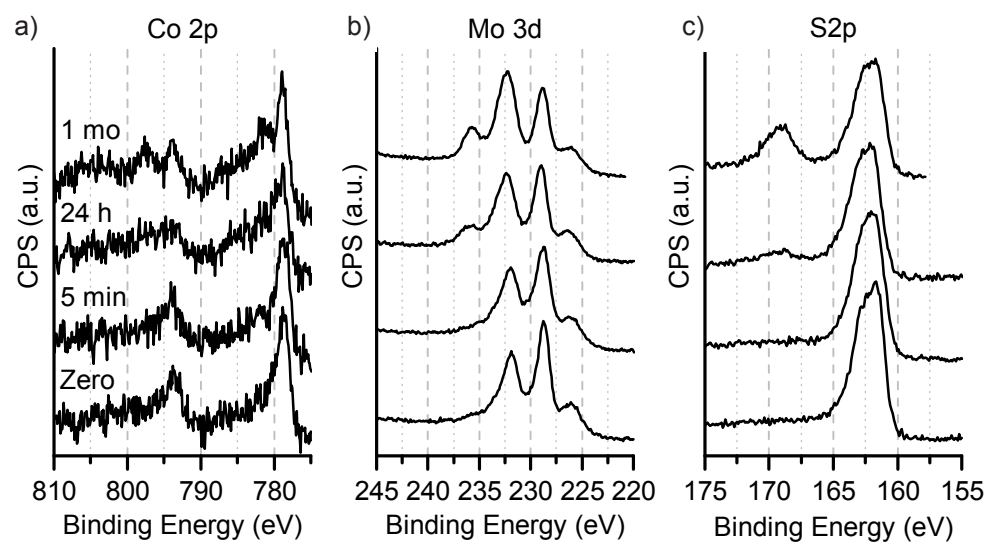


Figure 2.6. XP spectra of CoMoS₂, showing (a) the Co 2p, (b) the Mo 3d, and (c) the S 2p signals, prior to exposure to air, after 5 minutes, 24 h, and 1 month of exposure to air.

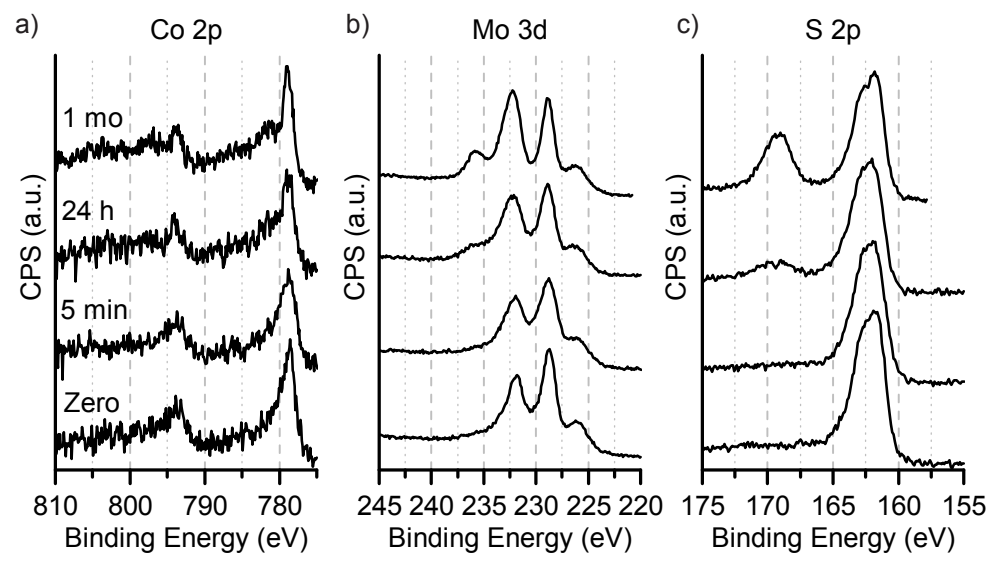


Figure 2.7. XP spectra of CoMoS₂-30, showing (a) the Co 2p, (b) the Mo 3d, and (c) the S 2p signals, prior to exposure to air, after 5 minutes, 24 h, and 1 month of exposure to air.

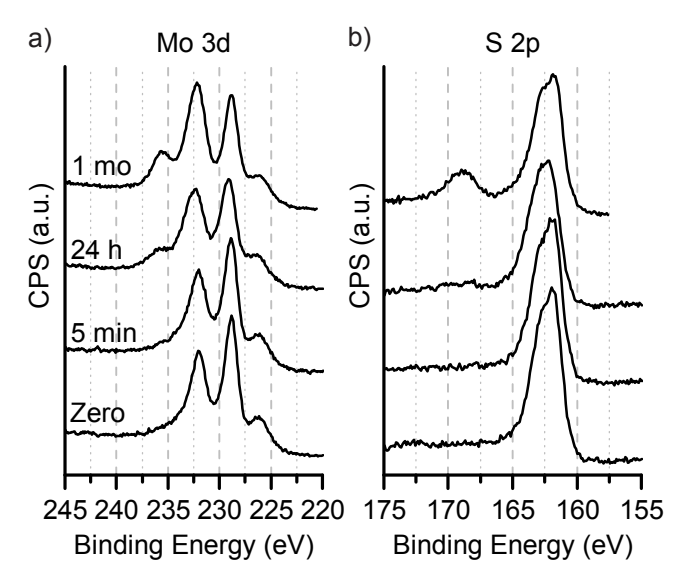


Figure 2.8. XP spectra of MoS₂, showing (a) the Mo 3d, and (b) the S 2p signals, prior to exposure to air, after 5 minutes, 24 h, and 1 month of exposure to air.

2.3.3 Proposed oxidation mechanism.

On the basis of the obtained TEM data alone, it is not easy to go beyond the slablength analysis presented above and draw additional conclusions, e.g., about the atomic structure, location, and orientation of the new species that were formed during exposure to air. Combining the TEM observations with the XP spectra, we can, however, draw further conclusions.

Exposure to air leads to oxidation of the samples, as is indicated by the XP spectra shown in Figures 2.4 and 2.5. The oxidation initiates at the Ni/Co promoter atoms and continues with the oxidation of Mo after prolonged exposure to air. As is visible in the TEM micrographs, the slabs disappear from the sides of the particle toward the center. In various other studies, it has been shown that MoS_2 -catalyzed reactions occur on the edges of the MoS_2 crystals, supported on a variety of materials.[4,24-28] The catalytically active species are the metal atoms located at the edges of the slabs. The oxide species that are formed there (MoO_3 , oxysulfides) have no planar crystal structure;[14,23] hence, the edges of the slabs disappear in the TEM images, enabling us to observe a change in slab length.

The suggestion that oxidation of the slabs starts from the edge is also supported by the XPS data, which show the initial oxidation, during the first 5 min of exposure to air, to occur at the Ni/Co promoter atoms, to form $\text{NiO}_x/\text{CoO}_x$. However, this is not conclusive on its own because it has not been indisputably shown that the promoter atoms in (Ni/Co)MoS₂, supported on γ -Al₂O₃, are located on the edges of the MoS₂ slabs, as was shown in various other studies of (Ni/Co)MoS₂ on different supports (e.g., Au single-crystal surfaces or graphite).[29-32] Also, the initial Ni/Co oxidation XPS signal could, at least partially, originate from the oxidation of Ni/Co atoms that were not incorporated in the (Ni/Co)MoS₂ slabs but were contained in other species on the sample, such as Ni/Co-sulfides.[30] This suggestion is also

supported by the fact that γ -Al₂O₃-supported Co-sulfides oxidize more readily than γ -Al₂O₃-supported MoS₂.[33]

The scale of the horizontal axes in the graphs that show the evolution of the samples as a function of air exposure time is close to logarithmic (Figures 2.3 and 2.4). The approximately linear curves in these plots indicate an exponential decrease in average slab length. On average, during the first 24 h of air exposure, the average slab length of all samples decreased by 20%. After one more month in air, the decrease had continued up to an average decrease of 30%. As the oxidation rate was initially high but then exponentially slowed, the process appeared to be self-limiting. This could indicate that when the edges of the (Ni/Co)MoS₂-slabs were oxidized, the formed oxide species remained at the support around the slab, thereby shielding the inner MoS₂-species from oxidative attacks by incoming oxygen molecules, as was proposed by Yoshimura et al. in 1991.[33] As the basal planes of the slabs are known to be inactive, [34,35] the oxide ring would be formed only at the edges. When this oxide ring around the slab grew thicker, further oxidation of the remaining slab occurred at a progressively lower rate. This mechanism also explains the slightly accelerating effect of the electron beam on the oxidation process, given in Table 2.2.

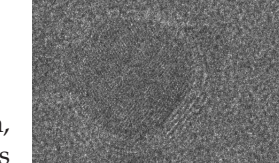
The accelerating effect could be due to the fact that the beam might be able to (slowly) partly disintegrate the protective ring, allowing further oxidation to occur on the slabs that have been imaged multiple times. To prove this hypothesis, additional measurements would be required, however (e.g., using scanning transmission electron microscopy or scanning tunneling microscopy on flat model systems to localize and visualize the formed oxide species). This hypothesis also explains why the method of oxygen titration/chemisorption does not give quantitative results for the number of active sites:[36] the sites are being changed by the adsorbed oxygen.

2.4 Conclusion

Ni/Co-promoted and unpromoted MoS₂ catalyst particles, dispersed on a γ-Al₂O₃ substrate, are not stable in ambient air. TEM imaging reveals that on average the length of the (Ni/Co)MoS₂-slabs decreases as a function of air exposure time. Even 5 min of exposure to ambient air already significantly decreases the average slab length. XPS shows that the samples are being oxidized. Oxidation of the catalyst slabs occurs from the edges toward the center of the slab, after which the formed oxide species probably remain around the slab. These remaining oxide species might form a ring-like barrier structure around the inner MoS₂-species, shielding these inner species from oxidation and explaining the exponential decay of the process.

References

- [1] Environmental Protection Agency. Control of Air Pollution From Motor Vehicles: Tier 3 Motor Vehicle Emission and Fuel Standards; Final Rule; **2014**, Vol. 79.
- [2] Eijsbouts, S.; Heinerman, J.; Elzerman, H. MoS₂ Structures in High-Activity Hydrotreating Catalysts. *Appl. Catal. A* **1993**, 105 (1), 53–68 DOI: 10.1016/0926-860X(93)85133-A.
- [3] Füchtbauer, H. G.; Kibsgaard, J.; Lauritsen, J. V.; Tuxen, A. K.; Lægsgaard, E.; Li, Z.; Clausen, B. S.; Topsøe, H.; Besenbacher, F. Morphology and Atomic-Scale Structure of MoS₂ Nanoclusters Synthesized with Different Sulfiding Agents. *Top. Catal.* **2013**, *57* (1-4), 207–214 DOI: 10.1007/s11244-013-0176-1.
- [4] Lauritsen, J. V.; Nyberg, M.; Nørskov, J. K.; Clausen, B. S.; Topsøe, H.; Lægsgaard, E.; Besenbacher, F. Hydrodesulfurization Reaction Pathways on MoS₂ Nanoclusters Revealed by Scanning Tunneling Microscopy. *J. Catal.* **2004**, 224 (1), 94–106 DOI: 10.1016/j.jcat.2004.02.009.
- [5] McGovern, I. T.; Dietz, E.; Rotermund, H. H.; Bradshaw, A. M.; Braun, W.; Radlik, W.; McGilp, J. F. Soft X-Ray Photoemission Spectroscopy of Metal-Molybdenum Bisulphide Interfaces. *Surf. Sci.* **1985**, *152-153*, 1203–1212 DOI: 10.1016/0039-6028(85)90540-0.
- [6] Wilcoxon, J.; Samara, G. Strong Quantum-Size Effects in a Layered Semiconductor: MoS₂ Nanoclusters. *Phys. Rev. B* **1995**, *51* (11), 7299–7302 DOI: 10.1103/PhysRevB.51.7299.
- [7] Mak, K. F.; Lee, C.; Hone, J.; Shan, J.; Heinz, T. F. Atomically Thin MoS₂: A New Direct-Gap Semiconductor. *Phys. Rev. Lett.* **2010**, *105* (13), 136805 DOI: 10.1103/PhysRevLett.105.136805.
- [8] Yazyev, O. V.; Kis, A. MoS₂ And Semiconductors in the Flatland. *Mater. Today* **2015**, *18* (1), 20–30 DOI: 10.1016/j.mattod.2014.07.005.
- [9] Li, Q.; Zhang, N.; Yang, Y.; Wang, G.; Ng, D. H. L. High Efficiency Photocatalysis for Pollutant Degradation with MoS_2/C_3N_4 Heterostructures. *Langmuir* **2014**, 30 (29), 8965–8972 DOI: 10.1021/la502033t.
- [10] Kang, Y.; Gong, Y.; Hu, Z.; Li, Z.; Qiu, Z.; Zhu, X.; Ajayan, P. M.; Fang, Z. Plasmonic Hot Electron Enhanced MoS₂ Photocatalysis in Hydrogen Evolution. *Nanoscale* **2015**, *7* (10), 4482–4488 DOI: 10.1039/c4nr07303g.
- [11] Spalvins, T. A Review of Recent Advances in Solid Film Lubrication. *J. Vac. Sci. Technol. A* **1987**, *5* (2), 212 DOI: 10.1116/1.574106.
- [12] Hilton, M. R.; Bauer, R.; Didziulis, S. V.; Dugger, M. T.; Keem, J. M.; Scholhamer, J. Structural and Tribological Studies of MoS₂ Solid Lubricant Films Having Tailored Metal-Multilayer Nanostructures. *Surf. Coat. Technol.* **1992**, *53* (1), 13–23 DOI: 10.1016/0257-8972(92)90099-V.
- [13] Chhowalla, M.; Amaratunga, G. A. J. Thin Films of Fullerene-Like MoS₂ Nanoparticles with Ultra-Low Friction and Wear. *Nature* **2000**, 407 (6801), 164–167 DOI: 10.1038/35025020.
- [14] Kooyman, P. J.; van Veen, J. A. R. The Detrimental Effect of Exposure to Air on Supported MoS₂. *Catal. Today* **2008**, *130* (1), 135–138 DOI: 10.1016/j. cattod.2007.07.019.



- [15] Hensen, E. J. M.; de Beer, V. H. J.; van Veen, J. A. R.; van Santen, R. A. A Refinement on the Notion of Type I and II (Co)MoS Phases in Hydrotreating Catalysts. *Catal. Lett.* **2002**, *84* (1/2), 59–67 DOI: 10.1023/A:1021024617582.
- [16] Egorova, M.; Prins, R. The Role of Ni and Co Promoters in the Simultaneous HDS of Dibenzothiophene and HDN of Amines Over Mo/ γ -Al₂O₃ Catalysts. *J. Catal.* **2006**, 241 (1), 162–172 DOI: 10.1016/j.jcat.2006.04.011.
- [17] Byskov, L. S.; Nørskov, J. K.; Clausen, B. S.; Topsøe, H. DFT Calculations of Unpromoted and Promoted MoS₂-Based Hydrodesulfurization Catalysts. *J. Catal.* **1999**, *187* (1), 109–122 DOI: 10.1006/jcat.1999.2598.
- [18] Zandbergen, H.; Kooyman, P. J.; van Langeveld, A. D. Transfer Systems for Insertion of Specimens Into Electron Microscopes Under Controlled Atmospheres; *Electron Microscopy 1998: Proceedings of the 14th International Congress on Electron Microscopy*, Cancun, Mexico, August 31 September 4, **1998**; Vol. II, 491–492.
- [19] van Haandel, L.; Kooyman, P. J.; van Veen, J. A. R.; Weber, T.; Hensen, E. J. M.; Bremmer, G. M. Structure–Activity Correlations in Hydrodesulfurization Reactions Over Ni-Promoted $Mo_xW(_{1-x})S_2/Al_2O_3$ Catalysts. *ACS Catal.* **2015**, 7276–7287 DOI: 10.1021/acscatal.5b01806.
- [20] Weber, T.; Muijsers, J. C.; Van Wolput, J.; Verhagen, C. P. J.; Niemantsverdriet, J. W. Basic Reaction Steps in the Sulfidation of Crystalline MoO_3 To MoS_2 , As Studied by X-Ray Photoelectron and Infrared Emission Spectroscopy. *J. Phys. Chem.* **1996**, 100 (33), 14144–14150 DOI: 10.1021/jp961204y.
- [21] Alstrup, I.; Chorkendorff, I.; Candia, R.; Clausen, B. S.; Topsøe, H. A Combined X-Ray Photoelectron and Mössbauer Emission Spectroscopy Study of the State of Cobalt in Sulfided, Supported, and Unsupported Co-Mo Catalysts. *J. Catal.* **1982**, *77* (2), 397–409 DOI: 10.1016/0021-9517(82)90181-6.
- [22] Gandubert, A. D.; Legens, C.; Guillaume, D.; Rebours, S.; Payen, E. X-Ray Photoelectron Spectroscopy Surface Quantification of Sulfided CoMoP Catalysts Relation Between Activity and Promoted Sites Part I: Influence of the Co/Mo Ratio. *Oil Gas Sci. Technol.* **2007**, *62* (1), 79–89 DOI: 10.2516/ogst:2007007.
- [23] Hansen, L. P.; Johnson, E.; Ramasse, Q. M.; Kisielowski, C. F.; Brorson, M.; Helveg, S. Electron Microscopy Studies of Structure and Dynamics in MoS_2 -Based Hydrodesulfurization Catalysts. *Microsc. Microanal.* **2014**, 20 (S3), 1566–1567 DOI: 10.1017/S1431927614009568.
- [24] Jaramillo, T. F.; Jørgensen, K. P.; Bonde, J. L.; Nielsen, J. H.; Horch, S.; Chorkendorff, I. Identification of Active Edge Sites for Electrochemical H₂ Evolution From MoS₂ Nanocatalysts. *Science* **2007**, *317* (5834), 100–102 DOI: 10.1126/science.1141483.
- [25] Lauritsen, J. V.; Nyberg, M.; Vang, R. T.; Bollinger, M. V.; Clausen, B. S.; Topsøe, H.; Jacobsen, K. W.; Lægsgaard, E.; Nørskov, J. K.; Besenbacher, F. Chemistry of One-Dimensional Metallic Edge States in MoS₂ Nanoclusters. *Nanotechnology* **2003**, *14* (3), 385–389 DOI: 10.1088/0957-4484/14/3/306.
- [26] Hensen, E. J. M.; Kooyman, P. J.; van der Meer, Y.; van der Kraan, A.; de Beer, V. H. J.; van Veen, J. A. R.; van Santen, R. A. The Relation Between Morphology and Hydrotreating Activity for Supported MoS₂ Particles. *J. Catal.* **2001**, 199 (2), 224–235

- DOI: 10.1006/jcat.2000.3158.
- [27] Temel, B.; Tuxen, A. K.; Kibsgaard, J.; Topsøe, N.-Y.; Hinnemann, B.; Knudsen, K. G.; Topsøe, H.; Lauritsen, J. V. Atomic-Scale Insight Into the Origin of Pyridine Inhibition of MoS₂-Based Hydrotreating Catalysts. *J. Catal.* **2010**, 271 (2), 280–289 DOI: 10.1016/j.jcat.2010.02.007.
- [28] Tuxen, A. K.; Kibsgaard, J.; Gøbel, H.; Lægsgaard, E.; Topsøe, H.; Lauritsen, J. V.; Besenbacher, F. Size Threshold in the Dibenzothiophene Adsorption on MoS₂ Nanoclusters. *ACS Nano* **2010**, *4* (8), 4677–4682 DOI: 10.1021/nn1011013.
- [29] Lauritsen, J. V. Atomic-Scale Structure of Co-Mo-S Nanoclusters in Hydrotreating Catalysts. *J. Catal.* **2001**, 197 (1), 1–5 DOI: 10.1006/jcat.2000.3088.
- [30] Lauritsen, J. V.; Kibsgaard, J.; Olesen, G. H.; Moses, P. G.; Hinnemann, B.; Helveg, S.; Nørskov, J. K.; Clausen, B. S.; Topsøe, H.; Lægsgaard, E.; *et al.* Location and Coordination of Promoter Atoms in Co- and Ni-Promoted MoS₂-Based Hydrotreating Catalysts. *J. Catal.* **2007**, 249 (2), 220–233 DOI: 10.1016/j.jcat.2007.04.013.
- [31] Kibsgaard, J.; Tuxen, A. K.; Knudsen, K. G.; Brorson, M.; Topsøe, H.; Lægsgaard, E.; Lauritsen, J. V.; Besenbacher, F. Comparative Atomic-Scale Analysis of Promotional Effects by Late 3d-Transition Metals in MoS₂ Hydrotreating Catalysts. *J. Catal.* **2010**, 272 (2), 195–203 DOI: 10.1016/j.jcat.2010.03.018.
- [32] Zhu, Y.; Ramasse, Q. M.; Brorson, M.; Moses, P. G.; Hansen, L. P.; Kisielowski, C. F.; Helveg, S. Visualizing the Stoichiometry of Industrial-Style Co-Mo-S Catalysts with Single-Atom Sensitivity. *Angew. Chem. Int. Ed.* **2014**, *53* (40), 10723–10727 DOI: 10.1002/anie.201405690.
- [33] Yoshimura, Y.; Matsubayashi, N.; Yokokawa, H.; Sato, T.; Shimada, H.; Nishijima, A. Temperature-Programmed Oxidation of Sulfided Cobalt-Molybdate/Alumina Catalysts. *Ind. Eng. Chem. Res.* **1991**, 30 (6), 1092–1099 DOI: 10.1021/ie00054a004.
- [34] Salmeron, M.; Somorjai, G. A.; Wold, A.; Chianelli, R.; Liang, K. S. The Adsorption and Binding of Thiophene, Butene and H₂S on the Basal Plane of MoS₂ Single Crystals. *Chem. Phys. Lett.* **1982**, *90* (2), 105–107 DOI: 10.1016/0009-2614(82)83620-8.
- [35] Kushmerick, J. G.; Weiss, P. S. Mobile Promoters on Anisotropic Catalysts: Nickel on MoS₂; *J. Phys. Chem. B*, **1998**; 102, 10094–10097 DOI: 10.1021/jp982752.
- [36] Zmierczak, W.; Muralidhar, G.; Massoth, F. E. Studies on Molybdena Catalysts XI. Oxygen Chemisorption on Sulfided Catalysts. *J. Catal.* **1982**, 77 (2), 432–438 DOI: 10.1016/0021-9517(82)90184-1.







CHAPTER 3

The effect of oxidation and resulfidation on (Ni/Co) MoS₂ hydrodesulfurization catalysts

The effect of a sequential oxidation and resulfidation treatment on $(Ni/Co)MoS_2$ catalyst nanoparticles, supported on γ -Al $_2O_3$, was investigated using high resolution (HR)TEM, XPS, and thiophene HDS catalytic performance measurements. Analysis of the HRTEM images revealed that, after the initial sulfidation and oxidation, the resulfidation treatment had the effect that the catalyst slabs were growing back to their original slab length. Also, there are relatively less small slabs present. The chemical composition of the samples, as determined by XPS, also slightly changed, as the concentration of oxides increased, especially for the Ni promoter atoms. Comparing the catalytic HDS activity of the samples before and after the oxidation-resulfidation treatment showed that the catalysts were, overall, more than 20% more active after resulfidation. Since the number of smaller slabs has decreased significantly after resulfidation, it is suggested that this increase in activity might be caused by a size effect of the catalyst.

3.1 Introduction

Environmental legislations steer oil refineries towards producing transportation fuels that contain ever less sulfur contaminants.[1] Sulfur is typically removed using the catalytic hydro-desulfurization (HDS) reaction, which exploits (Ni/Co) MoS $_2$ catalysts dispersed on $\gamma\text{-Al}_2O_3$ as support material.[2,3] MoS $_2$ catalysts consist of a single layer of molybdenum atoms sandwiched between two layers of sulfur, forming two-dimensional slab-like particles with a typical size of 2 to 3 nm.[4,5] Typical $\gamma\text{-Al}_2O_3$ -supported MoS $_2$ catalysts contain both single catalyst slabs and stacks of multiple slabs. The catalyst performance in terms of activity and selectivity can be influenced by adding metal promoter atoms such as nickel or cobalt, yielding (Ni/Co)MoS $_2$ slabs.[2,3,6] As this catalytic system is intensively used, there is a great research effort in industry and academia to improve the catalyst.

Previous research indicated that experimentalists should be careful during preparation and handling of their MoS₂ catalyst samples, to prevent exposing the samples to air as this will change the particle size of the sulfide entities.[7] Further investigations showed that oxidic species form on the edges of the (Ni/Co)MoS₂ catalyst slabs upon exposure to air.[8] It was suggested that these oxidic species would remain around a core of (Ni/Co)MoS₂ that still subsists, forming a ring-like barrier and thereby impeding further oxidation.

The question remained what the effect of a high-temperature resulfidation treatment would be on these oxidized catalysts, in terms of catalyst activity, size, and dispersion. Since the initial preparation of the catalyst involves the sulfidation of oxidic precursor species that finally form the (Ni/Co)MoS₂ slabs,[9] the newly formed oxidic species could probably be transformed back into sulfides. Two possible results of this approach could be that these sulfides would then either aggregate into new (Ni/Co)MoS₂ crystallites, or combine with the still-existing (Ni/Co)MoS₂ slabs, causing these slabs to grow back and resemble the situation as it was before oxidation.

To investigate this question, we prepared a series of NiMoS₂, CoMoS₂, and MoS₂ samples, supported on γ -Al₂O₃. After initial sulfidation, we investigated the catalyst using high resolution transmission electron microscopy (HRTEM), X-ray photoelectron spectroscopy (XPS), and thiophene HDS catalytic performance experiments, then exposed the samples to a flow of artificial air (O₂/N₂, 20/80) for 24 h. Following this oxidation step, we subjected the samples to a second sulfidation treatment, identical to the initial sulfidation step. The samples were then investigated again using the aforementioned techniques. A second NiMoS₂ sample was also prepared using two consecutive sulfidation treatments, without an interim oxidation step, to compare the HDS activity data.

3.2 Experimental

3.2.1 Preparation of catalysts

The catalyst samples were prepared by incipient-wetness co-impregnation of Ketjen CK-300 γ -Al₂O₃ extrudates (S_{BET} = 250 m²/g, V_{pore} = 0.66 mL/g), which were crushed and sieved to a 125-250 μ m fraction prior to impregnation. Different solutions containing nickel(II) nitrate (Ni(NO₃)₂ 6H₂O, Merck), cobalt(II) nitrate (Co(NO₃)₂ 6H₂O,

Merck), ammonium heptamolybdate ((NH₄) $_6$ Mo $_7$ O $_{24}$ 4H $_2$ O, Merck), and nitrilotriacetic acid (NTA) ((C $_2$ H $_3$ O $_2$) $_3$ N, Merck) were prepared to obtain catalysts with 8 wt% Mo, and 1.5 wt% Ni or Co for the promoted

catalysts. The molar ratio of NTA:Mo was 1.2:1. All catalyst precursors were dried at room temperature for 1 h, dried in static air at 100 °C overnight and finally calcined at 450 °C (heating rate 6 °C/min) in flowing air for 4 h. The catalyst precursors were sulfided at 350 °C (heating rate 6 °C/min) for 2 h in $\rm H_2/H_2S$ 9:1 (Scott), in a flow of 60 mL/min STP at a total pressure of 1 bar.

To obtain 'oxidized' samples, a portion of the freshly sulfided sample was placed in a glass tube, and a flow of O_2/N_2 (20/80, 150 mL/min) was set over the sample for 24 h. After oxidation, the sample was re-sulfided via the same recipe used for the initial sulfidation. After preparation, and in between each experimental step, the samples were collected, placed in a glovebox filled with N_2 (concentration of $H_2O < 5$ ppm, $O_2 < 1$ ppm), and sealed in glass vials.

3.2.2 TEM and XPS characterization of catalysts

TEM studies were carried out using a monochromated FEI Tecnai F20ST/STEM electron microscope, operated at an accelerating voltage of 200 keV, in bright field TEM mode. Images were recorded using a Gatan Ultrascan CCD camera (4k x 4k).

The vials containing the samples were opened in an Ar-filled glovebox, after which the samples were crushed in *n*-hexane (Sigma-Aldrich, anhydrous, 95%) using a mortar and pestle, creating a suspension. A few drops of the suspension were placed on a Quantifoil microgrid carbon film-covered mixed mesh Au TEM grid. After evaporation of the solvent at room temperature, the grid was placed in a protective atmosphere transfer TEM specimen holder.[10] The sample compartment of the holder was then closed and sealed by a Viton O-ring, and the holder was removed from the glovebox and brought to the TEM for imaging. Once inserted in the TEM airlock, one three-minute pumping cycle was started while the holder was still closed, and the sample compartment of the holder was opened at the beginning of a second three-minute pumping cycle.

Samples were imaged after the initial sulfidation and after the oxidation-resulfidation treatment. Since the behavior of the samples upon mere oxidation was already thoroughly documented before,[7,8] we did not characterize the oxidized samples. The resulting images were analyzed using ImageJ software. After identifying the slabs, the length of each slab was measured by hand using standard drawing tools in the software. Per sample, around 500 individual slabs were measured. The mean slab length was obtained from the least-squares fit of a log-normal distribution to the slab length histogram, as is a common approach when modeling particle size distributions.[11-14] The average stacking degree (*N*) was calculated according to eqn. (1):

 $N = \frac{\sum_{i} n_{i} N_{i}}{\sum_{i} n_{i}} \tag{1}$

where N_i is the stacking number of a stack of MoS_2 (i.e., the number of MoS_2 platelets in the stack) and n_i is the amount of individual MoS_2 platelets counted for a given stacking number N_i .

The same samples were analyzed using a Kratos AXIS Ultra XP spectrometer, equipped with a monochromatic Al ($K\alpha$ = 1486.6 eV) X-ray source and a delay-

line detector (DLD). To prevent contact with air, samples were transferred from the glovebox to the XPS in a closed, homemade transfer holder under N_2 atmosphere. Survey scans were recorded at constant pass energy of 160 eV and region scans at 40 eV. The background pressure was 2 × 10-9 mbar.

XP spectra were fitted with CasaXPS (version 2.3.14) by a non-linear least-squares fitting algorithm using mixed Gaussian-Lorentzian (35/65) curves. Shirley background subtraction was applied and the energy was calibrated using the Al 2p peak at 74.6 eV as a reference. The Mo 3d spectrum was fitted with Mo⁴⁺ (MoS₂), Mo⁵⁺ (MoS_xO_y) and Mo⁶⁺ (MoO₃) contributions. The Ni 2p and Co 2p spectra were fitted with a sulfidic M²⁺ contribution and an oxidic M²⁺ contribution (NiO, CoO). The sulfidic contribution was assigned to Ni or Co sulfides, either dispersed on the edges of MoS₂ particles or present as bulk metal sulfides (Ni₃S₂, Co₉S₈). Lastly, the S2-and bridged S₂²⁻ anions, as well as sulfate (SO₄²⁻), were taken into account for fitting the S 2p spectra. Binding energies of these components are listed in Table 3.1 and agree well with previously reported studies.[15-17]

Table 3.1. XPS Binding energies of the various species present in (Co/Ni)MoS₂, as determined by the fitting procedure described in the text.

	Mo ⁴⁺ (MoS ₂)	Mo^{5+} (MoS_xO_y)	Mo ⁶⁺ (MoO ₃)	S ²⁻ (MS _x)	S_2^{2-} (MS _x)
BE (eV) ^a	229.0	231.0	232.6	161.7	163.3
$\Delta \text{BE (eV)}^b$	3.15	3.15	3.15	1.15	1.15
	S ⁶⁺ (SO ₄ ²⁻)	Co^{2+} $(CoS_x)^c$	Co ²⁺ (CoO) ^c	Ni^{2+} $(NiS_x)^c$	Ni ²⁺ (NiO) ^c
BE (eV) ^a	168.8	778.7	778.7	853.9	856.5
$\Delta \text{BE (eV)}^b$	1.15	-	-	-	-

 $[^]a$ Binding energy of the $3d_{5/2}$ or $2p_{3/2}$ peak. Uncertainty ± 0.2 eV.

3.2.3 Catalytic activity

Atmospheric gas-phase thiophene HDS experiments were performed under differential conditions in a single-pass stainless steel flow reactor with an internal diameter of 4 mm. An amount of precisely weighted catalyst particles (approximately 25 mg for (Ni/Co)MoS₂, approximately 50 mg for MoS₂), diluted with 200 mg of SiC (250 μ m), was sulfided in 60 mL/min H₂/H₂S(10%) at 350 °C for 2 h (6 °C/min ramp). Then, the feed was switched to 4% (v/v) thiophene (Sigma-Aldrich) diluted in H₂ at a flow rate of 100 mL/min (STP). Activity was measured by gas chromatography coupled with flame ionization detection (GC-FID). The reaction rate (r_{Thio}) normalized per mole of Mo was calculated according to eqn. (2):

$$r_{\text{Thio}} = \left(\frac{F_{\text{Thio}}}{m_{\text{cat}} w_{\text{Mo}}}\right) X \tag{2}$$

where $F_{\rm Thio}$ is the molar flow of thiophene (mol_{\rm Thio}~h^{-1}), $m_{\rm cat}$ the catalyst mass (g),

 $^{^{}b}\Delta BE(3d) = BE(3d_{3/2}) - BE(3d_{5/2}); \Delta BE(2p) = BE(2p_{1/2}) - BE(2p_{3/2}).$

 $^{^{\}circ}$ Only the $2p_{3/2}$ peak was fitted for Co and Ni.

 $w_{\rm Mo}$ the fraction of molybdenum (mol_{Mo} gcat⁻¹), and X the conversion. Initial conversion was high while steady-state activity was reached after approximately 13 h. The regular method to determine steady-state activity is by calculating the average activity of at least 4~5 h of steady-state data points. As some samples continued to show minor deactivation, even after 20 h of activity tests, the activity data was fitted with a first-order exponential decay function and the horizontal asymptote was defined as the eventual steady-state activity of the

3.3 Results and discussion

catalyst.

3.3.1 Imaging and slab length analysis

To determine the effect of the oxidation-resulfidation treatment on the slab size and dispersion of the different (Ni/Co)MoS₂ samples, a series of TEM characterizations was performed after the initial sulfidation treatment (the 'Zero' data) as well as after the resulfidation treatment (the 'Resulf' data). The length of the slabs was measured, and the resulting slab length distribution histograms are shown in Figure 3.1. It is visible that for NiMoS₂, the slab length distribution has shifted slightly towards higher slab lengths, indicating that the slabs have grown longer after the second sulfidation treatment. This effect is also visible for MoS₂, though less pronounced. The CoMoS₂ sample does not show this increase of slab length, but instead shows that the slab length distribution of both the freshly sulfided and the resulfided samples are almost identical.

It should be considered that the intermediate oxidation step does have a significant effect on the slab length distribution, as previous experiments showed that 24 h of oxidation in air will shift the slab length distributions towards smaller slab lengths, while smaller slabs are disappearing completely.[8]

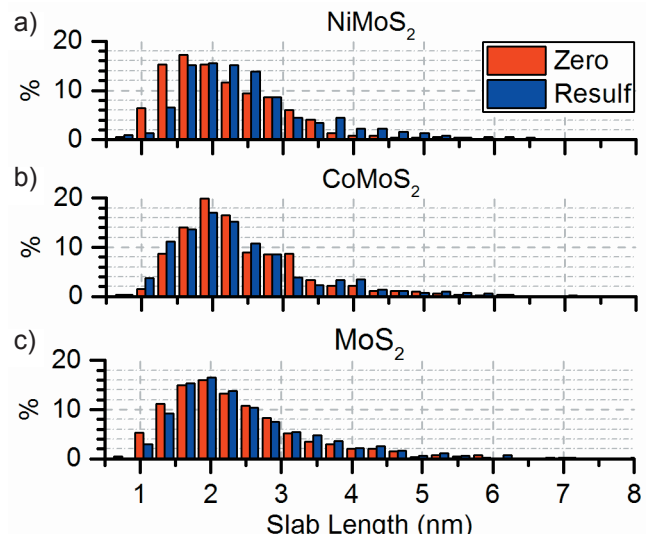


Figure 3.1. Slab length distributions of (a) $NiMoS_2$, (b) $CoMoS_2$, and (c) MoS_2 . Distributions of both the freshly sulfided samples (Zero, red bars) as well as the oxidized and resulfided samples (Resulf, blue bars) are shown.

Since it is shown here that the slab length distribution of the resulfided sample resembles the starting situation reasonably well, we can conclude that the resulfidation treatment after oxidation not only causes the slabs to only increase in size again, but even allows the slabs to grow back to their original length or beyond.

To quantitatively compare the samples, the histograms were fitted with a lognormal distribution and the geometric mean slab length (x) and geometric standard deviation (σ) of each sample was calculated. In order to compare the stacking of the catalyst slabs, the average stacking numbers were calculated, showing the number of slabs per stack on average. Fits of the histograms are shown in Figure 3.2, the data are shown in Table 3.2.

Table 3.2. Geometric mean slab length values (x_c), geometric standard deviation (σ), and average stacking number of the samples.

		x_c (nm)	σ	Stacking
$NiMoS_2$	Zero	1.99 ± 0.03	0.39 ± 0.02	1.4
	Resulf	2.21 ± 0.03	0.31 ± 0.01	1.5
CoMoS ₂	Zero	2.11 ± 0.02	0.37 ± 0.01	1.5
	Resulf	2.15 ± 0.03	0.34 ± 0.01	1.5
MoS_2	Zero	2.12 ± 0.03	0.34 ± 0.01	1.4
	Resulf	2.16 ± 0.04	0.31 ± 0.02	1.5

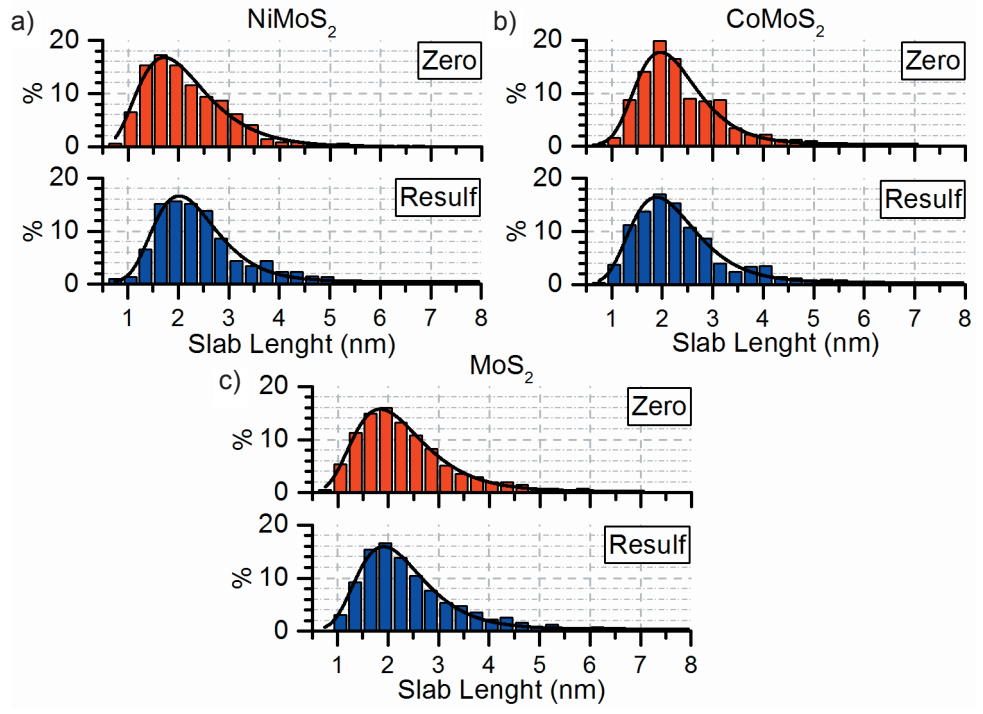


Figure 3.2. Slab length distribution histograms of a) NiMoS₂, b) CoMoS₂, and c) MoS₂. The histograms are fitted with a least squares fit of a log-normal distribution.

The mean slab length values show the same trend as was found in the histogram data given in Figure 3.1. The NiMoS₂ sample shows a substantial increase in mean slab length of approximately 30%. For both MoS₂ and CoMoS₂, the mean slab length does not differ significantly from the freshly sulfided sample. The geometric standard deviation values are similar for all samples,

MoS₂ and CoMoS₂, the mean slab length does not differ significantly from the freshly sulfided sample. The geometric standard deviation values are similar for all samples, and show that the slab length distribution of all resulfided samples have condensed into more narrowed histograms. As for the average stacking, it remains practically the same for all samples between the different sulfidation treatments.

3.3.2 Chemical state of the catalysts

The catalysts were analyzed using XPS directly after the initial sulfidation, as well as after the oxidation-resulfidation treatment. The resulting Ni 2p, Mo 3d, and S 2p spectra of the NiMoS₂ sample, including the deconvolution, are shown in Figure 3.3. The spectra of CoMoS₂ and MoS₂ are shown in the Figures 3.4 and 3.5. The chemical composition of each sample was determined from the deconvolution of the spectra, giving the fractions of species that are in sulfidic state, as shown in Figure 3.6. The numeric data of Figure 3.6 are shown in Table 3.3.

From Figure 3.6 it is visible that after the initial sulfidation of the samples, approximately 83% of Ni, 94% of Co, and 86% of Mo was present as sulfides, while the remainder of these species remained oxidic. The sulfur signal consisted solely of sulfidic species (S^2 -, S_2^2); no oxides were observed. The effect of the oxidation-resulfidation treatment had a small effect on the Mo spectra of all three samples, and on the Co spectra: the sulfide/oxide ratio of these components only slightly changed, between 0.4% and 2.1%.

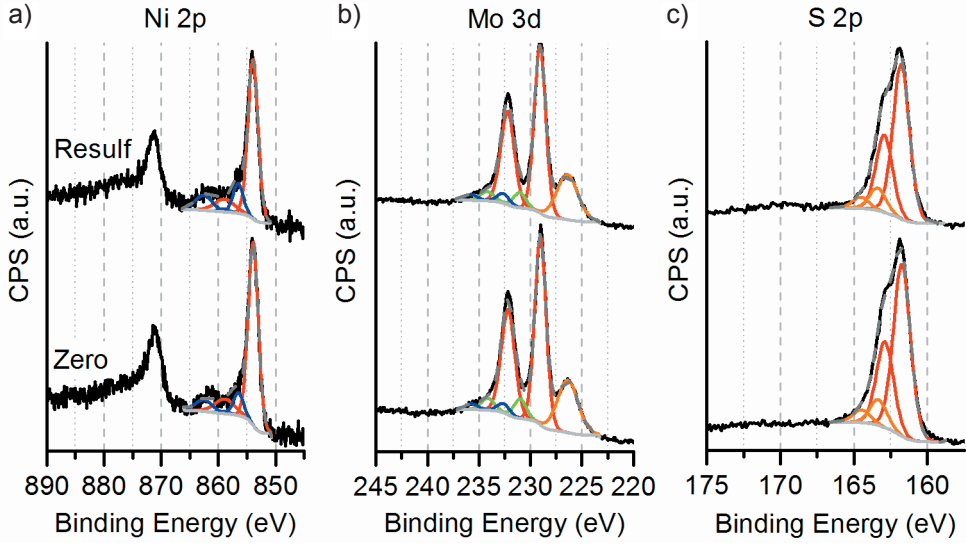


Figure 3.3. XP spectra of NiMoS2, showing the (a) Ni 2p, (b) Mo 3d, and (c) S 2p signals after initial sulfidation (Zero) and after the oxidation-resulfidation treatment (Resulf). The deconvolution consists of the following components:(a) Ni 2p: NiS_x, red; NiO_x, blue (both include satellites). (b) Mo 3d: Mo⁴⁺, red; Mo⁵⁺, green; Mo⁶⁺, blue; for S 2s, orange. (c) S 2p: S²⁻, red; S₂²⁻, orange. In all graphs: background, light gray; fit, gray dashed; data is black.

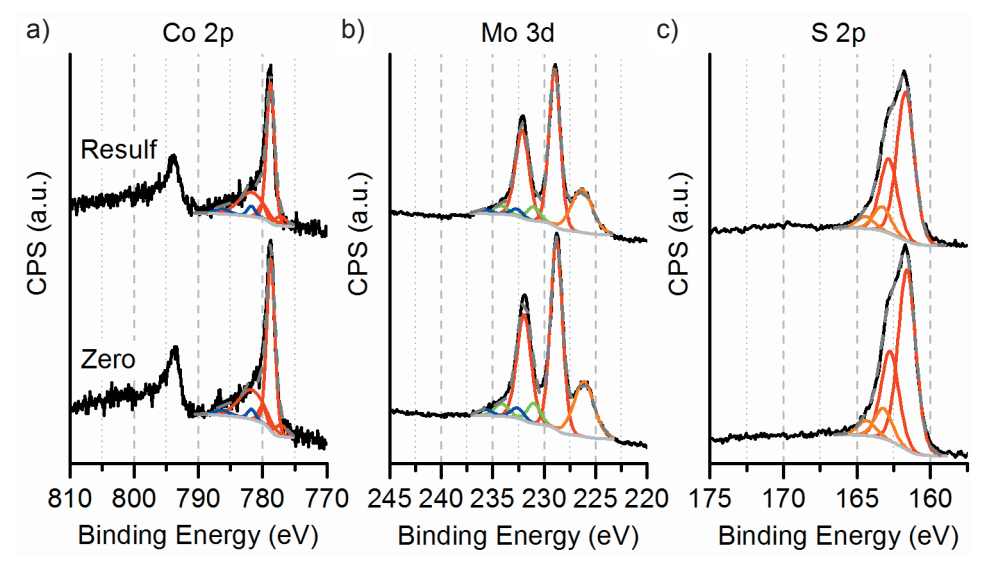


Figure 3.4. XP spectra of NiMoS2, showing the (a) Co 2p, (b) Mo 3d, and (c) S 2p signals after initial sulfidation (Zero) and after the oxidation-resulfidation treatment (Resulf). The deconvolution consists of the following components:(a) Co 2p: CoS_x, red; CoO_x, blue (both include satellites). (b) Mo 3d: Mo⁴⁺, red; Mo⁵⁺, green; Mo⁶⁺, blue; for S 2s, orange. (c) S 2p: S²⁻, red; S₂²⁻, orange. In all graphs: background, light gray; fit, gray dashed; data is black.

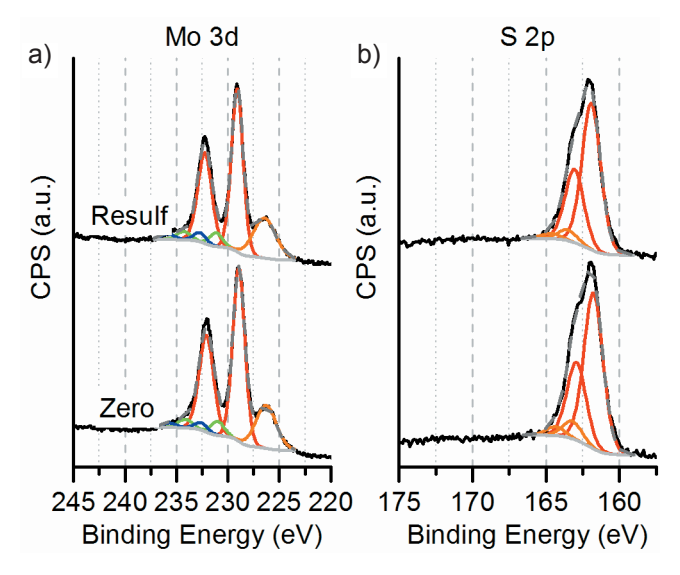


Figure 3.5. XP spectra of MoS2, showing the (a) Mo 3d, and (b) S 2p signals after initial sulfidation (Zero) and after the oxidation-resulfidation treatment (Resulf). The deconvolution consists of the following components: (a) Mo 3d: Mo $^{4+}$, red; Mo $^{5+}$, green; Mo $^{6+}$, blue; for S 2s, orange. (c) S 2p: S $^{2-}$, red; S $_2^{2-}$, orange. In all graphs: background, light gray; fit, gray dashed; data is black.

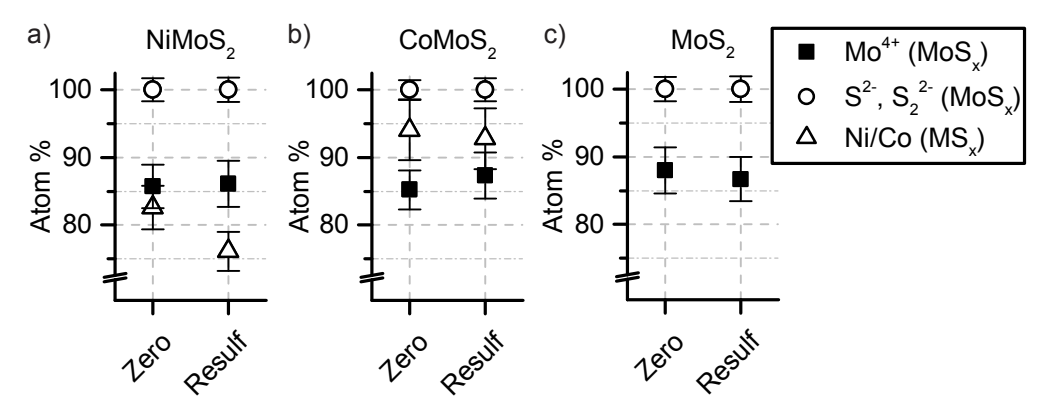


Figure 3.6. Fraction of the species that are present in the sulfidic state (in atom %, as determined by deconvolution of XP spectra). (a) NiMoS₂, (b) CoMoS2, and (c) MoS₂, after initial sulfidation (Zero) and after the oxidation-resulfidation treatment (Resulf). The fraction of sulfided species was calculated from the contributions of MoS₂ (Mo⁴⁺), sulfide anions (S²⁻ and S₂²⁻) and sulfided Ni/Co (M-MoS₂ or MS₃). Statistical error margins are indicated

Table 3.3. Composition (in atom %, determined via deconvolution of XP spectra) of the samples NiMoS₂, CoMoS₂, and MoS₂, as graphically shown in Figure 3.6.

		Ni/Co	Mo	S
NiMoS ₂	Zero	82.6 ± 3.2	85.7 ± 3.2	100.0 ± 1.7
	Resulf	76.1 ± 2.9	86.1 ± 3.4	100.0 ± 1.8
CoMoS ₂	Zero	94.1 ± 4.5	85.2 ± 2.9	100.0 ± 1.5
	Resulf	92.8 ± 4.5	87.3 ± 3.4	100.0 ± 1.7
MoS_2	Zero		88.0 ± 3.4	100.0 ± 1.8
	Resulf		86.7 ± 3.3	100.0 ± 1.9

It should be noted here, that the error margins indicated in Figure 3.6 and Table 3.3 are the calculated statistical errors based on the number of counts in each fitted peak. The total error might be larger, as the background subtraction process is not included in these error values.

In the Ni spectra a significant amount of oxides appeared after the oxidation-resulfidation treatment, as nickel oxidation increased by approximately 7%. This oxidative trend is in agreement with previous studies that showed the Ni/Co promoter atoms to oxidize more readily than Mo and S, and Ni oxidized more deeply after 24 h in air.[8] As it was shown that after 24 h of oxidation all species had significantly oxidized (Ni 39%, Co 24%, Mo 15%, S 6%) it is now clear that resulfidation occurs for all species.

During the initial sulfidation treatment, NTA has the effect of chelating the Ni/Co promoter atoms and causing these promoter atoms to not sulfide below approximately 250 °C, while Mo starts sulfiding at approximately 150 °C already. [18,19] Since NTA decomposes mainly between 200 °C and 400 °C at 1 bar sulfidation pressure, the chelating agents will be removed during the first sulfidation treatment and the chelating effect will be diminished in the second sulfidation treatment. The lack of chelating agents would cause all the formed oxidic species (Ni, Co, Mo) to be sulfided at lower temperatures. [18-20] It is surprising, however, that the Ni promoter atoms, in contrast to Co and Mo, are not sulfided back to their initial degree of sulfidation, but a fraction of the initially sulfided Ni promoter atoms remains oxidized after the resulfidation treatment: The initial sulfidation treatment left 17% of the Ni precursor species in oxidic form, which increased to 24% after oxidation-resulfidation step.

3.3.3 Catalytic activity

The catalytic activity of the samples was measured in gas-phase thiophene HDS at atmospheric pressure. Steady-state activity was determined via a first-order exponential decay fit of the dataset, as shown in Figure 3.7.

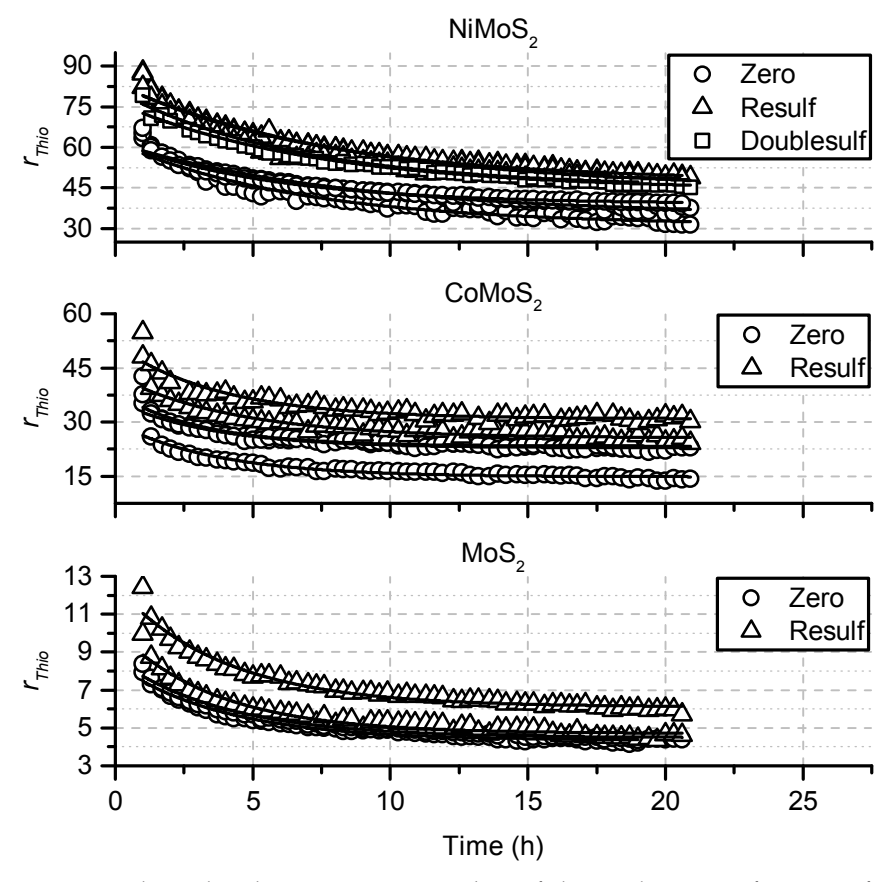


Figure 3.5. Gas-phase thiophene HDS activity data of the catalysts as a function of time, including first-order exponential decay fits (solid lines).

For each type of catalyst, activity data were obtained for two or three individual samples. For comparison, an additional NiMoS2 sample was treated with a second sulfidation treatment, without the 24 h oxidation treatment in between. This sample is labeled 'Doublesulf'. Afterwards, the average steady-state activity was determined per group of samples. The resulting average activity data are shown in Table 3.4.

Table 3.4. Average steady-state catalytic activity data, normalized per mole of Mo, for gasphase thiophene HDS.

Average r_{Thio} (mol _{Thio} mol _{Mo} ⁻¹ h ⁻¹) ± standard error of fit						
NiMoS ₂ CoMoS ₂ MoS ₂						
Zero	37.0 ± 2.9	20.3 ± 4.8	4.4 ± 0.1			
Resulf	46.0 ± 2.1	28.2 ± 3.8	5.4 ± 1.0			
Doublesulf	44.2 ± 0.3					

Oxidation-resulfidation treatment clearly has a positive effect on the steady-state activity of the catalysts. All three samples show an increase of over 20%, while CoMoS₂ exhibits the largest activity increase with 39%. Also, the Doublesulf NiMoS₂ sample showed a similar increase in HDS activity.

The activity that is measured for the first data point highly depends on the time between the moment that the thiophene flow is introduced to the reactor and the moment that the chromatograph starts measuring the first products. As this time might vary between different measurements, the first data point is subject to a variable error. Also, the fit does not perfectly cover the first few data points. We have verified however that varying the exact value of this first data point, both to a significantly higher or lower value, has a negligible effect on the eventual steady-state activity value that is determined by the fitting procedure.

Also, the activity values as determined via the fitting procedure deviated little from the activity values as calculated via the regular method (the average of the last 4~5h). For all the samples, the deviation was between 0% and 2%, except for the NiMoS₂ Resulf and Doublesulf tests which deviated 5% and 6%, respectively.

3.3.4 Discussion

The slab length analysis shows that (Ni/Co)MoS₂ slab length is increasing on average after the oxidation-resulfidation treatment. The number of smaller slabs, below a size of 1.5 nm, is decreasing, as is visible especially in the left shoulders of Figures 3.1a and 3.1c. Still, the HDS activity of all catalyst samples is increasing significantly. From previous research it is known that only the edges of the (Ni/Co) MoS₂ slabs are catalytically active,[21,22] so from this perspective it is surprising that a catalyst sample that has larger particles and thus relatively less active edges available, is more active. The increase in activity might be caused by a redispersion process of the catalyst and its promoter atoms during the second heating step of the resulfidation treatment. The effect of the oxidation-resulfidation treatment might

also be that the catalyst particles are now less well-crystallized, as was observed in previous experiments and which was suggested to cause more active sites for HDS. [23]

Another potential explanation could be that there is a minimum size that a (Ni/ Co)MoS $_2$ slab should have, above which it is catalytically (more) active. Since the initially sulfided samples contain a larger proportion of smaller (< 1.5 nm) slabs, these slabs could fully oxidize during the oxidation treatment, and then redisperse and form larger, more active slabs during the second sulfidation treatment. This hypothesis is in line with the observation from Lauritsen *et al.*, where it was shown that MoS $_2$ nanostructures comprising less than 15 Mo edge atoms (21 atoms in total, particle size < ~1.6 nm) do not show the so-called electronic brim state that is believed to play an important role in HDS catalysis.[24,25]

In view of this hypothesis, it might be favorable to tailor a (Ni/Co)MoS₂ catalyst in such a way that the size distribution of the formed slabs is more narrow than is conventionally obtained via standard preparation methods, while the number of slabs smaller than ~1.6 nm is minimized. It might be that for this, a sequence of oxidation-resulfidation treatments could be beneficial.

3.4 Conclusion

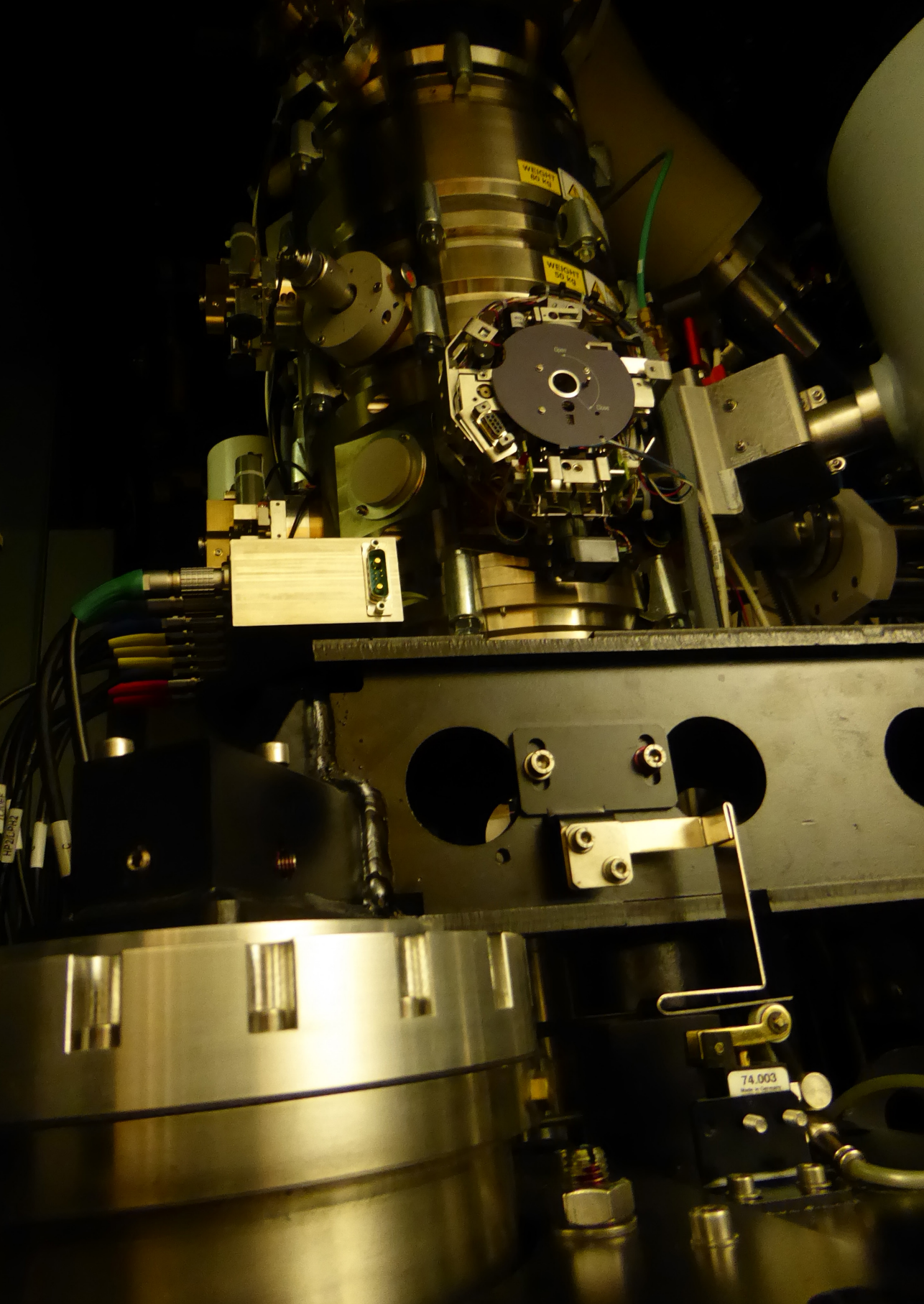
(Ni/Co)MoS₂ slabs were prepared via an initial sulfidation step, and subsequently subjected to a 24 h oxidation and second sulfidation treatment. From HRTEM imaging it appeared that after oxidation and resulfidation the (Ni/Co)MoS₂ slabs were growing back to their original length. The average slab length increased, while the slab length distribution of the samples changed to a less widely dispersed distribution histogram. XPS showed that the Ni/Co promoter atoms were more oxidized after oxidation-resulfidation, compared to the initial sulfidation treatment. The oxidized molybdenum and the sulfur returned to the freshly sulfided state after resulfidation, as before oxidation. Moreover, the oxidation-resulfidation cycle made all samples more active HDS catalysts in gas-phase thiophene HDS measurements, showing an activity increase of up to 39%. We suggest that this increase in HDS activity might be due to redistribution of the (Ni/Co)MoS₂ slabs during the second sulfidation treatment. This could indicate a size effect of the catalyst, as smaller slabs (< ~1.6 nm) might be less active, and after a second sulfidation treatment the number of smaller slabs decreases significantly.

References

- [1] Environmental Protection Agency. Control of Air Pollution From Motor Vehicles: Tier 3 Motor Vehicle Emission and Fuel Standards; Final Rule; **2014**, Vol. 79.
- [2] Hensen, E. J. M.; de Beer, V. H. J.; van Veen, J. A. R.; van Santen, R. A. A Refinement on the Notion of Type I and II (Co)MoS Phases in Hydrotreating Catalysts. *Catal. Lett.* **2002**, *84* (1/2), 59–67 DOI: 10.1023/A:1021024617582.
- [3] Egorova, M.; Prins, R. The Role of Ni and Co Promoters in the Simultaneous HDS of Dibenzothiophene and HDN of Amines Over Mo/ γ -Al₂O₃ Catalysts. *J. Catal.* **2006**, 241 (1), 162–172 DOI: 10.1016/j.jcat.2006.04.011.
- [4] Eijsbouts, S.; Heinerman, J.; Elzerman, H. MoS₂ Structures in High-Activity Hydrotreating Catalysts. *Appl. Catal. A.* **1993**, *105* (1), 53–68 DOI: 10.1016/0926-860X(93)85133-A.
- [5] Eijsbouts, S.; Heinerman, J.; Elzerman, H. MoS₂ Structures in High Activity Hydrotreating Catalysts. II. Evolution of the Active Phase During the Catalyst Life Cycle. Deactivation Model. *Appl. Catal. A.* **1993**, *105* (1), 69–82 DOI: 10.1016/0926-860X(93)85134-B.
- [6] Byskov, L. S.; Nørskov, J. K.; Clausen, B. S.; Topsøe, H. DFT Calculations of Unpromoted and Promoted MoS₂-Based Hydrodesulfurization Catalysts. *J. Catal.* **1999**, *187* (1), 109–122 DOI: 10.1006/jcat.1999.2598.
- [7] Kooyman, P. J.; van Veen, J. A. R. The Detrimental Effect of Exposure to Air on Supported MoS_2 . Catal. Today **2008**, 130 (1), 135–138 DOI: 10.1016/j. cattod.2007.07.019.
- [8] Bremmer, G. M.; van Haandel, L.; Hensen, E. J. M.; Frenken, J. W. M.; Kooyman, P. J. Instability of Nimos₂ And Comos₂ Hydrodesulfurization Catalysts at Ambient Conditions: a Quasi *in Situ* High-Resolution Transmission Electron Microscopy and X-Ray Photoelectron Spectroscopy Study. *J. Phys. Chem. C* **2016**, 120 (34), 19204–19211 DOI: 10.1021/acs.jpcc.6b06030.
- [9] Dugulan, A. I.; Hensen, E. J. M.; van Veen, J. A. R. High-Pressure Sulfidation of a Calcined CoMo/ Al_2O_3 Hydrodesulfurization Catalyst. *Catal. Today* **2008**, *130* (1), 126–134 DOI: 10.1016/j.cattod.2007.06.075.
- [10] Zandbergen, H.; Kooyman, P. J.; van Langeveld, A. D. Transfer Systems for Insertion of Specimens Into Electron Microscopes Under Controlled Atmospheres; *Electron Microscopy* 1998: *Proceedings of the 14th International Congress on Electron Microscopy*, Cancun, Mexico, August 31 September 4, **1998**; Vol. II, 491–492.
- [11] Datye, A. K.; Xu, Q.; Kharas, K. C.; McCarty, J. M. Particle Size Distributions in Heterogeneous Catalysts: What Do They Tell Us About the Sintering Mechanism? *Catal. Today* **2006**, *111* (1-2), 59–67 DOI: 10.1016/j.cattod.2005.10.013.
- [12] Haynes, H. W. Effect of Particle Size Distribution on Catalyst Effectiveness. *J. Catal.* **1983**, 79, 470–474.
- [13] Renaud, G.; Lazzari, R.; Revenant, C.; Barbier, A.; Noblet, M.; Ulrich, O.; Leroy, F.; Jupille, J.; Borensztein, Y.; Henry, C. R.; *et al.* Real-Time Monitoring of Growing Nanoparticles. *Science* **2003**, *300* (5624), 1416–1419 DOI: 10.1126/science.1082146.
- [14] Granqvist, C. G.; Buhrman, R. A. Size Distributions for Supported Metal

- Catalysts: Coalescence Growth Versus Ostwald Ripening. *J. Catal.* **1976**, 42 (3), 477–479 DOI: 10.1016/0021-9517(76)90125-1.
- [15] Weber, T.; Muijsers, J. C.; Van Wolput, J.; Verhagen, C. P. J.; Niemantsverdriet, J. W. Basic Reaction Steps in the Sulfidation of Crystalline MoO₃ To MoS₂, As Studied by X-Ray Photoelectron and Infrared Emission Spectroscopy. *J. Phys. Chem.* **1996**, 100 (33), 14144–14150 DOI: 10.1021/jp961204y.
- [16] Alstrup, I.; Chorkendorff, I.; Candia, R.; Clausen, B. S.; Topsøe, H. A Combined X-Ray Photoelectron and Mössbauer Emission Spectroscopy Study of the State of Cobalt in Sulfided, Supported, and Unsupported Co-Mo Catalysts. *J. Catal.* **1982**, 77 (2), 397–409 DOI: 10.1016/0021-9517(82)90181-6.
- [17] Gandubert, A. D.; Legens, C.; Guillaume, D.; Rebours, S.; Payen, E. X-Ray Photoelectron Spectroscopy Surface Quantification of Sulfided CoMoP Catalysts Relation Between Activity and Promoted Sites Part I: Influence of the Co/Mo Ratio. *Oil Gas Sci. Technol.* **2007**, *62* (1), 79–89 DOI: 10.2516/ogst:2007007.
- [18] Coulier, L.; de Beer, V. H. J.; van Veen, J. A. R.; Niemantsverdriet, J. W. Correlation Between Hydrodesulfurization Activity and Order of Ni and Mo Sulfidation in Planar Silica-Supported NiMo Catalysts: the Influence of Chelating Agents. *J. Catal.* **2001**, 197 (1), 26–33 DOI: 10.1006/jcat.2000.3068.
- [19] van Haandel, L.; Bremmer, G. M.; Hensen, E. J. M.; Weber, T. The Effect of Organic Additives and Phosphoric Acid on Sulfidation and Activity of (Co)Mo/Al₂O₃ Hydrodesulfurization Catalysts. *J. Catal.* **2017**, *351*, 95–106 DOI: 10.1016/j. jcat.2017.04.012.
- [20] van Haandel, L.; Kooyman, P. J.; van Veen, J. A. R.; Weber, T.; Hensen, E. J. M.; Bremmer, G. M. Structure–Activity Correlations in Hydrodesulfurization Reactions Over Ni-Promoted $\mathrm{Mo_{x}W(_{1-x})S_{2}/Al_{2}O_{3}}$ Catalysts. *ACS Catal.* **2015**, 7276–7287 DOI: 10.1021/acscatal.5b01806.
- [21] Salmeron, M.; Somorjai, G. A.; Wold, A.; Chianelli, R.; Liang, K. S. The Adsorption and Binding of Thiophene, Butene and H₂S on the Basal Plane of MoS2 Single Crystals. *Chem. Phys. Lett.* **1982**, *90* (2), 105–107 DOI: 10.1016/0009-2614(82)83620-8.
- [22] Kushmerick, J. G.; Weiss, P. S. Mobile Promoters on Anisotropic Catalysts: Nickel on MoS₂; *J. Phys. Chem. B*, **1998**, 102, 10094–10097 DOI: 10.1021/jp982752.
- [23] Kooyman, P. J.; Buglass, J. G.; Reinhoudt, H. R.; van Langeveld, A. D.; Hensen, E. J. M.; Zandbergen, H.; van Veen, J. A. R. Quasi *in Situ* Sequential Sulfidation of CoMo/Al₂O₃ Studied Using High-Resolution Electron Microscopy. *J. Phys. Chem. B* **2002**, *106* (45), 11795–11799 DOI: 10.1021/jp0256701.
- [24] Lauritsen, J. V.; Kibsgaard, J.; Helveg, S.; Topsøe, H.; Clausen, B. S.; Lægsgaard, E.; Besenbacher, F. Size-Dependent Structure of MoS₂ Nanocrystals. *Nat. Nanotechnol.* **2007**, 2 (1), 53–58 DOI: 10.1038/nnano.2006.171.
- [25] Besenbacher, F.; Brorson, M.; Clausen, B. S.; Helveg, S.; Hinnemann, B.; Kibsgaard, J.; Lauritsen, J. V.; Moses, P. G.; Nørskov, J. K.; Topsøe, H. Recent STM, DFT and HAADF-STEM Studies of Sulfide-Based Hydrotreating Catalysts: Insight Into Mechanistic, Structural and Particle Size Effects. *Catal. Today* **2008**, *130* (1), 86–96 DOI: 10.1016/j.cattod.2007.08.009.





CHAPTER 4

Cobalt-rhenium β -Mn-type bimetallic nanoparticles prepared via colloidal chemistry

We report on the synthesis, thermal stability and structural evolution of β -manganese (Mn)-type cobalt (Co)-rhenium (Re) nanoparticles (NPs). Monodisperse Co_{1-x}Re_x NPs are synthesized for the first time via a facile one-pot colloidal method, yielding excellent control of Re stoichiometry for $x \le 0.15$. Scanning transmission electron microscopy-energy dispersive X-ray spectroscopy analysis demonstrates that the Re atoms are homogeneously distributed throughout the Co lattice. Synchrotron powder X-ray diffraction combined with Rietveld refinement shows clear preferential site occupancy of Re atoms in the 12-fold site. A maximum of 15 atom % Re can be incorporated into the Co lattice, yielding single-phase particles. *In situ* synchrotron powder X-ray diffraction heating studies show that in reducing atmosphere the β -Mn-type Co–Re NPs are stable up to 300 °C before transforming into hexagonal close-packed Co, implying Re segregation.

4.1 Introduction

Bimetallic nanoparticles (NPs) attract significant attention due to the immense technological potential that arises from size, morphology and compositional effects. [1-5] In catalytic processes, bimetallic NPs often exhibit superior performance compared to their monometallic counterparts. [6-8] The enhanced catalytic performance may originate from synergy between a modified electronic structure and the formation of new active sites, induced by the local presence of the second metallic element.[9,10] Co-Re NPs are of interest in catalytic processes such as the Fischer-Tropsch reaction and ammonia synthesis.[11-17] In the presence of small amounts of Re, the overall Fischer-Tropsch performance of Co in terms of activity and selectivity towards longchain hydrocarbons (C_{5,1}) is enhanced.[18-20] One long lasting debate, addressed both experimentally and theoretically, is the location of the Re promoter in the Co particles. While some studies indicate that Re is distributed inside the bulk Co matrix forming an alloy, [21] others propose that Re atoms accumulate on the surface in intimate contact with Co metal nanoparticles, [22] or that Re is located just below a surface consisting of Co atoms. [23] In these experimental studies, [21,22] the Co-Re bimetallic catalysts are prepared by wet impregnation, which gives limited control of parameters such as particle size and elemental distribution. A more targeted strategy would be the synthesis of free-standing Co-Re NPs via colloidal chemistry with subsequent deposition on a selected support material. [24-28] To the best of our knowledge, synthetic protocols for colloidal Co-Re NPs are currently unavailable. In this communication we report on a method to synthesize monodisperse Co-Re NPs with the β -Mn-type structure, a structure found for monometallic Co NPs.[29,30]

4.2 Experimental

4.2.1 Synthesis of Co-Re nanoparticles

Uniformly sized $Co_{1-x}Re_x$ ($x \le 0.15$) NPs were synthesized by thermal decomposition of dicobalt octacarbonyl ($Co_2(CO)_8$, $\ge 90\%$) and dirhenium decacarbonyl ($Re_2(CO)_{10}$, 98%) metal precursors in ortho-dichlorobenzene (o-DCB, 99%, anhydrous) containing oleic acid ($OA \ge 99\%$) as stabilizing agent. All chemicals were purchased from Sigma-Aldrich and used without further purification.

For the synthesis of Co–Re NPs, the previously reported protocol for the synthesis of Co NPs [31] was subjected to various modifications (Figure 4.1). In a typical $Co_{0.85}Re_{0.15}$ NP synthesis, 0.20 mmol $Re_2(CO)_{10}$ and 65 μ L OA (0.205 mmol) were dissolved in 15 mL o-DCB under Ar flow. The solution was subsequently heated to 177 \pm 1 °C under stirring conditions. In the meantime, 1.11 mmol $Co_2(CO)_8$ was dissolved in 3 mL o-DCB in a glove box (O₂ and H₂O levels <1 ppm).

When the o-DCB/OA/Re₂(CO)₁₀ mixture reached the targeted temperature, the Co₂(CO)₈ precursor solution was rapidly injected into the hot mixture. The formed colloidal suspension was aged for 2-4 hours and subsequently quenched with 10 mL fresh o-DCB. The NPs were flocculated using excess 2-propanol and isolated by centrifugation. After discarding the supernatant, the NP precipitate was washed with 2-propanol for at least three times before redispersion in hexane. In order to tune the Co-Re metal composition, the relative amounts of Co and Re carbonyl precursors were systematically adjusted (Table 4.1).

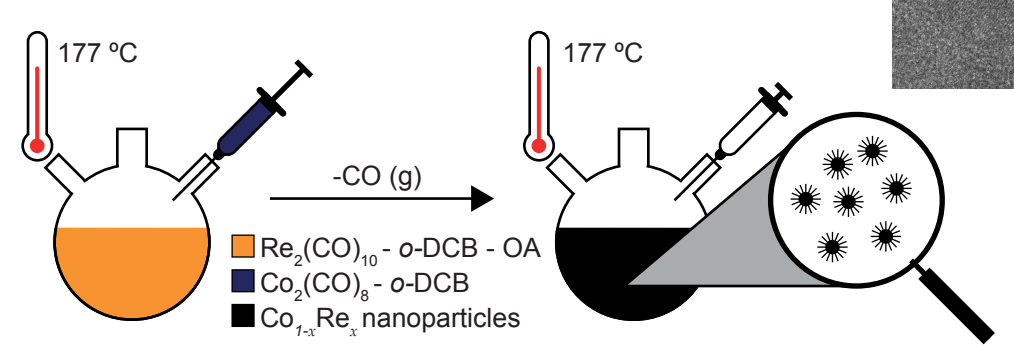


Figure 4.1. Colloidal Co–Re NPs formed via thermal decomposition of carbonyl precursors in the presence of OA as stabilizing agent and *o*-DCB as solvent.

Table 4.1. Amounts of reactants used for the preparation of Co_{1-x}Re_x Nanoparticles.

	Co ₂ (CO) ₈		Re ₂ (CO) ₁₀		o-DCB	OA
Sample	mg	mmol	mg	mmol	mL	mmol
$Co_{0.97}Re_{0.03}$	440	1.286	28	0.043	18	0.205
$Co_{0.92}Re_{0.08}$	420	1.228	72	0.110	18	0.205
$Co_{0.85}Re_{0.15}$	380	1.111	132	0.202	18	0.205
${\rm Co_{0.60}Re_{0.40}}$	270	0.789	354	0.543	18	0.205

4.2.2 Nanoparticle characterization

The crystal structure and thermal stability of Co-Re NPs were investigated by synchrotron powder X-ray diffraction (SR-PXRD). All the experiments were performed at the Swiss-Norwegian Beamlines (SNBL), station BM01A, at the European Synchrotron Radiation Facility (ESRF). Diffraction profiles were collected using a PILATUS 2M detector. Wavelength ($\lambda = 0.06957$ nm) was calibrated by means of a NIST Si standard. For data reduction a PyFAI-based tool was used.[32] For structural investigations, dried samples were loaded (inside a glove box, O₂ and H₂O levels <1 ppm) in 0.7 mm diameter glass capillaries and sealed. Sets of diffraction patterns were collected at room temperature and the intensities were averaged to improve statistics. Rietveld refinements were performed using the Fullprof suite of programs [33] (2 Θ range 10-37°; Δ 2 Θ = 0.0125°; 30 Bragg reflections, 10-13 variable parameters; manual background correction; typical Bragg $R_{\rm p}$ factor = 4.3, $R_{\rm p}$ = 10.4). For the temperature-dependent SR-PXRD experiments, an inhouse-made quartz capillary-based in situ cell was used. The $Co_{0.85}Re_{0.15}$ sample was loaded (inside a glove box) in a 0.7 mm diameter quartz capillary, with a bed length of ~10 mm, and kept in place by quartz wool plugs. Sample heating was provided by a vertical hot air blower. Flowing gas was supplied by a set of mass flow controllers calibrated for relatively small flows (~5 mL min⁻¹). A 4 vol. % H₂/He gas mixture (Messer Schweiz AG, 99.2%) was used. The sample was heated *in situ* over the temperature range 27 – 402 °C at a rate of 2 °C min⁻¹. The diffraction patterns were recorded simultaneously using a collection rate of 4 images min⁻¹.

High-resolution transmission electron microscopy (HRTEM) and scanning transmission electron microscopy (STEM) was performed using a Cs-corrected FEI Titan Cubed microscope operating at 300 kV, equipped with a Gatan US1000 2k x 2k CCD, a Direct Electron DE-12 4k x 3k CCD and a high-angle annular dark-field (HAADF) detector, or with a monochromated FEI Tecnai F20ST/STEM operating at 200 kV, equipped with a Gatan US4000 4k x 4x CCD. Both microscopes were equipped with an energy dispersive X-ray (EDX) detector (Oxford Instruments, X-MAX^N 100TLE Windowless) for EDX spectroscopy. Analysis of (STEM-)EDX data was done using AZTec software, version 3.1.

All TEM samples were prepared by drop casting 10 μ L of the relevant NP dispersion onto ultrathin carbon film (< 3 nm) supported by lacey carbon film on 400 mesh copper grids (Ted Pella Inc.) and dried under inert atmosphere.

4.3 Results and discussion

4.3.1 Characterization of Co-Re nanoparticles

The NP composition was determined using HRTEM-EDX. Analysis of a number of single Co–Re NPs showed signals of both Co and Re, confirming their bimetallic nature. The average stoichiometries are summarized in Table 4.2 and Figure 4.2.

Table 4.2. Composition of Co-Re NPs, as determined by HRTEM-EDX.

Sample	Atom % Re ^a		
$Co_{0.97}Re_{0.03}$	N.D. ^b		
$Co_{0.92}Re_{0.08}$	5.1 ± 0.9		
$Co_{0.85}Re_{0.15}$	12.2 ± 1.3		

^a Measurements on randomly selected single NPs, averaged.

^b N.D. Not determined.

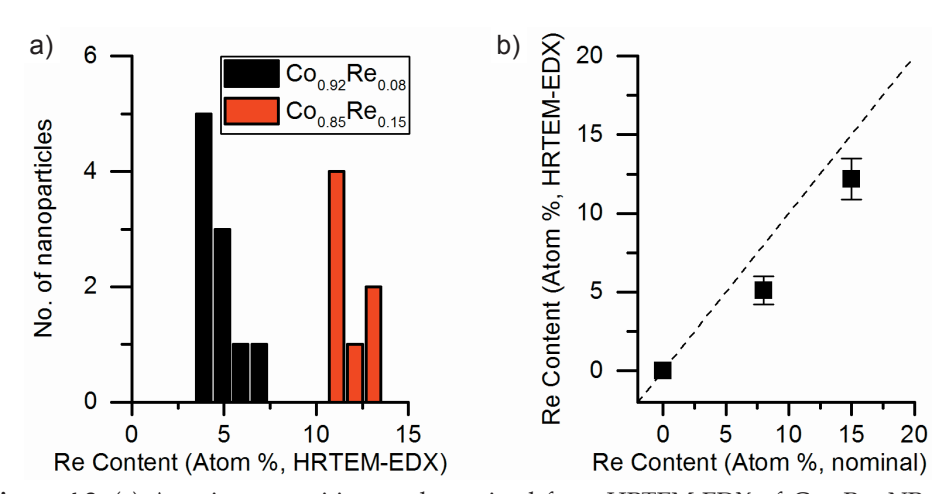


Figure 4.2. (a) Atomic composition as determined from HRTEM-EDX of $Co_{1-x}Re_x$ NPs on single nanoparticles. (b) Averaged composition (data points) determined by HRTEM-EDX versus nominal composition.



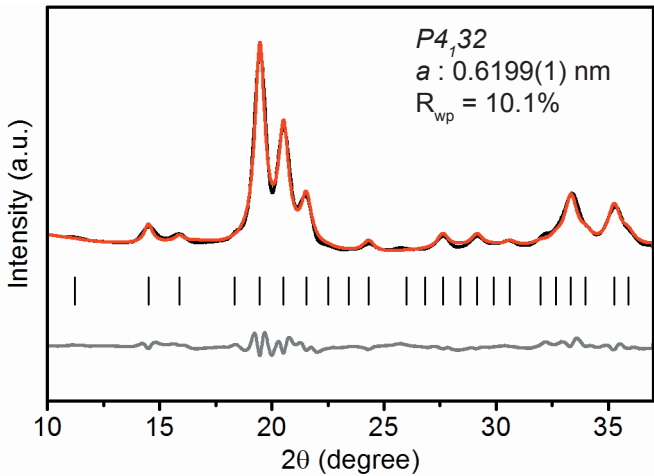


Figure 4.3. SR-PXRD pattern of $Co_{0.85}Re_{0.15}$ NPs (black) and corresponding Rietveld refinement. The calculated (red) and difference (gray) profiles are shown along with the positions for the Bragg reflections (vertical bars). $\lambda = 0.06957$ nm.

Figure 4.3 shows the SR-PXRD pattern of Co–Re NPs with nominal composition $Co_{0.85}Re_{0.15}$. Rietveld refinement using the structural model reported by Dinega and Bawendi [29] confirmed that the Co-Re NPs crystallize in the cubic β -Mn-type structure (space group $P4_132$). The refined crystallographic parameters are reported in Table 4.3. The Rietveld fit showed clear preferential site occupancy for Re-atoms in the 12-fold site.

Table 4.3. Crystallographic data^a of *β*-Mn-type Co–Re NPs with nominal composition $Co_{0.85}Re_{0.15}$.

Species	Site	X	у	Z	Occupancy
Co1 x,x,x	8 <i>c</i>	0.0634(5)	0.0634(5)	0.0634(5)	0.666(1)
Re1 x,x,x	8 <i>c</i>	0.0634(5)	0.0634(5)	0.0634(5)	0.000(1)
Co2 1/8,y,z	12 <i>d</i>	0.125	0.193(2)	0.461(1)	0.818(7)
Re2 1/8,y,z	12 <i>d</i>	0.125	0.193(2)	0.461(1)	0.182(7)

 $^{^{}a}$ T = 20 °C; Rwp = 10.1%; Space group: $P4_{3}32$; Unit cell parameter, a = 0.6199(1) nm.

Figure 4.4 illustrates the moderate differences in the diffraction profiles depending on the Re-site distribution (Re at the 8-fold site; Re at the 12-fold site; random Co/Re distribution). For Co- or Mn-based bimetallic β -Mn-type solid solutions, both 8-fold and 12-fold site preferences have been reported.[33-35] Furthermore, it is evident that the unit cell expands upon Re incorporation. By assuming a linear relationship in the *a*-axis between the two end members Co and Re (β -Mn-type structure) [a = 0.6098(3) nm for Co [31]; and 0.697(2) nm for Re [36]] the refined value a = 0.6199(1) nm for the synthesized Co_{0.85}Re_{0.15} NPs corresponds to a Re incorporation of 11.7 atom %. This value is in good agreement with the Re content (12.2 ± 1.3 atom %) determined by HRTEM-EDX (Table 4.2).

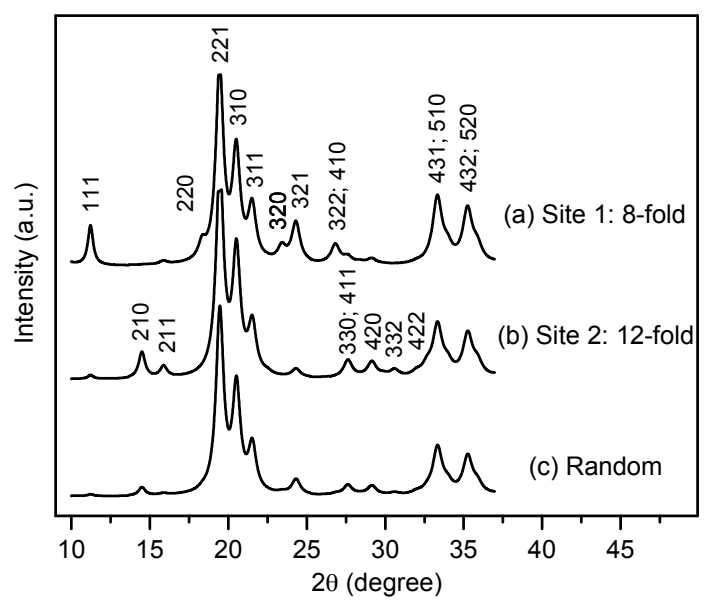


Figure 4.4. Calculated X-ray diffraction patterns of β -Mn-type Co–Re (Re, 1/6 fraction). In the simulated patterns, all Re atoms are assumed to occupy only (a) site 1 (8-fold); (b) site 2 (12-fold); or (c) are randomly distributed in the β -Mn-type Co lattice.

A representative high-angle annular dark-field scanning transmission electron microscopy (HAADF-STEM) image of the ${\rm Co_{0.85}Re_{0.15}}$ NPs is shown in Figure 4.5a. The as-prepared particles have a spherical shape with an average diameter of 8 nm and a narrow size distribution (11% variation in diameter); as shown in Figure 4.5b.

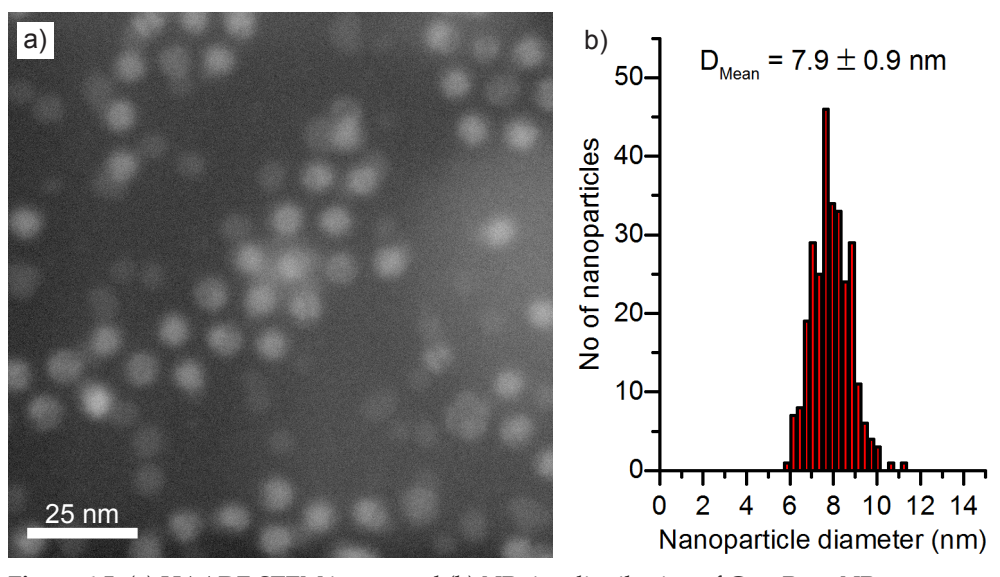


Figure 4.5. (a) HAADF-STEM image and (b) NP size distribution of $Co_{0.85}Re_{0.15}$ NPs.

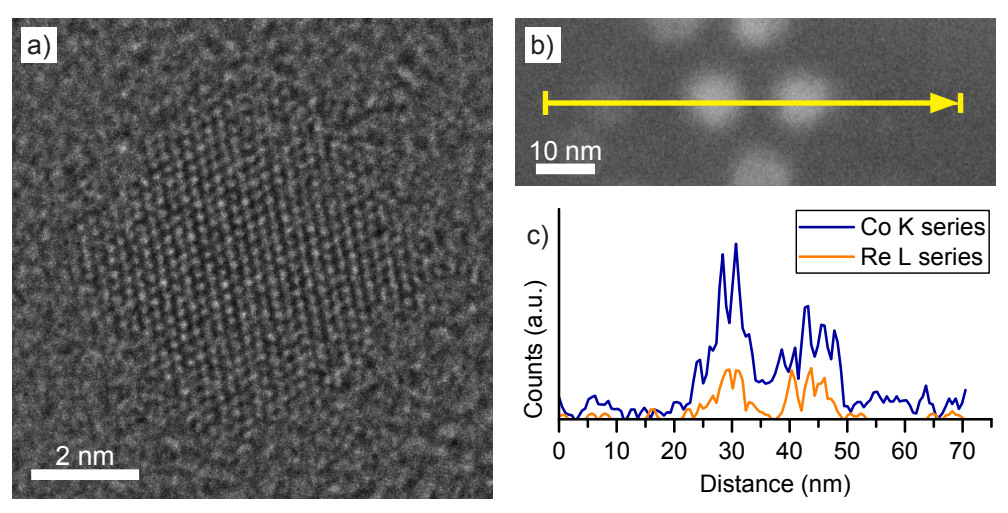


Figure 4.6. (a) HRTEM image of a single $Co_{0.85}Re_{0.15}$ nanoparticle. (b) HAADF-STEM image of multiple $Co_{0.85}Re_{0.15}$ NPs and (c) the corresponding STEM-EDX line scan profile recorded along the arrow direction.

HRTEM (Figure 4.6a) reveals homogeneous lattice fringes and a periodic lattice with no indications of Re segregation. To further investigate the elemental distribution in the individual NPs, STEM-EDX line scans were recorded (Figure 4.6b-c). The compositional line profiles across the two ${\rm Co_{0.85}Re_{0.15}}$ NPs (Figure 4.6c) show homogeneous Co and Re distributions. These results indicate atomic-level mixing in the ${\rm Co_{0.85}Re_{0.15}}$ crystallites. Based on SR-PXRD and STEM-EDX results, we conclude that the as-prepared ${\rm Co_{0.85}Re_{0.15}}$ NPs form a solid solution.

4.3.2 Varying the Co-Re composition

Compositional tuning of the $Co_{1-x}Re_x$ ($x \le 0.15$) NPs was achieved by adjusting the relative molar ratio between the two metal carbonyl precursors. Figure 4.7 shows the SR-PXRD patterns and Rietveld refinements of NPs with varying Re content. Careful inspection of the SR-PXRD patterns gave no indication for the existence of any crystalline phases with a high Re content; only Bragg reflections originating from the cubic β -Mn-type structure were identified.

For the Co_{0.97}Re_{0.03} sample, SR-PXRD revealed some weak additional reflections (indicated by asterisk in Figure 4.7a). The origin of these reflections is not fully understood; however, possibly some can be related to hcp/ccp intergrowth particles. [31] It is worth mentioning that with increasing Re content (Figure 4.7b-c) the above mentioned reflections disappear, yielding single-phase particles.

Furthermore, an expansion in the *a*-axis with increasing Re content for $x \le 0.15$ was observed for $\text{Co}_{1-x}\text{Re}_x$ (see Figure 4.8), in good agreement with what is expected from Vegard´s law approximation (dashed line).[37,38]

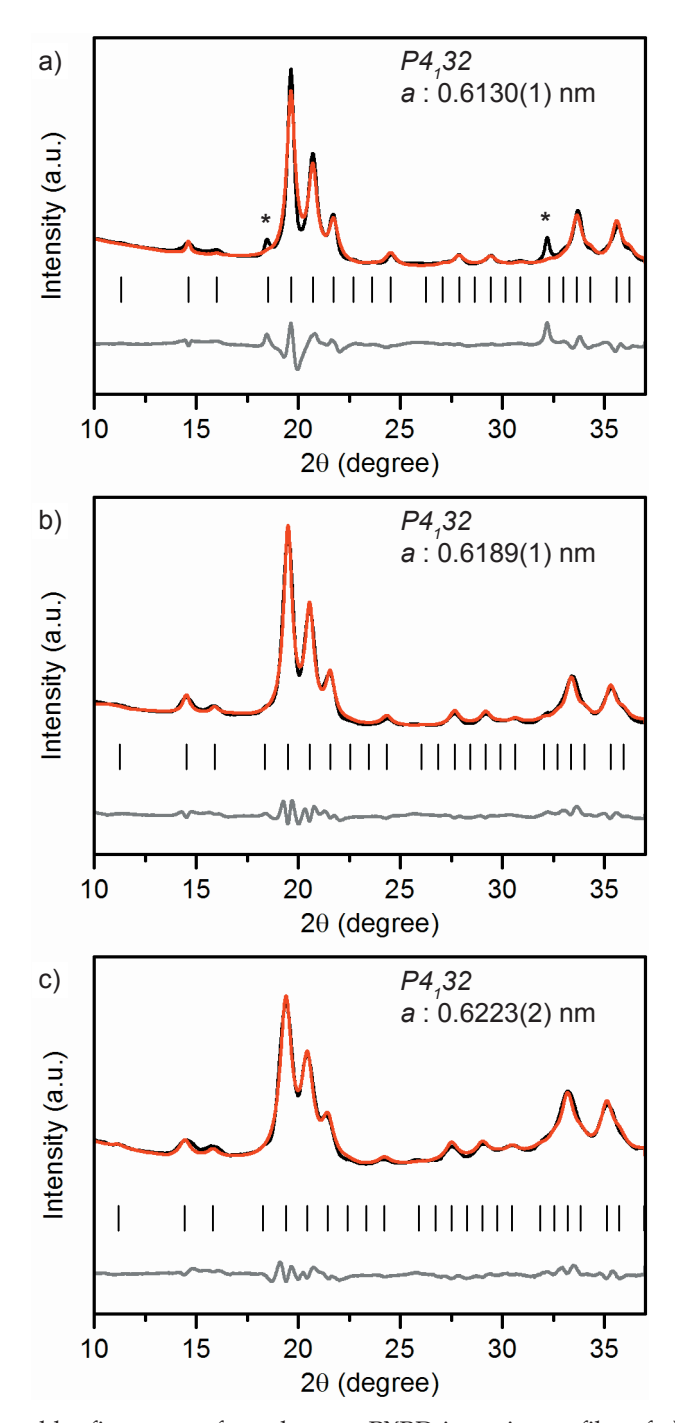


Figure 4.7. Rietveld refinements of synchrotron PXRD intensity profiles of a) $Co_{0.97}Re_{0.03}$; b) $Co_{0.92}Re_{0.08}$; and c) $Co_{0.60}Re_{0.40}$ NPs. Observed (black), calculated (red) and difference (gray) profiles are shown along with the positions for Bragg reflections (vertical bars). Impurity denoted with asterisk (*). $\lambda = 0.06957$ nm.

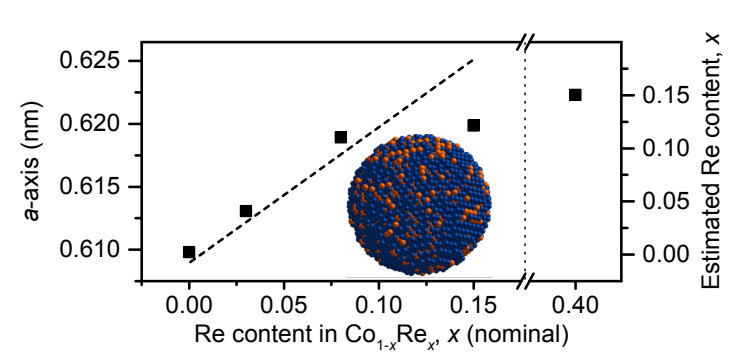


Figure 4.8. Refined *a*-axis (from SR-PXRD) versus nominal Re content for $Co_{1-x}Re_x$ NPs. Dashed line represents Vegard's law linear relation. Estimated Re content (based on Vegard's law) included on the right y-axis, along with a proposed graphical representation of the Co (blue) and Re (orange) atom distribution within the $Co_{1-x}Re_x$ particles ($x \le 0.15$).

4.3.3 High Re content

However, we did not obtain uniform, single phased $Co_{1-x}Re_x$ NPs for x > 0.15. Attempts to synthesize such particles under our reaction conditions always resulted in a product with a Re content of ~15 atom %, as estimated from SR-PXRD. For example, SR-PXRD analysis of $Co_{0.60}Re_{0.40}$ gave a = 0.6223(1) nm (Figure 4.7c), corresponding to an estimated Re incorporation of 14.3 atom % (Figure 4.8).

While no other crystalline phases were detected by SR-PXRD, complementary TEM investigations of $Co_{0.60}Re_{0.40}$ revealed that the sample is highly inhomogeneous both with respect to particle size and chemical composition of the individual particles. Representative TEM images of the $Co_{0.60}Re_{0.40}$ NPs are presented in Figure 4.9. The particles are characterized by a tri-modal size distribution; the main population being spherical bimetallic Co–Re NPs with an average diameter of ca. 7 nm. Some ultra-small clusters and larger aggregates (with sizes of ~1 nm and 50–70 nm, respectively) were also identified. STEM-EDX mapping suggests that the latter are Re-rich (Figure 4.10). Our findings clearly suggest that within the explored experimental window, the solubility limit of Re into single-phased β -Mn-type Co NPs is ~15 atom %.

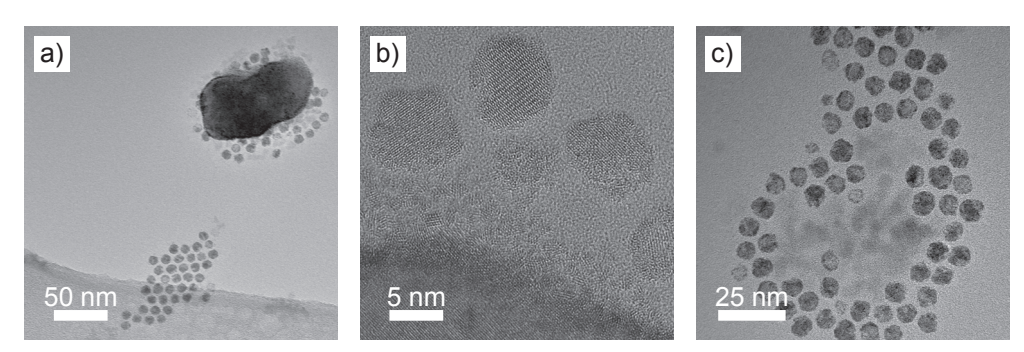


Figure 4.9. Representative TEM images of $Co_{0.60}Re_{0.40}$ on lacey carbon grid. (a) An ~80 nm-sized, Re-rich particle surrounded by Co-Re NPs. (b) High magnification image of a large Re-rich particle (bottom left corner) covered with ~1 nm clusters and a few Co-Re NPs of about 7 nm. (c) Cluster of Co-Re NPs of about 7 nm in size.

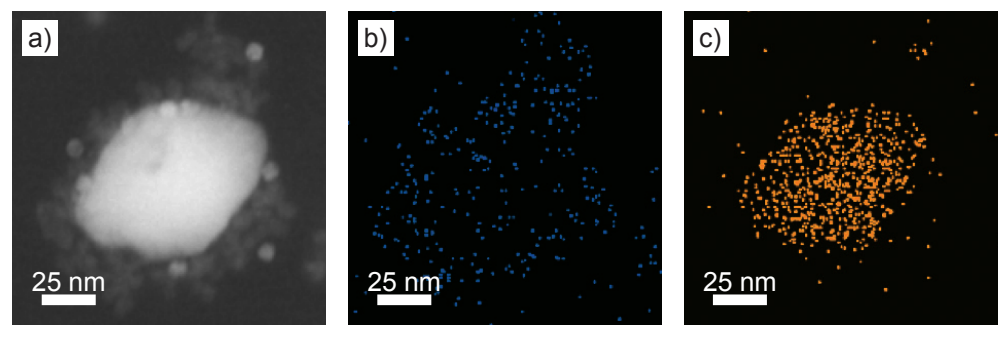


Figure 4.10. TEM images of the Co_{0.60}Re_{0.40} sample on lacey carbon grid (a) HAADF-STEM image of a large Re-rich particle. (b) and (c) show the corresponding STEM-EDX mapping images of the Co K series (blue) and the Re L series (orange), respectively.

4.3.4 Thermal stability

The thermal stability of the β -Mn-type Co_{0.85}Re_{0.15} NPs was studied by *in situ* SR-PXRD. Figure 4.11a shows a contour plot of the diffraction patterns from 27 – 402 °C upon heating in diluted H₂. Selected 2D-patterns are presented in Figure 4.11b. Upon heating, all Bragg reflections of the β -Mn-type phase are slightly shifting to lower angles due to thermal expansion (see e.g. the blue and cyan diffractograms at 204 and 286 °C, Figure 4.11b). For the β -Mn-type Co-Re NPs, the calculated linear thermal expansion coefficient in the temperature range of 100 – 250 °C is 25 × 10⁻⁶ °C⁻¹. Upon further heating, the NPs transform into a hexagonal close-packed (hcp) phase at around 300 °C (green and red diffractograms in Figure 4,11b). This phase transformation is in good agreement with reports on Co NPs.[30,39]

The sharp Bragg reflections of the hcp-type phase (red diffractogram at 349 °C, Figure 4.11b) clearly show that a complete recrystallization and particle growth process has taken place, with an estimated change from 5 to 30 nm sized crystallites (using the Scherrer equation) for the β -Mn and hcp-type phases, respectively. The calculated unit cell dimensions of the hcp-type phase at 349 °C are a=0.2516 nm and c=0.4095 nm. When using the thermal expansion coefficients of hcp Co (linear coefficients along the a and c axes; 12.5×10^{-6} °C⁻¹ and 17.8×10^{-6} °C⁻¹),[40] these values translate into a unit cell volume of 0.01105 nm³/Co at 20 °C, which is very close to the value reported for pure hcp Co (0.01106 nm³/Co).[41]

The high-temperature SR-PXRD data hence show that a drastic Re segregation occurs. The β -Mn-type Co-Re NPs transform into pure hcp Co, and consequently a separate high-Re-content phase forms, with too small particle size or to poor crystallinity to be detected by the applied method.

4.4 Conclusion

We report on the first synthesis of crystalline Co–Re NPs. According to Rietveld refinement these NPs take the β -Mn-type structure with a distinct site preference of Re atoms in the 12-fold site. Homogeneous elemental distribution of Co and Re in the individual NPs was further demonstrated using HRTEM and STEM-EDX line scans. The synthesized Co–Re NPs form a solid solution up to a maximum of

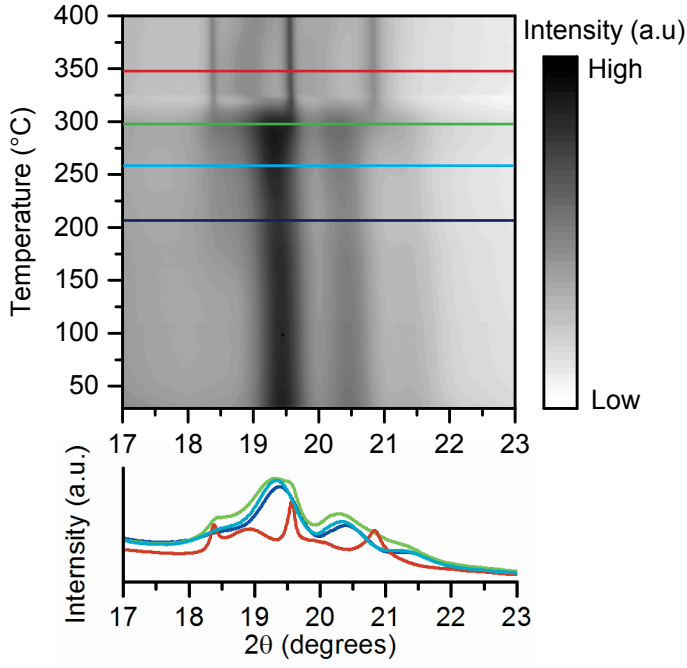


Figure 4.11. *In situ* synchrotron high temperature treatment of $Co_{0.85}Re_{0.15}$ NPs. (a) SR-PXRD contour plot upon heating in 4 vol. % H_2 /He from 27 to 400 °C at a rate of 2 °C min⁻¹. (b) Selected 2D SR-PXRD patterns corresponding to the colored lines in (a). Blue = 204 °C, cyan = 256 °C, green = 298 °C, red = 349 °C. λ = 0.06957 nm.

~15 atom % Re. The thermal stability of the Co–Re NPs was explored in reducing atmosphere. The β -Mn polymorph is stable up to 300 °C, which defines the maximum operational temperature for this type of Co–Re NPs, a parameter of immense importance when utilized as nano-catalysts for industrial applications.

As the β -Mn-type Co–Re NPs are currently synthesized for the first time, their catalytic potential has not yet been explored. Although Co-containing Fischer-Tropsch catalysts are based on the hexagonal/cubic close-packed (hcp/ccp) Co polymorphs,[15, 42] currently no routes for controlled hcp/ccp Co–Re NPs synthesis exist. Therefore, the synthesis of β -Mn-type Co–Re NPs represents a promising possibility to obtain well-defined model catalysts.[24-28] These will be highly attractive for detailed investigations to elucidate the role of the Re promoter in the Co-based Fischer-Tropsch process. The β -Mn-type Co–Re NPs can be studied as such, or thermally converted into a hcp/ccp structure, which ought to be possible, yet is still very challenging.

References

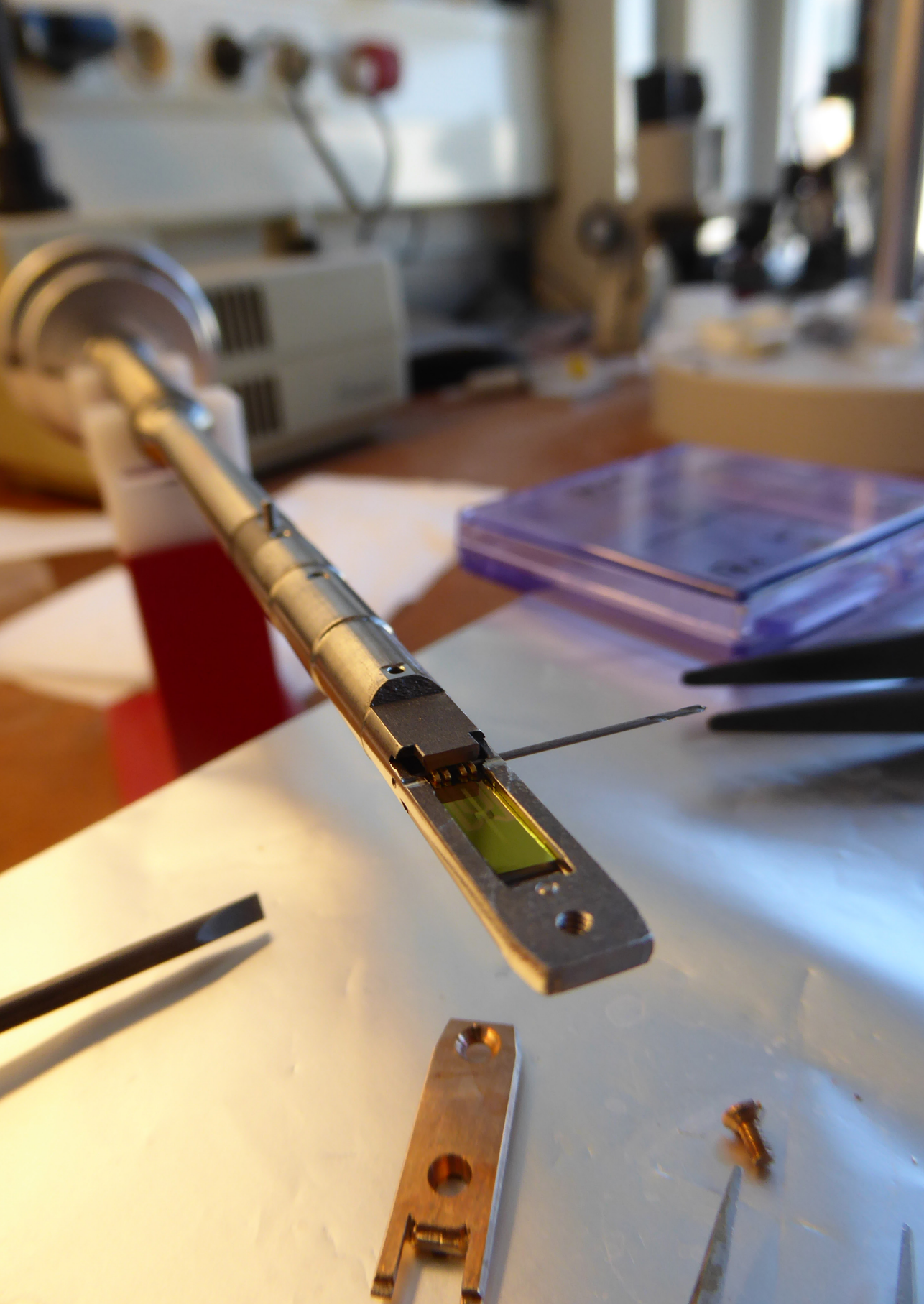
- [1] Ferrando, R.; Jellinek, J.; Johnston, R. L. Nanoalloys: From Theory to Applications of Alloy Clusters and Nanoparticles. *Chem. Rev.* **2008**, *108* (3), 845–910 DOI: 10.1021/cr040090g.
- [2] You, H.; Yang, S.; Ding, B.; Yang, H. Synthesis of Colloidal Metal and Metal Alloy Nanoparticles for Electrochemical Energy Applications. *Chem. Soc. Rev.* **2013**, 42 (7), 2880–2904 DOI: 10.1039/C2CS35319A.
- [3] Barcaro, G.; Caro, A.; Fortunelli, A. Springer Handbook of Nanomaterials; Editor: Vajtai, R.; Springer Berlin, Heidelberg, **2013**; pp 409–472 DOI: 10.1007/978-3-642-20595-8.
- [4] Gilroy, K. D.; Ruditskiy, A.; Peng, H.-C.; Qin, D.; Xia, Y. Bimetallic Nanocrystals: Syntheses, Properties, and Applications. *Chem. Rev.* **2016**, *116* (18), 10414–10472 DOI: 10.1021/acs.chemrev.6b00211.
- [5] Yan, Y.; Du, J. S.; Gilroy, K. D.; Yang, D.; Xia, Y.; Zhang, H. Intermetallic Nanocrystals: Syntheses and Catalytic Applications. *Adv. Mater.* **2017**, 29 (14), 1605997 DOI: 10.1002/adma.201605997.
- [6] Nakamula, I.; Yamanoi, Y.; Imaoka, T.; Yamamoto, K.; Nishihara, H. A Uniform Bimetallic Rhodium/Iron Nanoparticle Catalyst for the Hydrogenation of Olefins and Nitroarenes. *Angew. Chem. Int. Ed.* **2011**, *50* (26), 5830–5833 DOI: 10.1002/anie.201102836.
- [7] Zhang, S.; Metin, Ö.; Su, D.; Sun, S. Monodisperse AgPd Alloy Nanoparticles and Their Superior Catalysis for the Dehydrogenation of Formic Acid. *Angew. Chem. Int. Ed.* **2013**, 52 (13), 3681–3684 DOI: 10.1002/anie.201300276.
- [8] Xia, B. Y.; Wu, H. B.; Li, N.; Yan, Y.; Lou, X. W. D.; Wang, X. One-Pot Synthesis of Pt-Co Alloy Nanowire Assemblies with Tunable Composition and Enhanced Electrocatalytic Properties. *Angew. Chem. Int. Ed.* **2015**, *54* (12), 3797–3801 DOI: 10.1002/anie.201411544.
- [9] Alayoglu, S.; Eichhorn, B. Rh-Pt Bimetallic Catalysts: Synthesis, Characterization, and Catalysis of Core-Shell, Alloy, and Monometallic Nanoparticles. *J. Am. Chem. Soc.* **2008**, *130* (51), 17479–17486 DOI: 10.1021/ja8061425.
- [10] Singh, A. K.; Xu, Q. Synergistic Catalysis Over Bimetallic Alloy Nanoparticles. *ChemCatChem.* **2013**, *5* (3), 652–676 DOI: 10.1002/cctc.201200591.
- [11] Eri, S.; James G Goodwin, J.; Marcelin, G.; Riis, T. Catalyst for Production of Hydrocarbons. US Patent 4801573, **1989**.
- [12] Behrmann, W. C.; Arcuri, K. B.; Mauldin, C. H. Surface Supported Cobalt Catalysts, Process Utilizing These Catalysts for the Preparation of Hydrocarbons From Synthesis Gas and Process for the Preparation of Said Catalysts. US Patent 5545674, **1996**.
- [13] Espinoza, R. L.; Visagie, J. L.; Van Berge, P. J.; Bolder, F. H. Catalysts. US Patent 5733839, **1998**.
- [14] Schanke, D.; Rytter, E.; Jaer, F. O. Scale-Up of Statoil's Fischer-Tropsch Process. In Natural Gas Conversion VII, Proceedings of the 7th Natural Gas Conversion Symposium; *Stud. Surf. Sci. Catal.* **2004**, *147*, 43–48 DOI: 10.1016/S0167-2991(04)80025-9.

- [15] Tsakoumis, N. E.; Walmsley, J. C.; Rønning, M.; van Beek, W.; Rytter, E.; Holmen, A. Evaluation of Reoxidation Thresholds for γ-Al₂O₃-Supported Cobalt Catalysts Under Fischer-Tropsch Synthesis Conditions. *J. Am. Chem. Soc.* **2017**, *139* (10), *3706–3715* DOI: 10.1021/jacs.6b11872.
- [16] Kojima, R.; Aika, K.-I. Rhenium Containing Binary Catalysts for Ammonia Synthesis. *Appl. Catal. A*, **2001**, 209 (1-2), 317–325 DOI: 10.1016/S0926-860X(00)00764-X.
- [17] McAulay, K.; Hargreaves, J. S. J.; McFarlane, A. R.; Price, D. J.; Spencer, N. A.; Bion, N.; Can, F.; Richard, M.; Greer, H. F.; Zhou, W. Z. The Influence of Pre-Treatment Gas Mixture Upon the Ammonia Synthesis Activity of Co-Re Catalysts. *Catal. Comm.* **2015**, *68*, 53–57 DOI: 10.1016/j.catcom.2015.04.016.
- [18] Bazin, D.; Borko, L.; Koppány, Z.; Kovács, I.; Stefler, G.; Sajó, L. I.; Schay, Z.; Guczi, L. Re-Co/NaY and Re-Co/Al₂O₃ Bimetallic Catalysts: *In Situ* EXAFS Study and Catalytic Activity. *Catal. Lett.* **2002**, *84* (3-4), 169–182 DOI: 10.1023/A:1021423802679.
- [19] Martínez, A.; López, C.; Márquez, F.; Díaz, I. Fischer-Tropsch Synthesis of Hydrocarbons Over Mesoporous Co/SBA-15 Catalysts: the Influence of Metal Loading, Cobalt Precursor, and Promoters. *J. Catal.* **2003**, 220 (2), 486–499 DOI: 10.1016/S0021-9517(03)00289-6.
- [20] Storsæter, S.; Borg, Ø.; Blekkan, E. A.; Holmen, A. Study of the Effect of Water on Fischer–Tropsch Synthesis Over Supported Cobalt Catalysts. *J. Catal.* **2005**, 231 (2), 405–419 DOI: 10.1016/j.jcat.2005.01.036.
- [21] Voronov, A.; Tsakoumis, N. E.; Hammer, N.; van Beek, W.; Emerich, H.; Rønning, M. The State and Location of Re in Co-Re/Al₂O₃ Catalysts During Fischer-Tropsch Synthesis: Exploring High-Energy XAFS for *In Situ* Catalysts Characterisation. *Catal. Today* **2014**, 229, 23–33 DOI: 10.1016/j.cattod.2013.11.069
- [22] Jacobs, G.; Chaney, J. A.; Patterson, P. M.; Das, T. K.; Davis, B. H. Fischer–Tropsch Synthesis: Study of the Promotion of Re on the Reduction Property of Co/ Al_2O_3 Catalysts by *In Situ* EXAFS/XANES of Co K and Re L_{III} Edges and XPS. *Appl. Catal. A*, **2004**, 264 (2), 203–212 DOI: 10.1016/j.apcata.2003.12.049
- [23] Bakken, V.; Bergene, E.; Rytter, E.; Swang, O. Bimetallic Cobalt/Rhenium Systems: Preferred Position of Rhenium Through an Interdisciplinary Approach. *Catal. Lett.* **2010**, 135 (1-2), 21–25 DOI: 10.1007/s10562-009-0089-6.
- [24] Somorjai, G. A.; Park, J. Y. Molecular Factors of Catalytic Selectivity. *Angew. Chem. Int. Ed.* **2008**, 47 (48), 9212–9228 DOI: 10.1002/anie.200803181.
- [25] Jürgens, B.; Borchert, H.; Ahrenstorf, K.; Sonström, P.; Pretorius, A.; Schowalter, M.; Gries, K.; Zielasek, V.; Rosenauer, A.; Weller, H.; et al. Colloidally Prepared Nanoparticles for the Synthesis of Structurally Well-Defined and Highly Active Heterogeneous Catalysts. *Angew. Chem. Int. Ed.* **2008**, *47* (46), 8946–8949 DOI: 10.1002/anie.200802188.
- [26] Jia, C.-J.; Schüth, F. Colloidal Metal Nanoparticles as a Component of Designed Catalyst. *Phys. Chem. Chem. Phys.* **2011**, 13 (7), 2457–2487 DOI: 10.1039/c0cp02680h.
- [27] An, K.; Somorjai, G. A. Size and Shape Control of Metal Nanoparticles for Reaction Selectivity in Catalysis. *ChemCatChem*, **2012**, 4 (10), 1512–1524 DOI: 10.1002/

- cctc.201200229.
- [28] Na, K.; Zhang, Q.; Somorjai, G. A. Colloidal Metal Nanocatalysts: Synthesis, Characterization, and Catalytic Applications. *J. Clust. Sci.* **2014**, 25 (1), 83–114 DOI: 10.1007/s10876-013-0636-6.
- [29] Dinega, D. P.; Bawendi, M. G. A Solution-Phase Chemical Approach to a New Crystal Structure of Cobalt. *Angew. Chem. Int. Ed.* **1999**, *38* (12), 1788–1791 DOI: 10.1002/(SICI)1521-3773(19990614)38:12<1788::AID-ANIE1788>3.0.CO;2-2.
- [30] Sun, S.; Murray, C. B. Synthesis of Monodisperse Cobalt Nanocrystals and Their Assembly Into Magnetic Superlattices (Invited). *J. Appl. Phys.* **1999**, *85* (8), 4325 DOI: 10.1063/1.370357.
- [31] Zacharaki, E.; Kalyva, M.; Fjellvåg, H.; Sjåstad, A. O. Burst Nucleation by Hot Injection for Size Controlled Synthesis of ε-Cobalt Nanoparticles. *Chem. Cent. J.* **2016**, *10* (1), 10 DOI: 10.1186/s13065-016-0156-1.
- [32] Dyadkin, V.; Pattison, P.; Dmitriev, V.; Chernyshov, D. A New Multipurpose Diffractometer PILATUS@SNBL. *J. Synchrotron Rad.* **2016**, 23 (Pt 3), 825–829 DOI: 10.1107/S1600577516002411.
- [33] Rodríguez-Carvajal, J. Recent Advances in Magnetic Structure Determination by Neutron Powder Diffraction. *Phys. B (Amsterdam, Neth.)* **1993**, 192 (1-2), 55–69 DOI: 10.1016/0921-4526(93)90108-I.
- [34] Miyakawa, M.; Umetsu, R. Y.; Ohta, M.; Fujita, A.; Fukamichi, K.; Hori, T. Spin Fluctuation, Thermal Expansion Anomaly, and Pressure Effects on the Néel Temperature of β -MnM (M = Ru, Os, and Ir) Alloys. *Phys. Rev. B* **2005**, 72 (5), 054420 DOI: 10.1103/PhysRevB.72.054420.
- [35] Karlsen, O. B.; Kjekshus, A.; Fjellvåg, H.; Ravindran, P.; Vidya, R.; Hauback, B. C. Structure and Magnetism of the β-Mn–Co Solid-Solution Phase. *J. Alloys Compd.* **2009**, *476* (1-2), 9–13 DOI: 10.1016/j.jallcom.2008.09.011.
- [36] Xie, W.; Thimmaiah, S.; Lamsal, J.; Liu, J.; Heitmann, T. W.; Quirinale, D.; Goldman, A. I.; Pecharsky, V.; Miller, G. J. β -Mn-Type $Co_{(8+x)}Zn_{(12-x)}$ As a Defect Cubic Laves Phase: Site Preferences, Magnetism, and Electronic Structure. *Inorg. Chem.* **2013**, 52 (16), 9399–9408 DOI: 10.1021/ic4009653.
- [37] Vavilova, V. V.; Galkin, L. N.; Glazov, M. V. Metastable Phase Formation Rules in Rhenium Based Alloys of Re-M System (M-Nb,Ta,Mo,W) During Fast Quenching. *Neorg. Mater.* **1991**, 27, 2119–2123.
- [38] Vegard, L. Die Konstitution Der Mischkristalle Und Die Raumfüllung Der Atome. Z. Physik. **1921**, 5 (1), 17–26 DOI: 10.1007/BF01349680.
- [39] Denton, A.; Ashcroft, N. Vegard's Law. *Phys. Rev. A* **1991**, 43 (6), 3161–3164 DOI: 10.1103/PhysRevA.43.3161.
- [40] Green, M. Organometallic Based Strategies for Metal Nanocrystal Synthesis. *Chem. Commun. (Camb.)* **2005**, 24, 3002–3011 DOI: 10.1039/b501835h.
- [41] Kasamatsu, Y.; Koyama, M.; Masumoto, K.-I.; Kojima, K.-I.; Hihara, T.; Kamigaichi, T. Dilatometric Measurement of the Thermal Expansion of Cobalt Single Crystal. *Jpn. J. Appl. Phys.* **1981**, 20 (1), 37–40 DOI: 10.1143/JJAP.20.37.
- [42] Masumoto, H.; Watanabe, K.; Inagawa, K. O. N. Magnetic Properties of Hexagonal Close-Packed Structure Type Co-Ir Binary Alloys. *Trans. JIM* **1976**, 17 (9),

592-595 DOI: 10.2320/matertrans1960.17.592.

[43] Price, S. W. T.; Martin, D. J.; Parsons, A. D.; Sławiński, W. A.; Vamvakeros, A.; Keylock, S. J.; Beale, A. M.; Mosselmans, J. F. W. Chemical Imaging of Fischer-Tropsch Catalysts Under Operating Conditions. *Sci. Adv.* **2017**, *3* (3), e1602838 DOI: 10.1126/sciadv.1602838.



CHAPTER 5

In situ TEM observation of the Boudouard reaction: multi-layered graphene formation from CO on cobalt nanoparticles at atmospheric pressure

Using a MEMS nanoreactor in combination with a specially designed *in situ* TEM holder and gas supply system, we imaged the formation of multiple layers of graphene encapsulating a cobalt nanoparticle, at 1 bar CO : N_2 (1 : 1) and 500 °C. The cobalt nanoparticle was imaged live in a TEM during the Boudouard reaction. The *in situ*/operando TEM studies give insight into the behavior of the catalyst at the nanometer-scale, under industrially relevant conditions. When switching from Fischer–Tropsch syngas conditions (CO : N_2 1 : 2 : 3 at 1 bar) to CO-rich conditions (CO : N_2 1 : 1 at 1 bar), we observed the formation of multi-layered graphene on Co nanoparticles at 500 °C. Due to the high temperature, the surface of the Co nanoparticles facilitated the Boudouard reaction, causing CO dissociation and the formation of layers of graphene. After the formation of the first patches of graphene at the surface of the nanoparticle, more and more layers grew over the course of about 40 minutes. In its final state, around 10 layers of carbon capped the nanoparticle. During this process, the carbon shell caused mechanical stress in the nanoparticle, inducing permanent deformation.

5.1 Introduction

Novel techniques and equipment to allow *in situ* and operando research on catalytic samples are currently under development. Using these tools, it is possible to investigate a catalyst under industrially relevant working conditions: high temperatures and high gas pressures. The so-called temperature and pressure gaps between traditional catalysis research and the industrial applications are thereby bridged, improving the relevance of the results obtained via *in situ* research.

Current demand for clean, renewable fuels has instigated interest in the well-known catalytic Fischer–Tropsch (FT) reaction, which produces hydrocarbons from synthesis gas (syngas, CO and H₂).[1] One of the catalysts frequently used for this reaction is cobalt, often in the form of supported nanoparticles.[2] Both in academia as well as industry, efforts are being undertaken to investigate this catalytic system, in order to understand the fundamental processes involved and eventually improve the performance of the catalyst.

Several research groups have used *in situ* techniques to explore the FT syngas reaction on cobalt, e.g. scanning tunneling microscopy (STM),[3–5] X-ray diffraction (XRD),[6] and X-ray absorption spectroscopy (XAS),[7,8] yielding meaningful insight into the working state of the catalyst surface under industrially relevant conditions. However, the use of *in situ* transmission electron microscopy (TEM) has not yet been reported. As has been shown for other reactions, such as the catalytic CO oxidation on platinum nanoparticles,[9] and the formation of solid carbon in various forms on metal nanoparticles,[10-13] *in situ* TEM experiments can reveal valuable information of the behavior of the catalyst nanoparticles at the atomic scale.

To investigate the behavior of FT catalysts at elevated pressures and temperatures in a TEM, we used a combination of a MEMS nanoreactor loaded with Co nanoparticles, inserted in a specially designed *in situ* TEM sample holder. The sample holder allowed us to heat the sample (up to 660 °C) while using a gas supply system to flow a mixture of reactant gases over the sample at ambient pressure. A residual gas analyzer (RGA) monitored the product gas stream leaving the outlet of the nanoreactor.

5.2 Experimental

5.2.1 Cobalt nanoparticles

ε-Cobalt nanoparticles (NPs) were synthesized under inert conditions via hot injection methodology using standard procedures.[14] Oleic acid (OA, $C_{18}H_{34}O_{27} \ge 99\%$, 0.07 g) in 1,2-dichlorobenzene (DCB, $C_6H_4C_{127}$, 99%, anhydrous, 15 mL) was heated to 170 °C under stirring, and 0.52 g of dicobalt octacarbonyl (Co₂(CO)₈₇ ≥90% Co) dissolved in 3 mL of DCB was rapidly injected. The black colloidal suspension, formed upon injection, was aged at 170 °C for 30 min before quenching with 10 mL of DCB. The NPs were flocculated with excess 2-propanol (C_3H_8O , 99.5%, anhydrous) and isolated by centrifugation. After discarding the supernatant, the NP precipitate was purified by three repetitive cycles of washing in 2-propanol and subsequent centrifugation. The ε-Co NPs dispersed in hexane (C_6H_{147} , 95%, anhydrous) were stored in a closed container in a glovebox to prevent oxidation. All reagents were supplied by Aldrich, and used without further purification.

For reference TEM imaging, a few drops of nanoparticle suspension were placed on a 400 mesh copper TEM grid coated with lacey carbon film, covered with a continuous, ultrathin (<3 nm) carbon film (Ted Pella Inc.). The solvent was left to evaporate inside the glovebox, by heating the TEM grid on a hotplate overnight at 100 °C.

5.2.2 Nanoreactors

In situ TEM experiments were conducted using the latest version of nanoreactors (Else Kooi Laboratory).[15] These micro-electromechanical systems (MEMS) devices are fully integrated on a single silicon die.[16] The nanoreactors, shown in Figure 5.1, consist of a 4.5 μm deep, etched channel with an in- and outlet allowing sample loading and gas flow feeding. For heating, a platinum wire is integrated in the top part of the gas channel. This wire allows simultaneous heating and temperature readout via a calibrated resistance measurement. The construction of the channel is such that it is possible to go up to 14 bar and 660 °C. A set of 41 electron-transparent windows, consisting of 15 nm thin amorphous SiN films, is embedded in the center of the channel. The thin and chemically inert amorphous silicon nitride film also covers all internal surfaces of the nanoreactor channel. The channel is supported by pillars, to increase stiffness and reduce bulging effects when filled with gas. After the preparation of the channel, the holes used for deposition and etching are plugged.

Cobalt nanoparticles were loaded into the nanoreactor by drop-casting the suspension containing the sample on the inlet.[17] Capillary forces drew the liquid through the channel, depositing nanoparticles on all surfaces, including the electron-transparent windows. The loading was done in a glovebox, under Ar atmosphere. Subsequently, the loaded nanoreactors were stored in an airtight vessel, which was taken out of the glovebox. The vessel was gently heated to $\sim\!80\,^{\circ}\mathrm{C}$ on a hotplate for two days, while a turbomolecular pump was connected to pump down the vessel in order to evaporate the solvent.

5.2.3 In situ TEM holder

The custom built, dedicated *in situ* TEM holder used for the experiments, as shown in Figure 5.2, contains a pair of capillaries for gas feed and exhaust. The nanoreactors

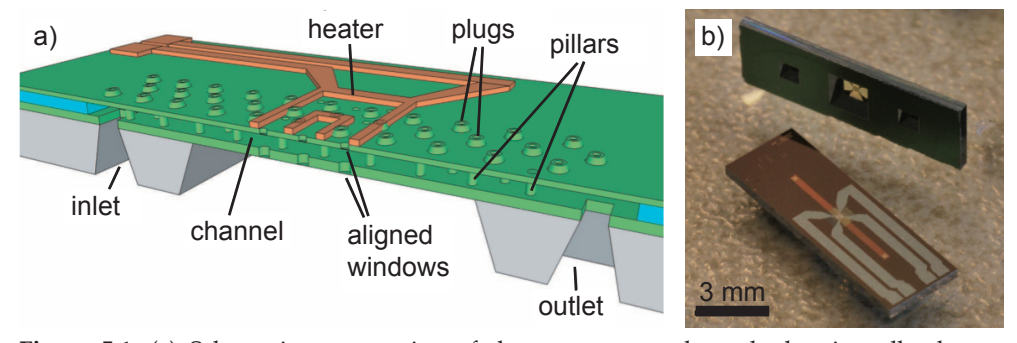


Figure 5.1. (a) Schematic cross-section of the nanoreactor channel, showing all relevant components.[10] (b) Photograph of two identical nanoreactors: the top one, viewed sideways, shows the bottom side with the channel inlet and outlet, and the bottom one, placed flat, shows the top side with the gas channel and heater wire.

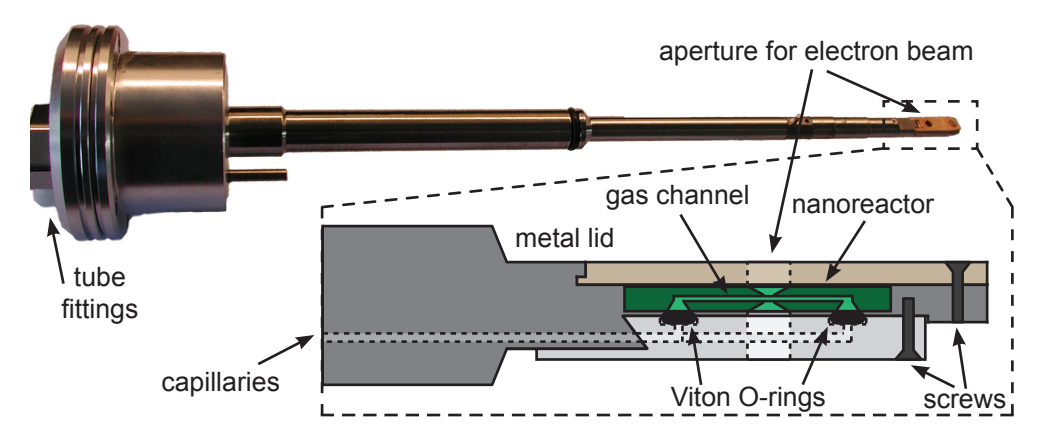


Figure 5.2. Schematic overview the in situ TEM holder.

were placed and pressed on top of two Viton O-rings to ensure a leak-tight connection between the nanoreactor gas-channel and the capillaries. For controlling and reading out the temperature of the nanoreactor, four pins (two for control, two for read-out) were placed in contact with the platinum heating wire. Custom-built software digitally controlled and monitored the temperature of the sample.[18]

5.2.4 Gas supply system and residual gas analysis

Reactant gases were supplied by a computer controlled gas flow system (Leiden Probe Microscopy BV).[19] A schematic overview of the system is shown in Figure 5.3.

Reactant gases (Praxair, purity: O₂ - 6.0; H₂ - 6.0; CO - 4.7) were introduced into the system via standard pressure reducing valves. The flow of each gas was controlled by Mass Flow Controllers (MFCs, Bronkhorst) and the desired mixture was obtained via a rotating mixing valve. Carrier gas (Linde Gas, N, purity: 6.0) was added to the gas mixture to create a typical total flow of ~5 mL, min⁻¹. The pressure in the main gas line was regulated by a Back Pressure Controller (BPC, Bronkhorst) 'TEM holder', and the exhaust of the system was pumped by a diaphragm pump. To direct a portion of the gas mixture to the *in situ* holder, a T-piece was placed before the BPC, connected to the inlet of the holder. The capillaries directly connected to the in situ TEM holder were made of PEEK (poly ether ether ketone, a non-conducting material) to ensure electrical insulation of the holder when inserted into the TEM compustage. Vibration isolation was implemented by clamping the PEEK capillaries in-between two heavy metal slabs, reducing the mechanical noise introduced by the pumps running continuously. The exhaust capillary of the *in situ* TEM holder was directly connected to a turbomolecular pump. This setup established a pressure difference between the inlet and the exhaust of the holder, resulting in gas flowing through the narrow nanoreactor channel. The pressure inside the nanoreactor channel was defined as half of the pressure that was established by the 'TEM holder BPC' at the T-piece of the inlet side of the holder, due to the symmetry of the holder and the nanoreactor. For residual gas analysis, a quadrupole mass spectrometer (QMS, Pfeiffer Vacuum QMA-200) was connected to the exhaust line. Before entering the gas system, CO gas was led through a 'carbonyl trap' consisting of a copper tube

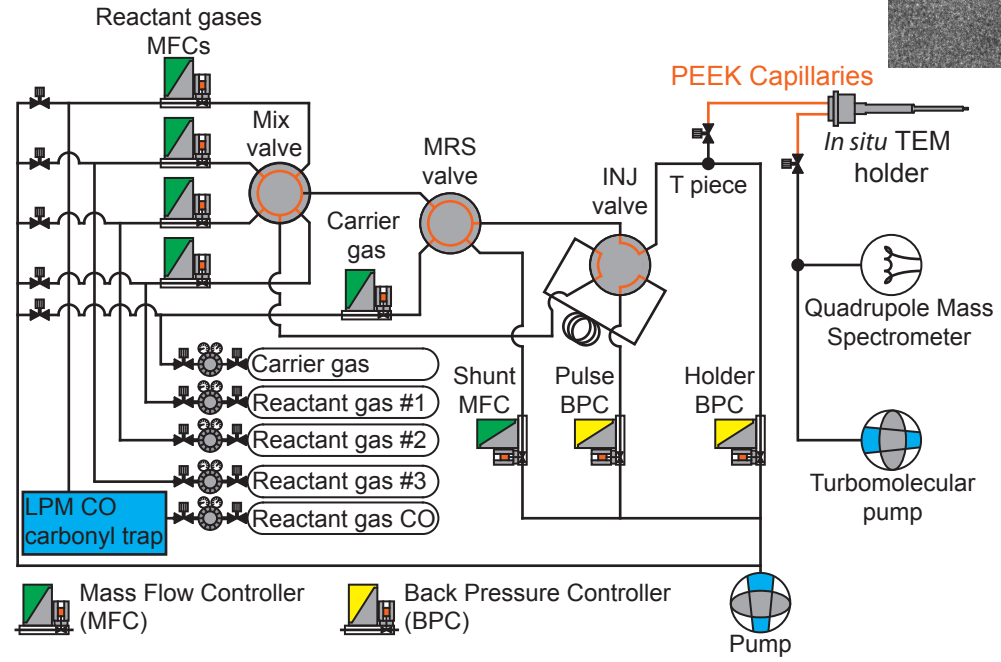


Figure 5.3. Schematic overview of the gas supply system, showing the computer operated Mass Flow Controllers (MFCs), Back Pressure Controllers (BPCs), and rotating mixing valves.

heated to 325 °C and filled with copper-shot. This was done to decompose and remove any metal carbonyls from the gas, as nickel tetracarbonyl (Ni(CO)₄) and iron pentacarbonyl (Fe(CO)₅) can be formed in the gas when CO is stored in or passed through steel containers at high pressure (e.g. during the production of the gas).[20–22] Using Spacetime software the data profiles from the gas supply system, QMS and nanoreactor temperature were synchronized and analyzed.[23]

5.2.5 Transmission Electron Microscopy

The TEM used for the in situ experiments was a C_s -corrected FEI Titan $_3$ 80-300 operated at 300 kV. Images were captured using a Digital Electronic camera (DE-12) with 6.0 mm pixel size and 4096 x 3072 pixels. To minimize beam effects on the sample, the electron intensity was kept below 500 electrons per Å 2 per s during the *in situ* experiments. An exposure time of 1 s was used for image acquisition.

Reference images of the cobalt nanoparticles under vacuum were acquired on an FEI monochromated Tecnai F20ST/STEM electron microscope, equipped with a Gatan Ultrascan CCD camera (4k 4k). This TEM was operated at 200 keV.

Resulting images were analyzed using Digital Micrograph 3 and Fiji software.

5.3 Results and discussion

5.3.1 Nanoparticle preparation

Cobalt nanoparticles were initially imaged on a carbon grid to obtain reference data. Figure 5.4 shows a representative micrograph of a free-standing nanoparticle on

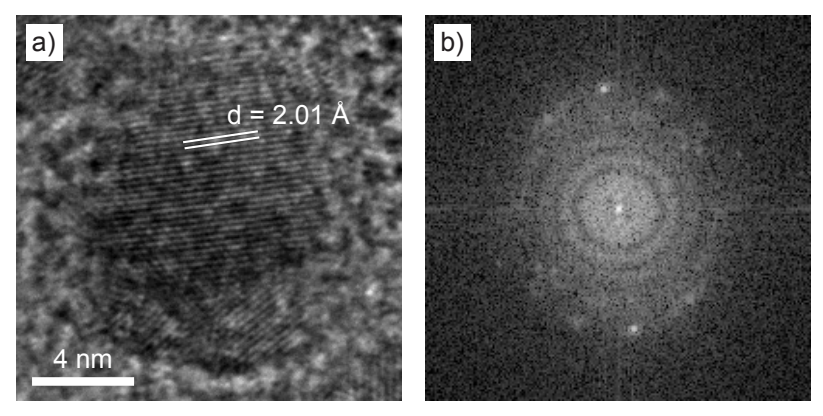


Figure 5.4. (a) ε-Co nanoparticle on carbon film, showing the lattice fringes corresponding to the (221) lattice plane. (b) FFT of the image.

carbon film. The lattice fringes with a d-spacing of 2.01 Å (Figure 5.4a) correspond to the (221) lattice plane of ε -Co (space group $p4_132$).[24] The FFT shows the two bright spots corresponding to the (221) lattice planes.

For the *in situ* experiments, a nanoreactor was loaded with a suspension containing cobalt nanoparticles. Prior to the Boudouard reaction, the sample was exposed to various conditions in order to conduct different experiments. The gas feed profile, QMS analyzer data and temperature course of the whole experiment are shown in Figure 5.5.

Initially, residual organic oleic acid (OA) molecules were removed in situ by heating the cobalt nanoparticles under a flow of N_2 , at 1 bar and 300 °C, for 90 minutes. A micrograph of a nanoparticle on the amorphous SiN window of the nanoreactor, obtained after the heating procedure, is shown in Figure 5.6.

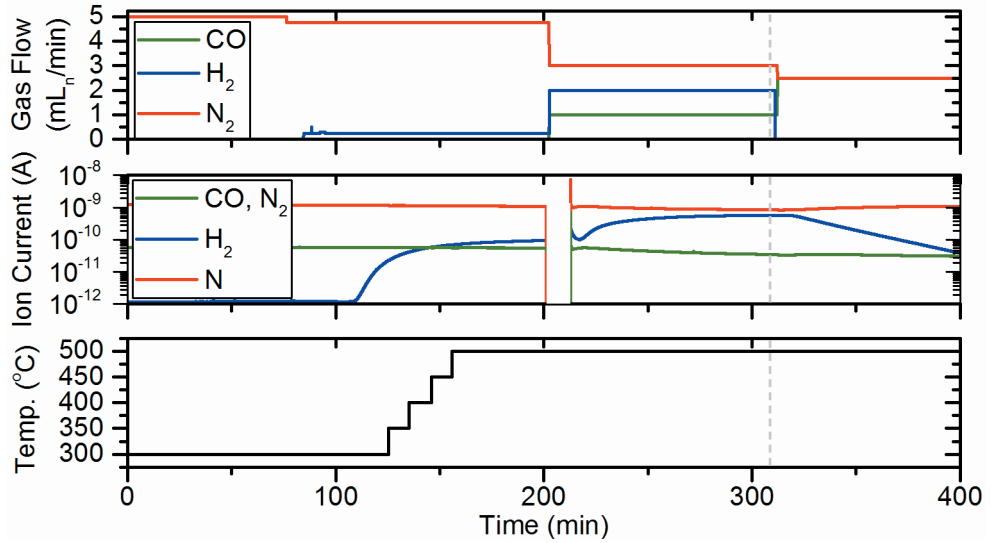


Figure 5.5. Gas feed profile (top), QMS analyzer data (middle), and nanoreactor temperature course (bottom) during the experiment. t = 0 is indicated by the vertical dashed line.

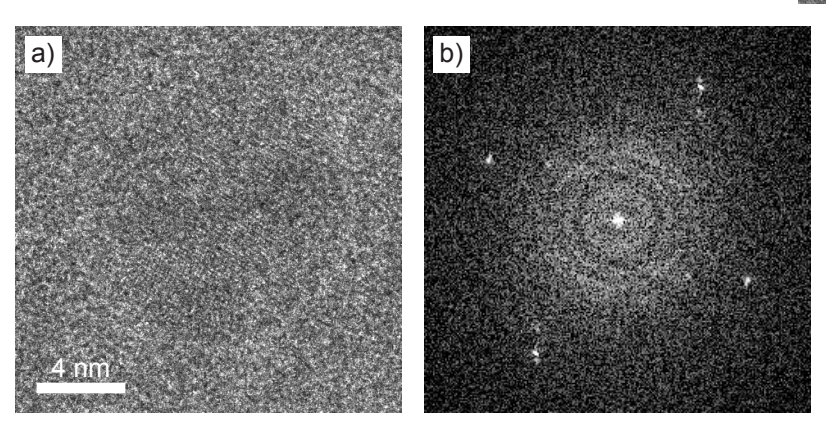


Figure 5.6. (a) Cobalt nanoparticle inside the nanoreactor, at 1 bar N_2 and 300 $^{\circ}$ C. (b) FFT of the image.

To reduce any oxides that might have formed (although we did not observe any oxide in the TEM images), and to further reduce the amount of OA, the nanoreactor was then flushed with 5% $\rm H_2$ in $\rm N_2$. While flushing, the temperature was increased from 300 °C to 500 °C in 30 minutes, using increments of 50 °C, and was kept at 500 °C for the rest of the experiment. During this treatment, the nanoparticles appeared to stay in the metallic state, meaning that no oxides or carbon had formed, however we cannot exclude residues of OA remaining on the nanoparticle surface. The ϵ -Co phase transforms irreversibly during annealing in a non-oxidative environment to hexagonal close packing (hcp) at ~300 °C, and cubic close packing (ccp) at ~500 °C.[25]

After this reduction step, the metallic nanoparticles were exposed to Fischer–Tropsch syngas conditions. First, the valve to the TEM holder was closed and a mixture of CO: $\rm H_2$: $\rm N_2$ (1:2:3) at 1 bar was prepared in the lines of the gas system. The closing of the valve is visible in Figure 5.5b by the sudden dip in the QMS signal, at ~200 min. When the reactant mixture was ready, the TEM holder valve was opened again and the gas flow entered the nanoreactor. These conditions were maintained for ~100 minutes.

Finally, the feed of H_2 was removed and the gas feed mixture was adjusted to $CO:N_2$ (1:1) at 1 bar, while the sample temperature was kept at 500 °C. For clarity and ease of further discussion, the moment of closing the H_2 feed is defined as t = 0, as shown by the vertical dashed line in Figure 5.5. The residual H_2 keeps flowing through the nanoreactor, until after six minutes the H_2 signal in the QMS chamber starts to decrease (Figure 5.5b).

5.3.2 Carbon deposition

Four minutes after closing the H_2 flow, the first deposition of carbon appeared at the surface of the nanoparticle, as shown in Figure 5.7. On the surface of the clean nanoparticle imaged at t = 4:02 minutes (Figure 5.7a), the first carbon patch appeared at the top left of the nanoparticle at t = 4:10 (Figure 5.7b, indicated by the white

arrow). Then, three seconds later at t = 4:13, a second patch of carbon appeared on the surface at the top right of the nanoparticle (Figure 5.7c, indicated by the white arrow). The carbon patches continued to grow laterally, and at t = 4:47 the patches joined each other and formed a continuous layer, showing a light grey fringe on top of the nanoparticle (Figure 5.7d). After the first layer was formed, a second layer started to form, again at the top right (Figure 5.7e). The layer continued to grow and a full second carbon layer was visible at t = 20:48 (Figure 5.7f). At t = 24:03 a total of seven layers of carbon had formed on top of the particle (Figure 5.7g). The layers continued to grow laterally, thereby capping the nanoparticle, as was visible at t = 28:53 (Figure 5.7h). During the next 10 minutes, more carbon layers formed (Figure 5.7i) until the nanoparticle reached its final state at t = 39:10 (Figure 5.7j), covered in about 10 layers of carbon. After this, the nanoparticle was monitored for about 10 more minutes, but no additional carbon was deposited.

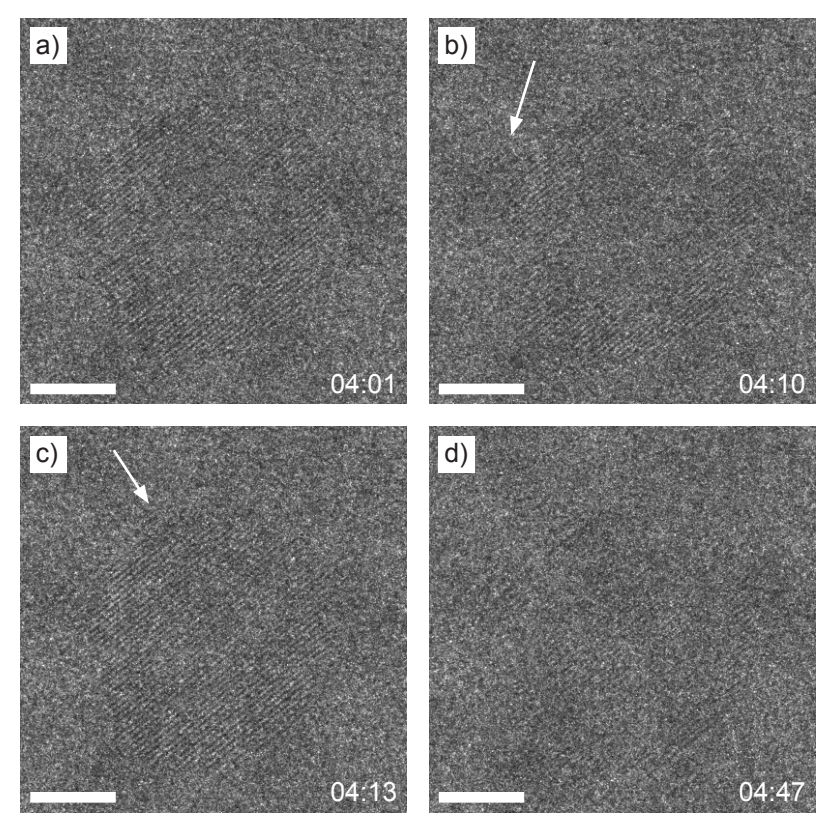
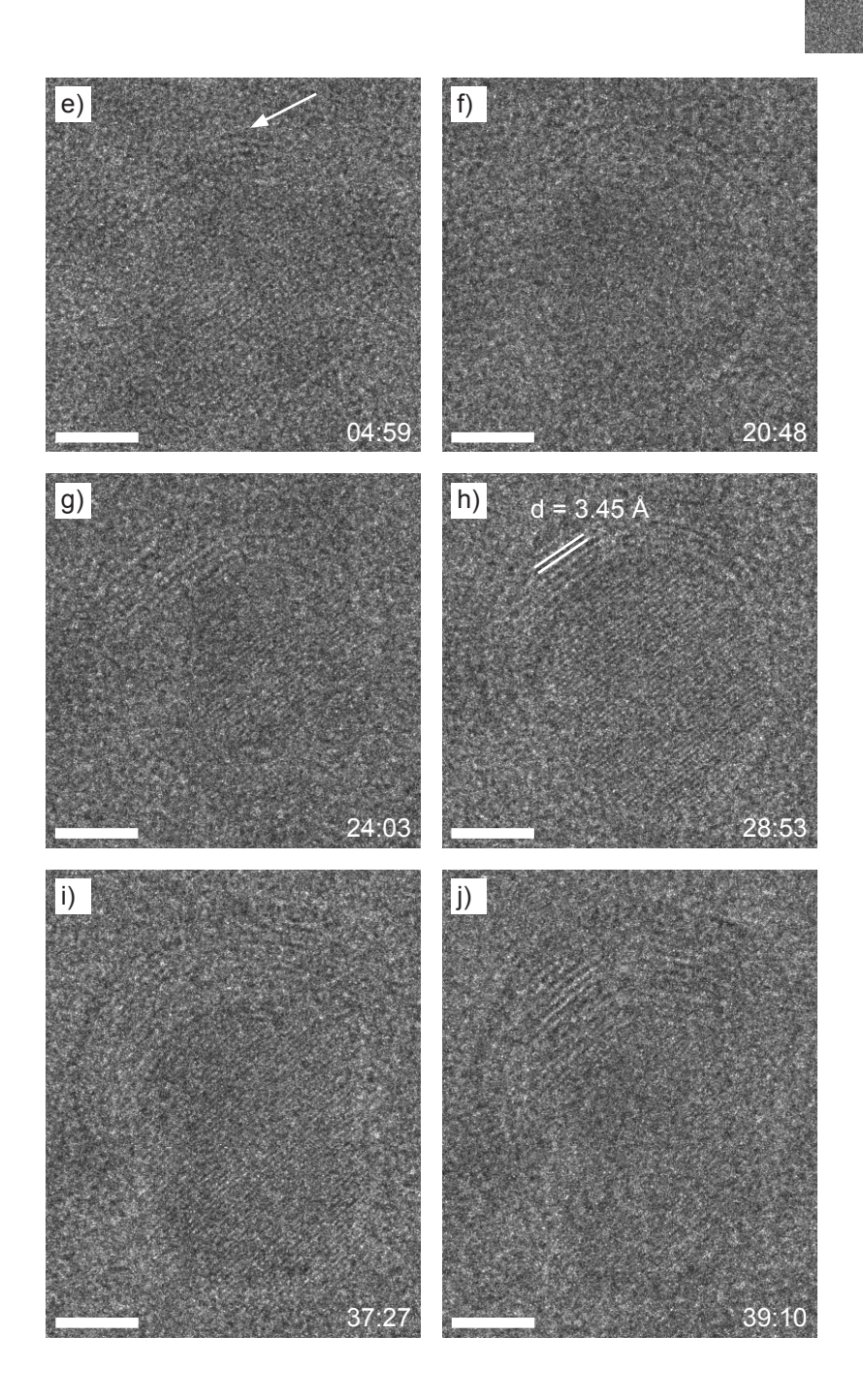


Figure 5.7. Carbon deposition process on a cobalt nanoparticle at $500\,^{\circ}\text{C}$ and 1 bar CO:N_2 (1:1). An initially fresh nanoparticle (a) was covered by patches of carbon ((b) and (c), indicated by the white arrows) that then grew laterally and formed a first layer (d). A second layer formed ((e), indicated by the white arrow) and capped the nanoparticle (f). More carbon layers grew (g-i) until after 39 minutes the nanoparticle ended up it its final state (j), covered by around 10 layers of carbon. On each micrograph, the time since shutting off the H_2 feed is indicated in minutes:seconds.



The first carbon patches were formed at two sides of the nanoparticle surface (Figure 5.6b and 5.6c, white arrows). The deposition of carbon could originate from either the dissociation of adsorbed CO molecules (eqn. (1)) or via the Boudouard disproportionation reaction (eqn. (2)).[26,27]

$$\begin{array}{c}
\text{CO}_{\text{ads}} \to \text{C}_{\text{s}} + \text{O}_{\text{ads}} \\
2 \text{ CO}_{\text{ads}} \to \text{CO}_{2 \text{ g}} + \text{C}_{\text{s}}
\end{array} \tag{1}$$

Both reactions yield solid carbon at metal surfaces, but CO adsorption followed by dissociation occurs at temperatures up to around 400 °C, while the Boudouard reaction is facilitated at cobalt surfaces above 427 °C.[26,27] Also, CO dissociation on cobalt leads to the formation of a single layer of carbidic carbon, while the Boudouard reaction can form multiple layers of graphitic carbon,[26] which is what we observed in our experiment. The carbon–carbon interlayer distance of the carbon layers formed on our nanoparticles is 3.45 Å (Figure 5.7h) indicating that graphitic carbon was indeed formed.[28] We thus conclude that we have visualized the Boudouard reaction. Further evidence for assigning the Boudouard reaction as the cause for the observed carbon deposition could be embedded in the QMS signal, as the CO_2 signal should rise as an effect of the formation of CO_2 and C from CO. However, due to high background signals it was not possible during this experiment to draw any conclusions based on the QMS data.

The process of the formation of a new carbon layer, as shown in Figure 5.8, was captured from t = 28:15. At this moment, there were nine carbon layers capping the

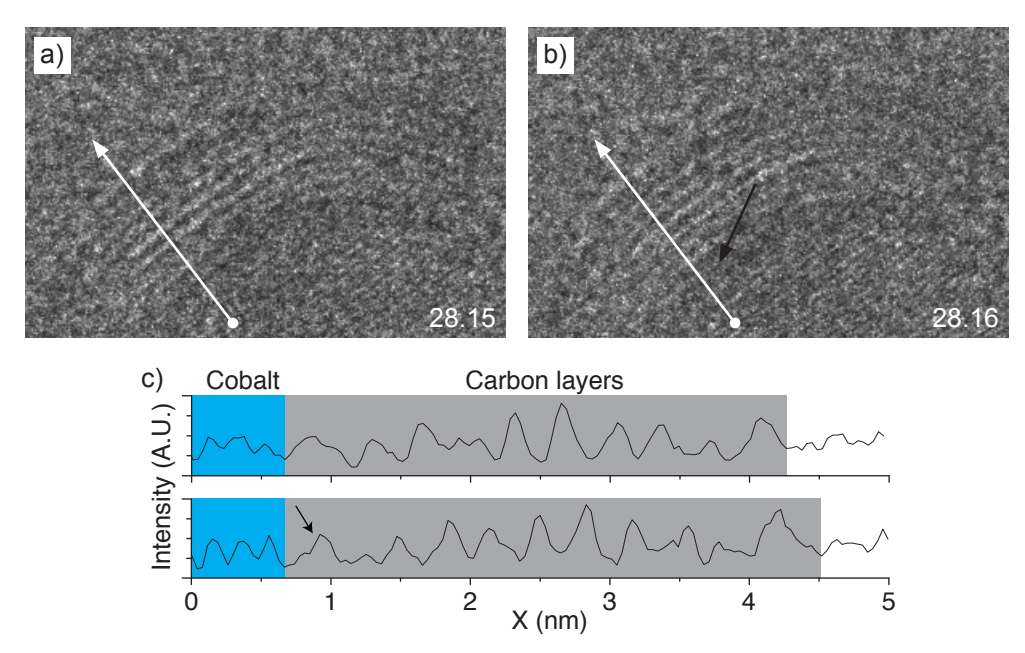


Figure 5.8. Growth of a new carbon layer, indicated by the black arrows, interlayered between the cobalt surface and the set of carbon layers capping the nanoparticle, before (a) and after (b) the formation. Profiles of the white lines are shown in (c). Top profile: image (a); bottom profile: image (b). White line length is 5 nm.

cobalt nanoparticle. The next second, at t = 28:16, it was visible that the ensemble of nine layers was pushed up by a few Ångström. A new fringe appeared at the interlayer between the cobalt surface and the packet of

carbon layers, indicating the formation of a new carbon layer. The new fringe is indicated by the black arrow in Figure 5.8b. To facilitate interpretation of the weak contrast, a white arrow was drawn perpendicular to the visible *d*-spacing on the nanoparticle and the packet of carbon layers at the exact same positions in Figures 5.8a and 5.8b. Contrast line profiles were obtained for both images, shown in Figure 5.8c.

By identifying the cobalt fringes (Figure 5.8c, blue region, *d*-spacing 2.07 Å) and the carbon fringes (Figure 5.8c, grey region, *d*-spacing 3.45 Å), it is clearly visible that the additional peak displaces the earlier formed carbon layers away from the cobalt nanoparticle surface, and the grey area expands by one lattice spacing of the carbon.

5.3.3 Effect on the nanoparticles

During the live observation of the growing layers, the nanoparticle was changing morphology. The initially spherical nanoparticle (Figure 5.7a) became elongated at the end of the carbon deposition process (Figure 5.7j). When the nanoparticle was covered with six carbon layers, the internal crystal structure was also temporarily altered, as shown in Figure 5.9. At t=25:26, the nanoparticle was still spherical (Figure 5.9a), showing a uniform crystal structure. During the following ten seconds, the crystal structure shifted around and eventually a twin boundary was formed at t=25:35 (Figure 5.9b) in the center of the nanoparticle. The crystal structure in the bottom right part of the nanoparticle continued showing mobility, and a second twin boundary appeared clearly at t=25:57 (Figure 5.9c). This situation was maintained for about 90 seconds. During that time the twin boundaries continuously shifted up and down several atomic rows. The top of the particle also showed a twin boundary for a few seconds, which was too mobile to be imaged clearly. After this period of twinning, the crystal structure of the nanoparticle became uniform again at t=27:34 (Figure 5.9d), which lasted until the end of the experiment.

The presence of twin boundaries is related to the amount of stress inside the nanoparticle, as the formation of boundaries leads to the release of this stress [29] and is known to occur in metallic nanoparticles.[30-32] Metallic nanoparticles (e.g. Au, Co) encaged by carbon shells will eventually deform when heated to a temperature above 300 °C and irradiated with a TEM electron beam, as the electron beam displaces carbon atoms in the carbon shells, causing the shells to shrink. [33-35] Similar deformation effects have been observed when carbon nanotubes were formed via CH, decomposition on the surface of Ni nanoparticles.[10] Our experiment showed a combination of both effects, as we initially started with uniform, crystalline nanoparticles, not covered by any graphite layers. Eventually, the growing carbon layers were capping just the top half of the nanoparticle. Due to continuous electron irradiation, the carbon must have been contracting and thereby compressing the capped particle. The formed strain was relieved by the formation of the twin boundaries. The initially spherical nanoparticle then deformed into an elongated shape, fitting inside the carbon cap and thereby releasing the twin boundaries to return to a uniform crystal structure.

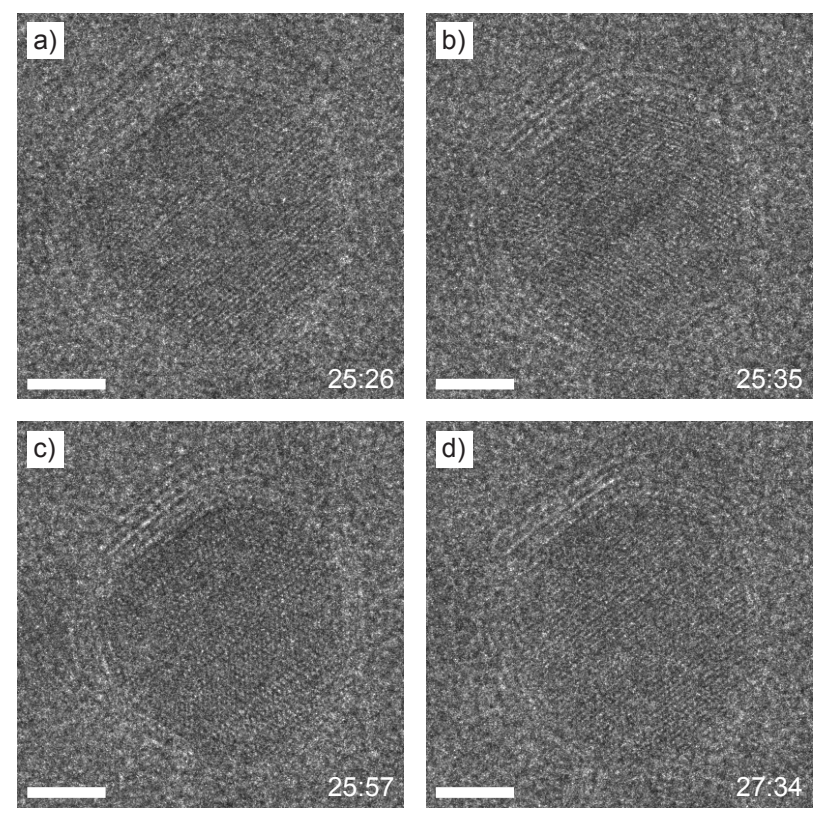


Figure 5.9. Cobalt nanoparticle, capped with six layers of carbon, initially showing a uniform crystal structure (a). A first twin boundary was formed through the center of the nano-particle (b), followed by a second twin boundary at the bottom right (c). After around 90 seconds of continuous mobility, the crystal structure relaxed into the final, uniform state (d). Scale bar is 3 nm.

5.3.4 Carbon morphologies

After continuously imaging the nanoparticle that showed the formation of the layers of carbon, other nanoparticles were imaged. Various other nanoparticles were also covered with layers of carbon, but not all of them. Around one third of all nanoparticles that were present on electron-transparent windows were encapsulated or covered with carbon. All carbon covered nanoparticles, independent of their size, supported carbon formations that consisted of around 7 to 14 layers of carbon. No trends could be established linking nanoparticle size to the number of layers. Different morphologies of carbon structures were visible: next to encapsulated nanoparticles also multi-walled carbon nanotube formations had been formed (Figure 5.10a), while other nanoparticles supported spherical structures (Figure 5.10b) that did not cap the supporting nanoparticle as tightly as the previously imaged assembly shown in Figure 5.7. As the formation of the carbon layers shown in Figure 5.10 occurred before any TEM imaging was done, we conclude that the carbon deposition is not induced by the TEM electron beam.



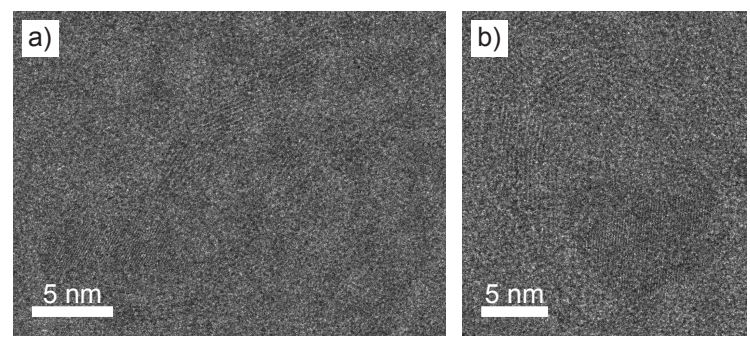


Figure 5.10. Cobalt nanoparticles supporting various shapes of carbon layers. (a) A multi-walled carbon nanotube, and (b) a spherical carbon formation loosely capping the supporting cobalt nanoparticle.

Several of the imaged particles were stable under the electron beam. However, other particles showed shape deformation processes and formation of twin boundaries while being imaged. An example of a nanoparticle that was being deformed while imaged, after being encapsulated without electron beam irradiation, is shown in Figure 5.11. When the nanoparticle was initially imaged (Figure 5.11a), the shape was already heavily elongated at t = 0.00 (when TEM imaging started). After half a minute (Figure 5.11b), the elongated particle started to slowly thin out in the center, as the carbon shape around the particle was squeezing the nanoparticle. This process slowly continued (Figure 5.11c) until finally at t = 1.19, the nanoparticle split into two separate particles (Figure 5.11d). The carbon assembly continued to deform, thereby moving the two nanoparticles around. After around three minutes the system reached its final state (Figure 5.11e).

5.4 Conclusion

We have shown the *in situ* formation of layers of graphitic carbon on free-standing cobalt nanoparticles, at 500 °C and 1 bar $\rm CO:N_2$ (1:1). The nanoparticles were imaged using TEM, with a specially designed *in situ* TEM holder and MEMS nanoreactor devices. Reactant gases were added to the nanoreactor via a gas supply system, while a QMS analyzed the product gas stream. Due to the high temperature and presence of CO gas, the Boudouard reaction led to the deposition of carbon and consequent formation of graphitic carbon on the cobalt nanoparticles.

During a 40 minute tracking period, a cobalt nanoparticle was covered and capped by layers of carbon, formed one by one at the interface of the nanoparticle surface and the carbon. The layers of carbon strained the nanoparticle. As a consequence, twin boundaries appeared until the nanoparticle was permanently deformed. Several other nanoparticles were imaged afterwards that showed similar deformation behavior.

Further measurements could provide additional evidence for the Boudouard

reaction by revealing the formation of CO_2 in the QMS data. The QMS data could also provide an indication whether all OA is fully removed from the surface of the nanoparticles, or if there is still OA present on the surface, however this is a topic for upcoming investigations.

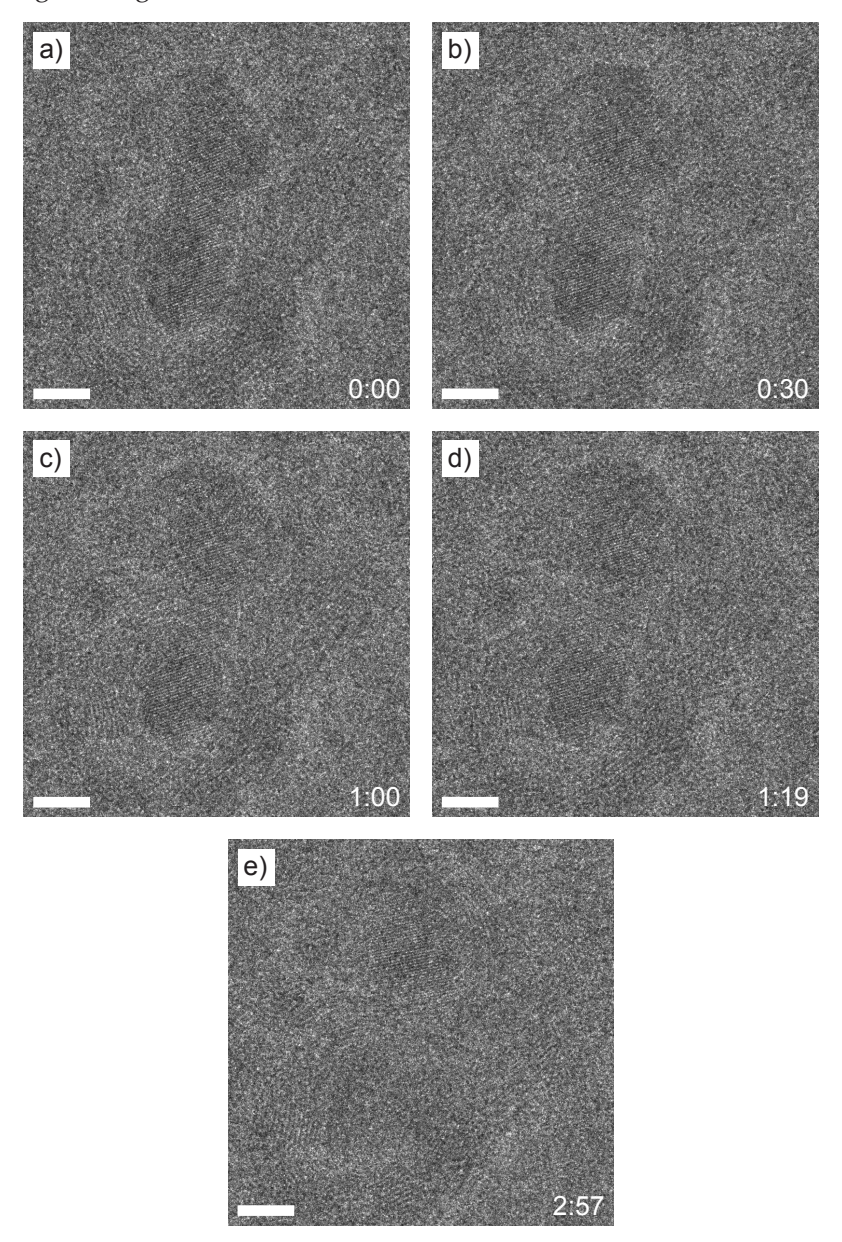
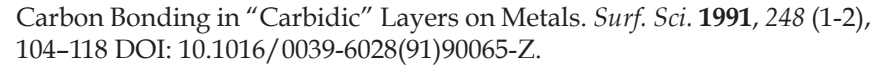


Figure 5.11. Cobalt nanoparticle encapsulated and deformed by an assembly of carbon layers (a). The nanoparticle was slowly squeezed by the surrounding carbon layers (b and c), leading to the splitting of the nanoparticle into two isolated particles (d). After further deformation of the carbon assembly surrounding the particles, the system reached the final, stable state (e). Scale bar is 4 nm.

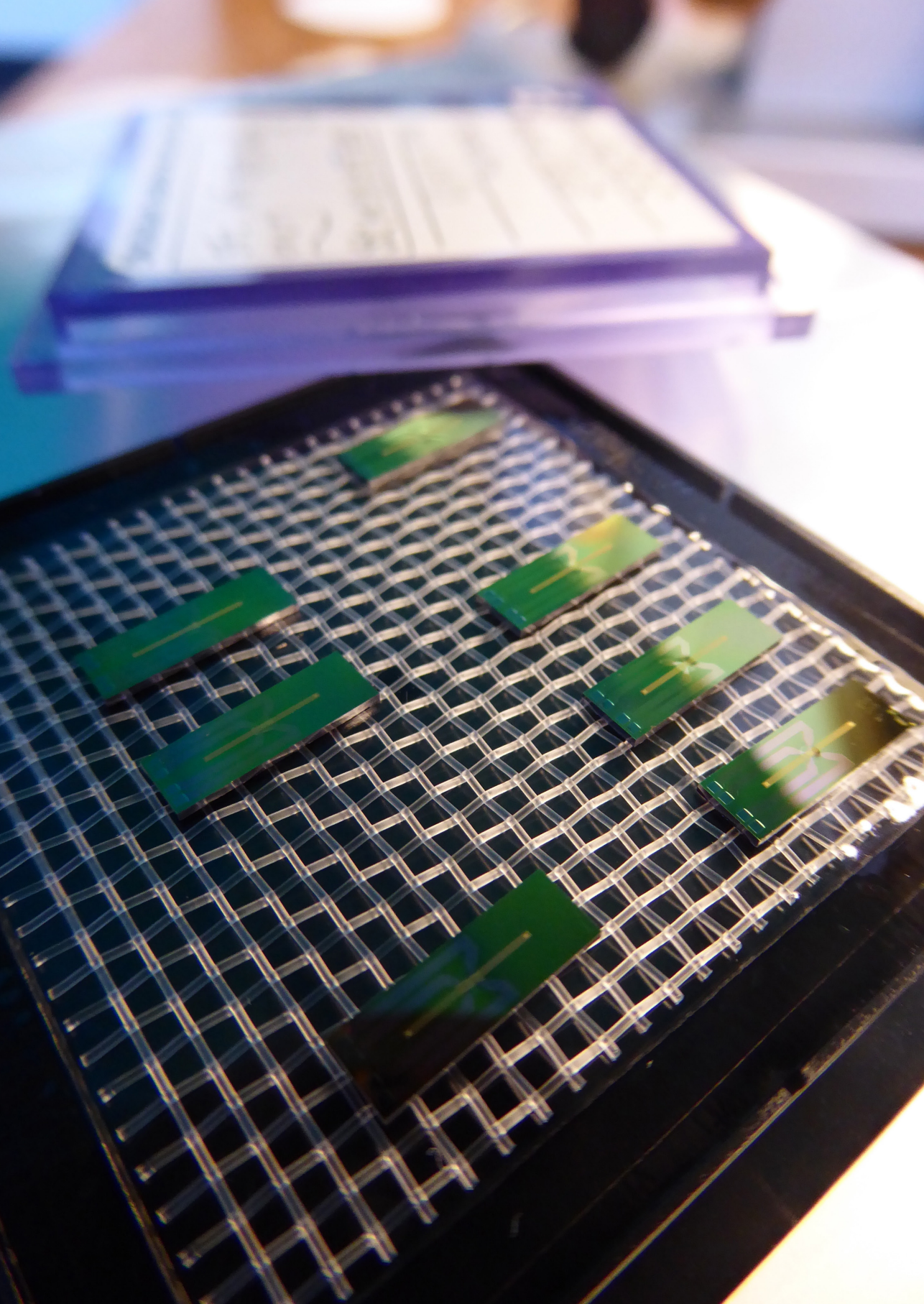
References

- [1] Khodakov, A. Y.; Chu, W.; Fongarland, P. Advances in the Development of Novel Cobalt Fischer-Tropsch Catalysts for Synthesis of Long-Chain Hydrocarbons and Clean Fuels. *Chem. Rev.* **2007**, *107* (5), 1692–1744 DOI: 10.1021/cr050972v.
- [2] Bezemer, G. L.; Bitter, J. H.; Kuipers, H. P. C. E.; Oosterbeek, H.; Holewijn, J. E.; Xu, X.; Kapteijn, F.; van Dillen, A. J.; de Jong, K. P. Cobalt Particle Size Effects in the Fischer-Tropsch Reaction Studied with Carbon Nanofiber Supported Catalysts. *J. Am. Chem. Soc.* **2006**, *128* (12), 3956–3964 DOI: 10.1021/ja058282w.
- [3] Navarro, V.; van Spronsen, M. A.; Frenken, J. W. M. *In Situ* Observation of Self-Assembled Hydrocarbon Fischer-Tropsch Products on a Cobalt Catalyst. *Nature Chem.* **2016**, *8* (10), 929–934 DOI: 10.1038/nchem.2613.
- [4] Banerjee, A.; Navarro, V.; Frenken, J. W. M.; van Bavel, A. P.; Kuipers, H. P. C. E.; Saeys, M. Shape and Size of Cobalt Nanoislands Formed Spontaneously on Cobalt Terraces During Fischer-Tropsch Synthesis. *J. Phys. Chem. Lett.* **2016**, 7 (11), 1996–2001 DOI: 10.1021/acs.jpclett.6b00555.
- [5] Boeller, B.; Ehrensperger, M.; Wintterlin, J. *In Situ* Scanning Tunneling Microscopy of the Dissociation of CO on Co(0001). *ACS Catal.* **2015**, *5* (11), 6802–6806 DOI: 10.1021/acscatal.5b01684.
- [6] Ducreux, O.; Rebours, B.; Lynch, J.; Roy-Auberger, M.; Bazin, D. Microstructure of Supported Cobalt Fischer-Tropsch Catalysts. *Oil Gas Sci. Technol.* **2009**, *64* (1), 49–62 DOI: 10.2516/ogst:2008039.
- [7] Li, S.; Meitzner, G. D.; Iglesia, E. Structure and Site Evolution of Iron Oxide Catalyst Precursors During the Fischer-Tropsch Synthesis. *J. Phys. Chem. B* **2001**, 105 (24), 5743–5750 DOI: 10.1021/jp010288u.
- [8] Tuxen, A. K.; Carenco, S.; Chintapalli, M.; Chuang, C.-H.; Escudero, C.; Pach, E.; Jiang, P.; Borondics, F.; Beberwyck, B.; Alivisatos, A. P.; *et al.* Size-Dependent Dissociation of Carbon Monoxide on Cobalt Nanoparticles. *J. Am. Chem. Soc.* **2013**, 135 (6), 2273–2278 DOI: 10.1021/ja3105889.
- [9] Vendelbo, S. B.; Elkjær, C. F.; Falsig, H.; Puspitasari, I.; Dona, P.; Mele, L.; Morana, B.; Nelissen, B. J.; van Rijn, R.; Creemer, J. F.; et al. Visualization of Oscillatory Behaviour of Pt Nanoparticles Catalysing CO Oxidation. *Nat. Mater.* **2014**, *13* (9), 884–890 DOI: 10.1038/nmat4033.
- [10] Helveg, S.; López-Cartes, C.; Sehested, J.; Hansen, P. L.; Clausen, B. S.; Rostrup-Nielsen, J. R.; Abild-Pedersen, F.; Nørskov, J. K. Atomic-Scale Imaging of Carbon Nanofibre Growth. *Nature* **2004**, 427 (6973), 426–429 DOI: 10.1038/nature02278.
- [11] Wu, J.; Helveg, S.; Ullmann, S.; Peng, Z.; Bell, A. T. Growth of Encapsulating Carbon on Supported Pt Nanoparticles studied by In Situ TEM. *J. Catal.* **2016**, *338*, 295-304, DOI: 10.1016/j.jcat.2016.03.010.
- [12] Peng, Z.; Somodi, F.; Helveg, S.; Kisielowski, C.; Specht, P.; Bell, A. T. High-Resolution In Situ and Ex Situ TEM Studies on Graphene Formation and Growth on Pt Nanoparticles. *J. Catal.* **2012**, *286*, 22-29, DOI: 10.1016/j.jcat.2011.10.008.
- [13] Hofmann, S.; Sharma, R.; Ducati, C.; Du, G.; Mattevi, C.; Cepek, C.; Cantoro,

- M.; Pisana, S.; Parvez, A.; Cervantes-Sodi, F.; Ferrari, A.C.; Dunin-Borkowski, R.; Lizzit, S.; Petaccia, L.; Goldoni, A.; Robertson J. In situ Observations of Catalyst Dynamics during Surface-Bound Carbon Nanotube Nucleation. *Nano Lett.* **2007**, 7 (3), 602–608 DOI: 10.1021/nl0624824
- [14] Zacharaki, E.; Kalyva, M.; Fjellvåg, H.; Sjåstad, A. O. Burst Nucleation by Hot Injection for Size Controlled Synthesis of ε-Cobalt Nanoparticles. *Chem. Cent. J.* **2016**, *10* (1), 10 DOI: 10.1186/s13065-016-0156-1.
- [15] Website Else Kooi Laboratory; http://ekl.tudelft.nl/EKL/home.php, Last consulted: 05-Sept-2016
- [16] Creemer, J. F.; Santagata, F.; Morana, B.; Mele, L.; Alan, T.; Iervolino, E.; Pandraud, G.; Sarro, P. M. An All-in-One Nanoreactor for High-Resolution Microscopy on Nanomaterials at High Pressures. *MEMS* **2011**, 1103–1106 DOI: 10.1109/MEMSYS.2011.5734622.
- [17] Puspitasari, I.; Saputra, P.; Morana, B.; Mele, L.; Santagata, F.; Creemer, J. F.; Kapteijn, F.; Kooyman, P. Particle Imaging and Flow Visualization of *In Situ* TEM Nanoreactors. *Microsc. Microanal.* **2012**, *18* (S2), 740–741 DOI: 10.1017/S1431927612005557.
- [18] Creemer, J. F.; Helveg, S.; Kooyman, P. J.; Molenbroek, A. M.; Zandbergen, H.; Sarro, P. M. A MEMS Reactor for Atomic-Scale Microscopy of Nanomaterials Under Industrially Relevant Conditions. *J. Microelectromech. Syst.* **2010**, *19* (2), 254–264 DOI: 10.1109/JMEMS.2010.2041190.
- [19] Herbschleb, C. T.; van der Tuijn, P. C.; Roobol, S. B.; Navarro, V.; Bakker, J. W.; Liu, Q.; Stoltz, D.; Cañas-Ventura, M. E.; Verdoes, G.; van Spronsen, M. A.; *et al.* The ReactorSTM: Atomically Resolved Scanning Tunneling Microscopy Under High-Pressure, High-Temperature Catalytic Reaction Conditions. *Rev. Sci. Instrum.* **2014**, *85* (8), 083703 DOI: 10.1063/1.4891811.
- [20] Bawn, C. E. H. The Kinetics of the Decomposition of Nickel Carbonyl. *Trans. Faraday Soc.* **1935**, *31*, 440–446.
- [21] Goldberger, W. M.; Othmer, D. F. Kinetics of Nickel Carbonyl Formation. *Ind. Eng. Chem. Proc. Des. Dev.* **1963**, 2 (3), 202–209 DOI: 10.1021/i260007a006.
- [22] Williams, T. C.; Shaddix, C. R. Contamination of Caron Monoxide with Metal Carbonyls: Implications for Combustion Research. *Combust. Sci. Technol.* **2007**, 179 (6), 1225–1230 DOI: 10.1080/00102200601057279.
- [23] Roobol, S. The Structure of a Working Catalyst: From Flat Surfaces to Nanoparticles. PhD thesis, Leiden University, **2014**, ISBN: 9789085932048.
- [24] Dinega, D. P.; Bawendi, M. G. A Solution-Phase Chemical Approach to a New Crystal Structure of Cobalt. *Angew. Chem. Int. Ed. Engl.* **1999**, *38* (12), 1788–1791 DOI: 10.1002/(SICI)1521-3773(19990614)38
- [25] Green, M. Organometallic Based Strategies for Metal Nanocrystal Synthesis. *Chem. Commun. (Camb.)* **2005**, 24, 3002–3011 DOI: 10.1039/b501835h.
- [26] Nakamura, J.; Toyoshima, I.; Tanaka, K. Formation of Carbidic and Graphitic Carbon From CO on Polycrystalline Cobalt. *Surf. Sci.* **1988**, 201 (1-2), 185–194 DOI: 10.1016/0039-6028(88)90605-X.
- [27] Hutson, F. L.; Ramaker, D. E.; Koel, B. E. Spectroscopic Evidence for Carbon-



- [28] Kharissova, O. V.; Kharisov, B. I. Variations of Interlayer Spacing in Carbon Nanotubes. *RSC Adv.* **2014**, *4* (58), 30807–30815 DOI: 10.1039/C4RA04201H.
- [29] Mayoral, A.; Barron, H.; Estrada-Salas, R.; Vazquez-Duran, A.; José-Yacamán, M. Nanoparticle Stability From the Nano to the Meso Interval. *Nanoscale* **2010**, 2 (3), 335–342 DOI: 10.1039/b9nr00287a.
- [30] Hofmeister, H. Fivefold Twinned Nanoparticles. Encyclopedia of Nanoscience, American Scientific Publishers, **2004**, ISBN: 1-58883-001-2.
- [31] Barnard, A. S.; Konishi, H.; Xu, H. F. Morphology Mapping of Platinum Catalysts Over the Entire Nanoscale. *Catal. Sci. Technol.* **2011**, *1* (8), 1440–1448 DOI: 10.1039/C1CY00238D.
- [32] Elechiguerra, J. L.; Reyes-Gasga, J.; Yacaman, M. J. The Role of Twinning in Shape Evolution of Anisotropic Noble Metal Nanostructures. *J. Mater. Chem.* **2006**, 16 (40), 3906–3919 DOI: 10.1039/b607128g.
- [33] Sun, L.; Rodriguez-Manzo, J. A.; Banhart, F. Elastic Deformation of Nanometer-Sized Metal Crystals in Graphitic Shells. *Appl. Phys. Lett.* **2006**, *89* (26), 263104 DOI: 10.1063/1.2403898.
- [34] Banhart, F.; Li, J. X.; Krasheninnikov, A. V. Carbon Nanotubes Under Electron Irradiation: Stability of the Tubes and Their Action as Pipes for Atom Transport. *Phys. Rev. B* **2005**, *71* (24), 241408 DOI: 10.1103/PhysRevB.71.241408.
- [35] Krasheninnikov, A. V.; Lehtinen, P. O.; Foster, A. S.; Nieminen, R. M. Bending the Rules: Contrasting Vacancy Energetics and Migration in Graphite and Carbon Nanotubes. *Chem. Phys. Lett.* **2006**, *418* (1-3), 132–136 DOI: 10.1016/j. cplett.2005.10.106.





Summary

This thesis describes our efforts to understand how catalysts work under reaction conditions, using (quasi) *in situ* transmission electron microscopy (TEM).

Chapters 2 and 3 focus on $(Ni/Co)MoS_2$ supported on γ -Al₂O₃, a catalyst used for the hydrodesulfurization (HDS) of fossil fuel.

Chapter 2 describes how we investigated the effect of exposing (Ni/Co)MoS₂-samples to ambient air using a combination of quasi *in situ* TEM and XPS. By imaging the exact same regions of the sample before and after air exposure, we concluded that the (Ni/Co)MoS₂-slabs were shrinking from the edges towards the center. Quantitative analysis of TEM image series revealed that the average slab length decreased as a function of air exposure time. Larger slabs shrunk, while short slabs disappeared completely. Complementary quasi *in situ* XPS experiments on the same samples showed that Ni-, Co-, Mo-, and S-oxides were formed. Initially, the slabs shrink relatively fast, while prolonged exposure to air only causes moderate further slab length decrease. Since oxides are formed at the edges of the slabs first, we propose that these oxide species form a protective, ring-like barrier around the inner MoS₂-species which shields them from further oxidation.

In chapter 3 the work on these HDS catalysts continues. The effect of a sequential oxidation and resulfidation treatment of $(Ni/Co)MoS_2$ was investigated using quasi *in situ* TEM and XPS, and the activity of the catalysts was determined for gasphase thiophene HDS experiments. After the resulfidation treatment, the average slab length, the slab length distribution and chemical composition of the samples were determined and compared with the freshly sulfided samples. The average slab length increased, while the slab length distribution was more narrow compared to the freshly sulfided sample. XPS showed a slight increase in oxidic species after the oxidation-resulfidation step. Remarkably, the catalytic activity of the samples exhibited a significant increase of up to 39% after resulfidation. We attribute these changes to a size effect of the $(Ni/Co)MoS_2$ slabs: the smaller slabs (< ~1.6 nm) might be less catalytically active.

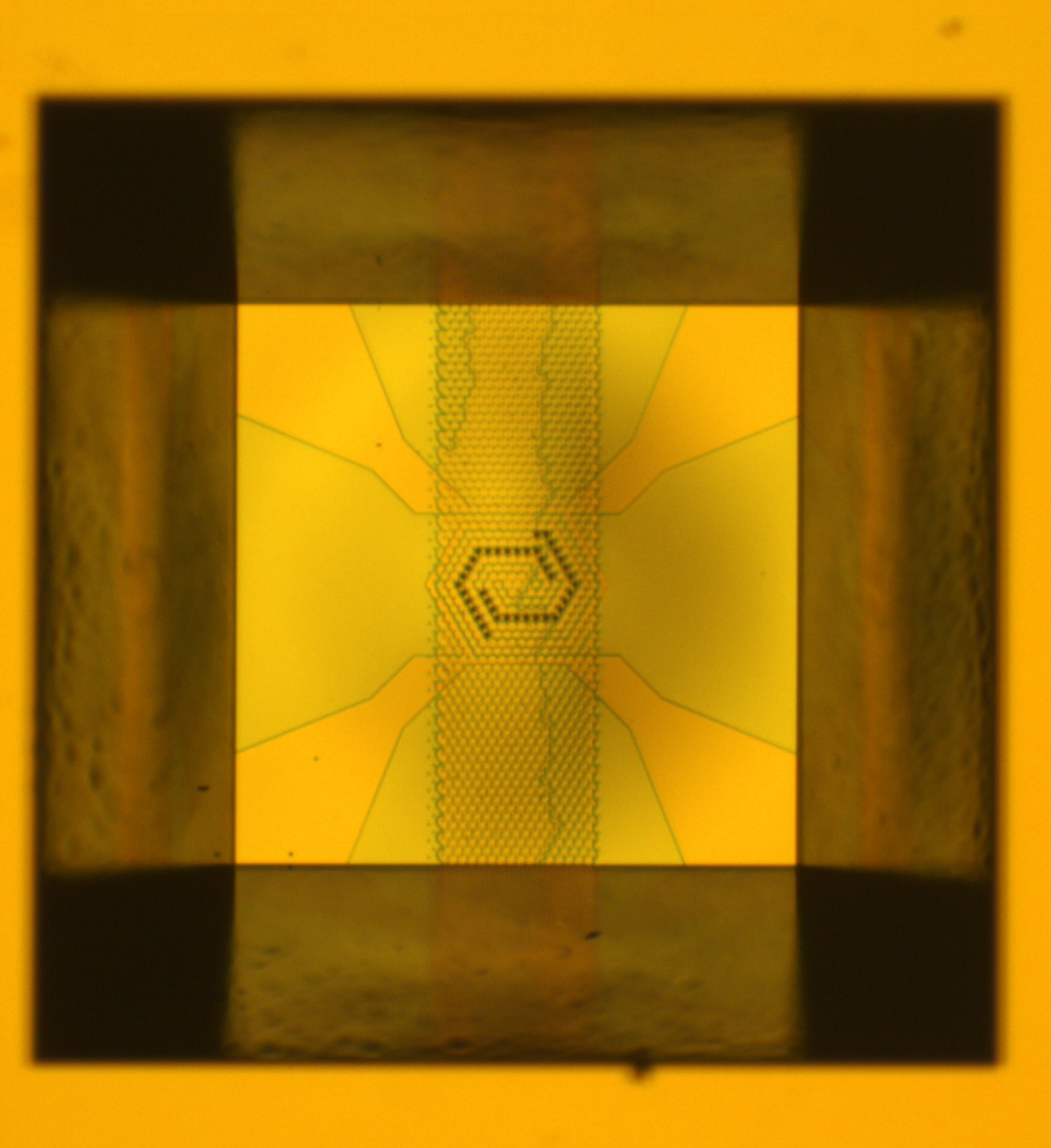
Chapters 4 and 5 discuss the preparation and characterization of Co-Re nanoparticles, and the application of Co nanoparticles in *in situ* TEM experiments.

In chapter 4, β -Mn-type Co_{1-x}Re_x nanoparticles were prepared via colloidal chemistry. For $x \le 0.15$, the Re-content could be controlled readily, as (S)TEM-(EDX) analysis showed homogeneous Re distribution through the uniformly sized nanoparticles. Synchrotron powder X-ray diffraction, in combination with Rietveld refinement, showed that the Re atoms occupy the 12-fold site preferably. Preparation of nanoparticles with Re concentrations of x > 0.15 yielded inhomogeneous particles, showing segregation of Re atoms into separate clusters, indicating that a maximum of 15 atom % Re can be incorporated in the Co lattice. Heating the Co-Re nanoparticles under reducing atmosphere in an *in situ* synchrotron powder X-ray diffraction cell

showed that the nanoparticles were stable up to 300 °C.

Chapter 5 shows how Co nanoparticles were studied using in situ TEM experiments. The nanoparticles were imaged under 1 bar of ${\rm CO:N_2}$ (1:1) at 500 °C, when the deposition of multiple layers of carbon was captured live. Due to the high temperature and presence of CO, the nanoparticle surface facilitated the Boudouard reaction, which is the dissociation of CO and the deposition of solid carbon. Over the course of about 40 minutes, more and more layers of carbon were formed up to a maximum of around 10 layers, after which no more deposition was observed. New layers of carbon were formed in between the surface of the nanoparticle and the already existing carbon layers. During imaging, the formed carbon layers induced mechanical stress in the nanoparticle, proven by the appearance of twin boundaries. Eventually the nanoparticle got permanently deformed by the capping carbon layers.







Samenvatting

In dit proefschrift beschrijf ik ons onderzoek naar katalysatoren en hoe deze werken onder reactie-condities, met behulp van (quasi) *in situ* transmissie-elektronenmicroscopie (TEM).

Hoofdstukken 2 en 3 behandelen (Ni/Co) MoS_2 op een γ -Al $_2O_3$ -drager, een katalysator die veel wordt gebruikt voor de ontzwaveling (HDS) van fossiele brandstoffen.

Hoofdstuk 2 beschrijft het effect van lucht op (Ni/Co)MoS₂ katalysatoren, via een combinatie van metingen met quasi *in situ* TEM en Röntgenfotoelektronenspectroscopie (XPS). Omdat we met de TEM exact dezelfde gebieden van het preparaat afbeeldden, zowel voor als na blootstelling aan lucht, konden we zien dat de (Ni/Co)MoS₂-deeltjes krompen vanaf de randen naar het midden. Kwantitatieve analyse van de TEM-afbeeldingen liet zien dat de gemiddelde diameter van de deeltjes afnam als functie van de tijd dat de ze waren blootgesteld aan lucht. Grotere deeltjes werden kleiner, terwijl kleinere deeltjes zelfs volledig verdwenen. Quasi *in situ* XPS experimenten aan dezelfde preparaten lieten zien dat er Ni-, Co-, Mo-, en S-oxides werden gevormd. In eerste intantie krompen de deeltjes vrij snel, terwijl langere blootstelling aan lucht slechts een gematigde extra afname in diameter veroorzaakte. Omdat de oxides het eerst werden gevormd aan de randen van de deeltjes, stellen we voor dat deze oxides een beschermende, ringachtige barrière vormen die het binnenste deel van elke MoS₂-deeltjes beschermt tegen oxidatie.

In hoofdstuk 3 gingen we verder met deze (Ni/Co)MoS₂ HDS katalysatoren. Hier onderzochten we met quasi *in situ* TEM en XPS het effect van opeenvolgend oxidatie- en herinzwaveling-behandelingen van (Ni/Co)MoS₂-deeltjes, en bepaalden we de katalytische activiteit van de opnieuw ingezwavelde preparaten via gasfase thiofeen HDS experimenten. Na de herinzwaveling-behandeling bepaalden we per preparaat de gemiddelde diameter van de deeltjes, de deeltjesdiameterverdeling en de chemische toestand, en vergeleken dit met de vers ingezwavelde preparaten. De gemiddelde diameter van de deeltjes was groter, terwijl de deeltjesdiameterverdeling minder breed was in vergelijking met de vers ingezwavelde preparaten. XPS liet een bescheiden toename in oxides zien na de oxidatie- en herinzwaveling-behandeling. Opvallend was dat de katalytische activiteit significant toenam na herinzwaveling. De preparaten waren tot wel 39% méér actief. Deze verandering schrijven we toe aan een deeltjesgrootte-effect van de (Ni/Co)MoS₂-deeltjes, waarbij we speculeren dat de kleinere deeltjes (< ~1.6 nm) minder actief zouden kunnen zijn.

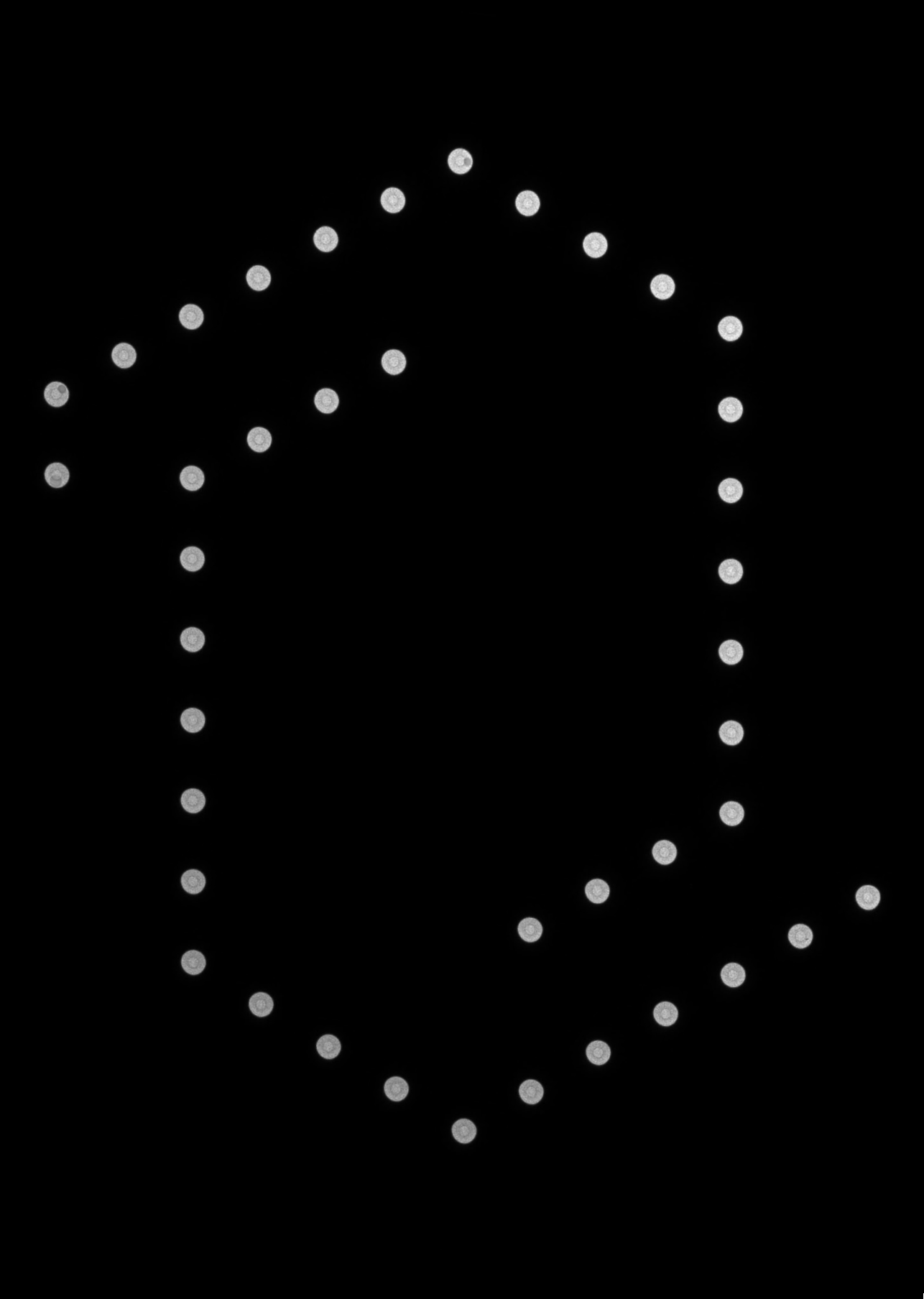
Hoofdstukken 4 en 5 bespreken de preparatie en karakterising van Co-Re nanodeeltjes en de toepassing van Co nanodeeltjes met *in situ* TEM experimenten.

In hoofdstuk 4 laten we zien hoe β -Mn-type $Co_{1-x}Re_x$ nanodeeltjes werden geprepareerd via colloïdechemie. Voor $x \le 0.15$ kon het Re-gehalte gemakkelijk onder

controle gehouden worden, terwijl (S)TEM-(EDX) analyse liet zien dat Re homogeen door de nanodeeltjes verspreid was. Synchrotron poeder-Röntgendiffractie, in combinatie met Rietveldverfijning, liet zien dat de Re atomen zich bevonden in 12-voudige coördinatie. Preparatie van nanodeeltjes met een Re concentratie van x > 0.15 resulteerde in inhomogene deeltjes en segregatie van Re atomen naar losse clusters. Dit laat zien dat er maximaal 15 atoom% Re in de Co kristalstructuur kan worden opgenomen. Het verhitten van Co-Re nanodeeltjes onder reducerende atmosfeer in een *in situ* synchrotron poeder-Röntgendiffractiecel liet zien dat de nanodeeltjes stabiel waren tot 300 °C.

Hoofdstuk 5 laat zien hoe we Co nanodeeltjes analyseerden met $in\ situ\ TEM$ experimenten. Terwijl we de nanodeeltjes afbeeldden onder 1 bar CO:N $_2$ (1:1) bij 500 °C, zagen we live hoe de deeltjes werden bedekt met meerdere laagjes koolstof. Door de hoge temperatuur en de aanwezigheid van CO kon de Boudouard reactie op het oppervlak van de nanodeeltjes plaatsvinden. De Boudouard reactie is het dissociëren van CO en het deponeren van vast koolstof. Gedurende een periode van 40 minuten werden er steeds meer laagjes grafeen gevormd, hetgeen stopte toen er een maximum van ongeveer 10 atoomlagen zichtbaar waren. Nieuwe atoomlagen koolstof werden gevormd tussen het oppervlak van het Co nanodeeltjes en de al eerder gedeponeerde atoomlagen koolstof. Tijdens het afbeelden van dit proces veroorzaakte het koolstofomhulsel mechanische stress in het nanodeeltje, wat ervoor zorgde dat de kristalstructuur van het deeltje tijdelijk werd vervormd. Uiteindelijk werd het deeltje als geheel permanent vervormd.







About the illustrations in this thesis

In order to provide an impression of the laboratory, the instruments and the experimental geometries that have contributed to this PhD thesis, I have provided several photographs and other illustrations.

The cover of this thesis is an artist's impression of the inside of a nanoreactor channel (rendered by Merijn Pen). It features catalyst nanoparticles that cover the channel surface and gas molecules that are flowing over them.

The small illustrations on the top right corner of each page combine into a flip book. Quickly flick all pages from front to back to watch an *in situ* movie of a cobalt nanoparticle that gets covered progressively with layers of carbon atoms. The movie is described and analyzed in detail in Chapter 5.

The first page of each chapter is accompanied by an illustration, in most cases directly related to that chapter. Chapter 1 shows a Philips CM30T microscope, the oldest operational transmission electron microscope in the HREM group at the Delft University of Technology. Installed in 1989, it is now often used for student TEM training. After sufficient training, access is provided to more sophisticated TEMs. The newest electron microscope is the FEI Titan³, shown at the start of Chapter 4.

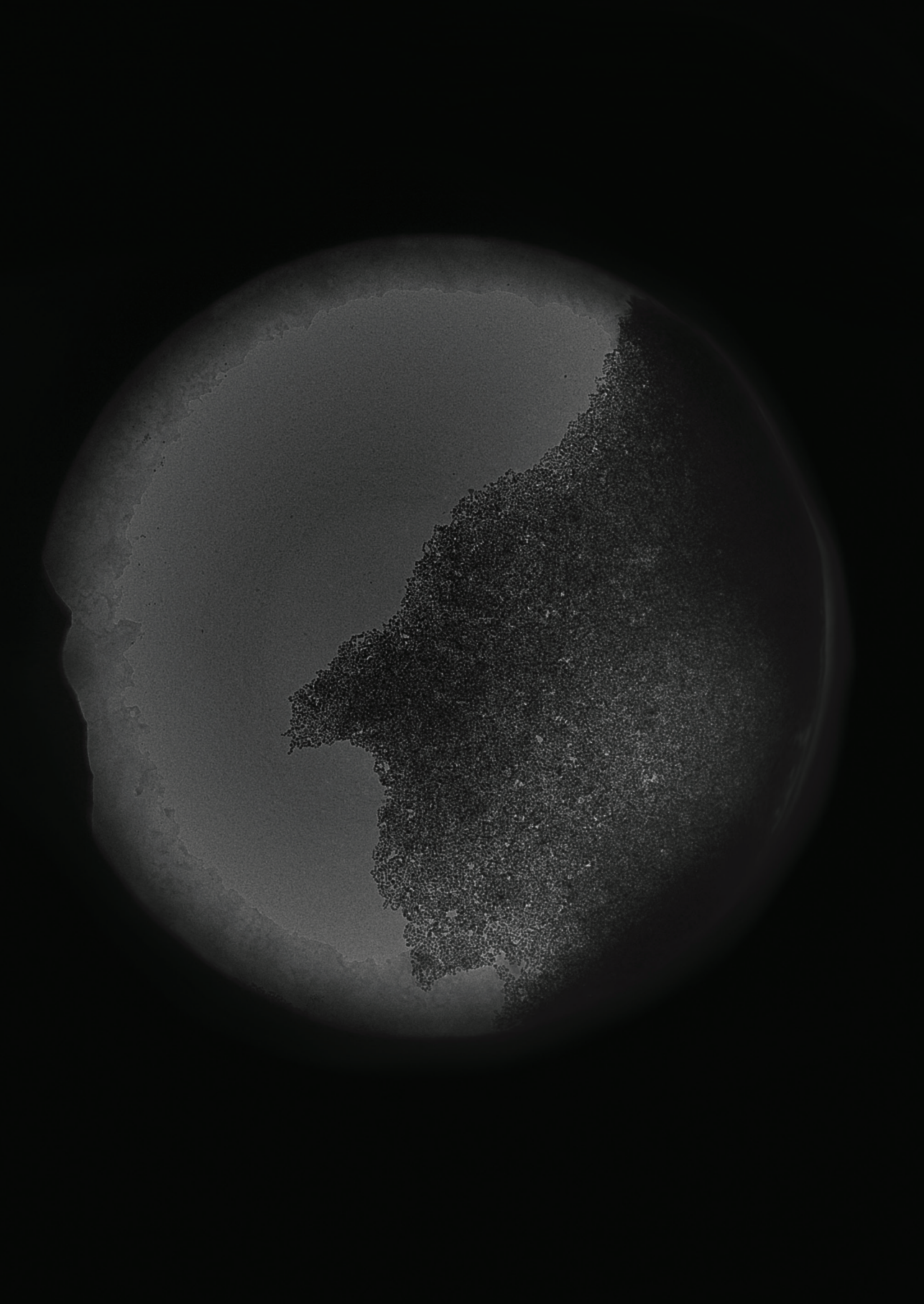
The grayscale image next to the Table of Contents displays a TEM image of a sample grid. The small dark lumps are pieces of γ -Al₂O₃ support material, carrying MoS₂-slabs. The start of Chapter 2 shows a high-magnification TEM image of such a particle supporting MoS₂-slabs. A STEM-HAADF image of CoRe nanoparticles on an ultrathin carbon sample grid is shown next to the Curriculum Vitae of the author.

The *in situ* TEM sample holder is shown at the start of Chapter 5, the tip of the holder opened, revealing a loaded nanoreactor.

During sample loading, we monitor the liquid flowing through the nanoreactor by use of an optical microscope. This is shown by the photograph accompanying the Dutch Samenvatting. Notice that the central channel is partially filled with liquid, which is visible at the top left and in the entire right side of the channel. A set of nanoreactors in a gel box is shown at the Summary chapter.

A low-magnification TEM image of a nanoreactor, showing the 41 electron-transparent windows, each window 7 μ m in diameter, is placed to the left of this text. After loading nanoparticles into the nanoreactor, the windows get covered with nanoparticles, as is shown at the Acknowledgements section.

Photographs of the gas flow system are provided at the start of Chapter 3 and next to the List of Publications.



Acknowledgements

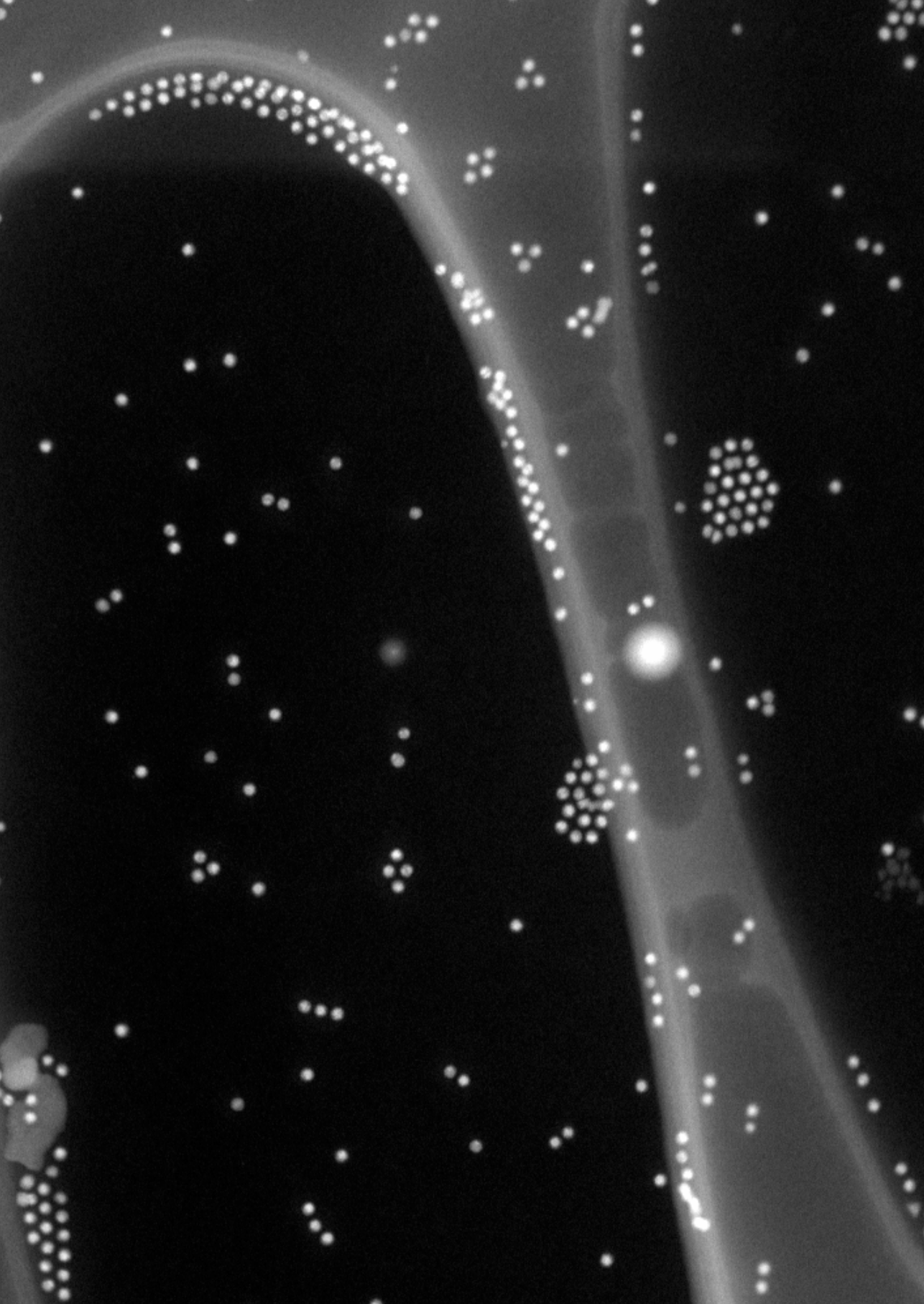
The work described in this thesis is the result of many people working together rather than that of solely my own efforts. I would like to express my gratitude to the people that contributed to this work or supported me in any other way during my time as a PhD student.

Firstly, I would like to thank my promotor Joost Frenken and co-promotor Patricia Kooyman for giving me the opportunity to start this endeavor, sharing their scientific guidance, passion and inspiration, and for the many hours Patricia spent with me at the TEM. I am grateful to Ellie van Rijsewijk for all her administrative help and support. My work at TU Delft was made possible by Henny Zandbergen, who provided access to the TEM facilities, and by the support of Marijke van der Veen. Frans Tichelaar taught me all the details about TEM experiments and was essential in my work at the TEMs. Laboratory work was made possible by Johan Bakker (Leiden University), Tom de Kruijff and Jouk Jansen (TU Delft), and by support from the Fine Mechanical Department of Leiden University by Mirthe Bergman. Irene Groot was of great help by directing our group in Leiden during the last three years.

I gratefully acknowledge the collaborative spirit that I have enjoyed of my current and former colleagues from the Leiden University Interface Physics group: Pavel Antonov, Dirk van Baarle, Yohan Fuchs, Rik Mom, Violeta Navarro, Willem Onderwaater, Mahesh Prabhu, Sander Roobol, Amir Saedi, Christina Sfiligoj, Matthijs van Spronsen, Andriy Taranovskyy, Sabine Wenzel, and Görsel Yetik; Gertjan van Baarle and Peter van der Tuijn (Leiden Probe Microscopy); the technical support by Bert Crama, Kees van Oosten, Christiaan Pen, Marcel Rost, Fred Schenkel, and Gijsbert Verdoes (Leiden University); my colleagues from the TU Delft HREM group: Majid Ahmadi, Ahmet Erdamar, Yoones Kabiri, Tatiana Kozlova, Sairam Malladi, Mariya Neklyudova, Leonardo Vicarelli, Meng-Yue Wu, Anil Yalçin; and the help by Shibabrata Basak, Merijn Pen, and Qiang Xu (DENSsolutions).

The *in situ* TEM experiments were made possible by the supply of nanoreactors via Fredrik Creemer, Bruno Morana, and Gregory Pandraud (Else Kooi Lab); and the support of Pleun Dona, Bas Hendriksen, and Luigi Mele (FEI).

The various catalysts used during my experiments were kindly provided via the pleasant collaborations we had, with Anja Sjåstad and Eirini Zacharaki (University of Oslo), and with the experimental support via Lennart van Haandel, Emiel Hensen, and Miao Yu (TU Eindhoven).



Curriculum Vitae

Marien Bremmer was born on April 9, 1990 in Katwijk, the Netherlands. He got his highschool degree from the Visser 't Hooft Lyceum in Leiden in 2008. Bremmer continued his studies through a BSc in Molecular Science and Technology (MST) at Leiden University and Delft University of Technology, obtaining his degree in 2011 after a research project on the synthesis of coiled-coil peptides and their applications in lipid membrane vesicle fusion, in the research group of Prof. Dr. Alexander Kros. During his MSc project in Chemistry at Leiden University, he continued his research on lipid membrane layers in the group of Kros. Using liquid-cell ellipsometry and liquid-cell AFM he studied the properties of multilayer self-assembled lipid layers, supported on silicon wafers. Before graduating, he finished a second research project at Leiden Probe Microscopy BV, where he built and used a tabletop gas flow reactor for catalysis experiments. Using the reflection of visible light, he studied the effect of CO oxidation conditions on the surface of a Pd single crystal.

Under the supervision of Prof. Dr. Joost Frenken and Prof. Dr. Patricia Kooyman he went on to pursue a PhD at the Huygens-Kamerlingh Onnes Laboratory of Leiden University, in collaboration with the Zandbergen Lab at Delft University of Technology. He studied (Ni/Co)MoS₂ catalyst particles in collaboration with Prof. Dr. Emiel Hensen from Eindhoven University of Technology, using quasi *in situ* transmission electron microscopy. In collaboration with Prof. Dr. Anja Sjåstad from University of Oslo he performed *in situ* TEM experiments on cobalt nanoparticles using gas flow systems, a dedicated *in situ* TEM sample holder, and nanoreactors to contain catalyst samples.





List of Publications

Bremmer, G.M.; van Haandel, L.; Hensen, E.J.M.; Frenken, J.W.M.; Kooyman, P.J. Instability of $NiMoS_2$ and $CoMoS_2$ hydrodesulfurization catalysts at ambient conditions: a quasi *in situ* high-resolution transmission electron microscopy and x-ray photoelectron spectroscopy study.

Journal of Physical Chemistry C, **2016**, 120 (34), 19204–19211; DOI: 10.1021/acs. jpcc.6b06030. (Chapter 2 of this thesis)

<u>Bremmer, G.M.</u>; van Haandel, L.; Hensen, E.J.M.; Frenken, J.W.M.; Kooyman, P.J. The effect of oxidation and resulfidation on (Ni/Co)MoS₂ hydrodesulfurization catalysts.

In preparation (Chapter 3 of this thesis)

Zacharaki, E.; <u>Bremmer, G.M.</u>; Kalyva, M.; Kooyman, P.J.; Fjellvåg, H.; Sjåstad, A.O. Cobalt-rhenium β -Mn type bimetallic nanoparticles prepared via colloidal chemistry. *Submitted* (Chapter 4 of this thesis)

Bremmer, G.M.; Zacharaki, E.; Sjåstad, A.O.; Navarro, V.; Frenken, J.W.M.; Kooyman, P.J.

In situ TEM observation of the Boudouard reaction: Multi-layered graphene formation from Co on cobalt nanoparticles at atmospheric pressure.

Faraday Discussions, 2017, 197, 337–351; DOI: 10.1039/C6FD00185H. (Chapter 5 of this thesis)

Bremmer, G.M.; Zacharaki, E.; Sjåstad, A.O.; Navarro, V.; Frenken, J.W.M.; Kooyman, P.J.

In situ TEM observation of multilayer graphene formation from Co on cobalt nanoparticles at atmospheric pressure.

Microscopy and Microanalysis, 2017, 23, 896-897; DOI: 10.1017/S1431927617005141

Bremmer, G.M.; van Haandel, L.; Hensen, E.J.M.; Frenken, J.W.M.; Kooyman, P.J. A quasi *in situ* HRTEM study of the air stability of (Ni/Co)MoS₂ hydrodesulfurization catalysts.

Microscopy and Microanalysis, **2015**, 21 (S3), 801-802; DOI: 10.1017/S1431927615004808

van Haandel, L.; Longo, A.; <u>Bremmer, G.M.</u>; Kooyman, P.J.; Bras, W.; Hensen, E.J.M.; Weber, Th.

Formation of supported molybdenum disulfide nanoparticles under industrial conditions.

In preparation

van Haandel, L.; Bremmer, G.M.; Hensen, E.J.M.; Weber Th.

The effect of organic additives and phosphoric acid on sulfidation and activity of (Co)Mo/Al₂O₂ hydrodesulfurization catalysts.

Journal of Catalysis, 2017, 351, 95-106; DOI: 10.1016/j.jcat.2017.04.012

van Haandel, L.; Bremmer, G.M.; Hensen, E.J.M.; Weber Th.

Influence of sulfiding agent and pressure on structure and performance of CoMo/Al₂O₂ hydrodesulfurization catalysts.

Journal of Catalysis, 2016, 342 (C), 27-39; DOI: 10.1016/j.jcat.2016.07.009

van Haandel, L.; <u>Bremmer, G.M.</u>; Kooyman, P.J.; van Veen, J.A.R.; Weber, Th.; Hensen, E.J.M.

Structure-activity correlations in hydrodesulfurization reactions over Ni-promoted $Mo_vW_{(1,v)}S_2/Al_2O_3$ catalysts.

ACS Catalysis, 2015, 5 (12), 7276–7287; DOI: 10.1021/acscatal.5b01806

Onderwaater, W.; Taranovskyy, A.; <u>Bremmer, G.M.</u>; van Baarle, G.; Frenken, J.W.M.; Groot, I.M.N.

From dull to shiny: A novel setup for reflectance difference analysis under catalytic conditions.

Review of Scientific Instruments, 2017, 88, 023704; DOI: 10.1063/1.4975930

Versluis, F.; Voskuhl, J.; van Kolck, B.; Zope, H.; <u>Bremmer, G.M.</u>; Albregtse, T.; Kros, A.

In situ modification of plain liposomes with lipidated coiled coil forming peptides induces membrane fusion.

Journal of the American Chemical Society, **2013**, 135 (21), 8057-8062; DOI: 10.1021/ja4031227

